THE PHENIX MUON SPECTROMETER AND J/PSI PRODUCTION IN 200 GeV CENTER OF MASS ENERGY PROTON-PROTON COLLISIONS AT RHIC

BY

ANDREW S. HOOVER, B.S., M.S.

A dissertation submitted to the Graduate School

in partial fulfillment of the requirements

for the degree

Doctor of Philosophy

Major Subject: Physics

New Mexico State University

Las Cruces, New Mexico

May 2003

"The PHENIX Muon Spectrometer and J/Psi Production in 200 GeV Center of Mass Energy Proton-Proton Collisions at RHIC," a dissertation prepared by Andrew S. Hoover in partial fulfillment of the requirements for the degree, Doctor of Philosophy, has been approved and accepted by the following:

Linda Lacey
Dean of the Graduate School

Stephen Pate
Chair of the Examining Committee

Date

Committee in charge:

Dr. Stephen Pate, Chair

Dr. Matthias Burkardt

Dr. James Herndon

Dr. Gary Kyle

Dr. Heinrich Nakotte

VITA

July 14, 1975	Born in Sellersville, Pennsylvania, USA
1993-1997	B.S., Colorado State University, Ft. Collins, Colorado
1997-2000	M.S., New Mexico State University, Las Cruces, New Mexico

PROFESSIONAL AND HONORARY SOCIETIES

American Physical Society

PUBLICATIONS

"PHENIX Muon Arms," H. Akikawa *et al.*, accepted for publication in Nucl. Instrum. Meth. **A**, Special Issue.

"Measurement of the Λ and $\bar{\Lambda}$ Particles in Au+Au Collisions at $\sqrt{s_{NN}}$ = 130 GeV," K. Adcox *et al.*, Phys. Rev. Lett. **89**, 092302 (2002)

"Flow Measurements via Two-particle Azimuthal Correlations in Au + Au Collisions at $\sqrt{s_{NN}}$ = 130 GeV," K. Adcox *et al.*, Phys. Rev. Lett. **89**, 212301 (2002)

"Event-by Event Fluctuations in Mean p_T and Mean e_T in $\sqrt{s_{NN}}$ = 130 GeV Au+Au Collisions," K. Adcox *et al.*, Phys. Rev. **C66**, 024901 (2002)

"Net Charge Fluctuations in Au+Au Interactions at $\sqrt{s_{NN}}$ = 130 GeV," K. Adcox *et al.*, Phys. Rev. Lett. **89**, 082301 (2002)

"Measurement of Single Electrons and Implications for Charm Production in Au+Au Collisions at $\sqrt{s_{NN}}$ = 130 GeV," K. Adcox *et al.*, Phys. Rev. Lett. **88**, 192303 (2002)

"Transverse-Mass dependence of Two-Pion Correlations for Au+Au collisions at $\sqrt{s_{NN}}$ = 130 GeV," K. Adcox *et al.*, Phys. Rev. Lett. **88**, 192302 (2002)

"Centrality dependence of $\pi^{+/-}$, $K^{+/-}$, p and $\bar{p}$ production from $\sqrt{s_{NN}}$ = 130

GeV Au + Au collisions at RHIC," K. Adcox *et al.*, Phys. Rev. Lett. **88**, 242301 (2002)

"Suppression of Hadrons with Large Transverse Momentum in Central Au+Au Collisions at $\sqrt{s_{NN}}$ = 130 GeV," K. Adcox *et al.*, Phys. Rev. Lett. **88**, 022301 (2002)

"Measurement of the Midrapidity Transverse Energy Distribution from $\sqrt{s_{NN}}$ = 130 GeV Au-Au Collisions at RHIC," K. Adcox *et al.*, Phys. Rev. Lett. **87** 052301 (2001)

"Centrality Dependence of Charged Particle Multiplicity in Au-Au Collisions at $\sqrt{s_{NN}}$ = 130 GeV," K. Adcox *et al.*, Phys. Rev. Lett. **86** 3500 (2001)

FIELD OF STUDY

Major Field: Physics

ABSTRACT

THE PHENIX MUON SPECTROMETER AND J/PSI PRODUCTION IN 200 GeV CENTER OF MASS ENERGY PROTON-PROTON COLLISIONS AT RHIC

BY

ANDREW S. HOOVER, B.S., M.S.

Doctor of Philosophy

New Mexico State University

Las Cruces, New Mexico, 2003

Dr. Stephen F. Pate, Chair

The PHENIX experiment is one of the large detector projects at the Relativistic Heavy-Ion Collider (RHIC) at Brookhaven National Laboratory. One of the unique features of the PHENIX detector is the muon tracking and identification system. No other RHIC experiment has a muon detection capability. Among the many physics topics explored by the observation of muons in Au-Au collisions are the effects of Debye screening on vector meson production, and the search for an enhancement in strangeness and heavy flavor production. In the collisions of

polarized protons, the muon arms can explore the polarization of quarks and gluons in the proton through W boson production, the Drell-Yan process, and open heavy flavor production. The muon detector system covers the rapidity range -2.2 $<$ y $<$ -1.2 for the south arm and 1.2 $<$ y $<$ 2.4 for the north arm, with full azimuthal coverage. The detector provides muon tracking and identification in the momentum range $2 < p < 50$ GeV, and π/μ rejection of 10^{-4}.

The south muon arm was completed in 2001 for the second RHIC running period. The performance of the muon spectrometer during its first data taking period will be discussed. The production cross section for J/ψ in proton-proton collisons at $\sqrt{s} = 200$ GeV is measured. The measured value is in good agreement with the color evaporation model and QCD predictions. Although the number of J/ψ currently available for study will not allow a definitive measurement of the J/ψ polarization, a technique for performing the measurement is studied and a very low statistics analysis produces a result which is consistent with expectations.

CONTENTS

LIST OF TABLES

LIST OF FIGURES

1 INTRODUCTION

In 1984, the first proposal was submitted for the design and development of a world class colliding beam accelerator at Brookhaven National Laboratory. The facility came to be known as the Relativistic Heavy Ion Collider (RHIC). Funding was secured in 1991, and the accelerator achieved its first collisions in 2000.

The main purpose of RHIC is to search for the existence of Quark Gluon Plasma (QGP), a state of matter predicted by Quantum Chromodynamics (QCD) to be created in ultrarelativistic collisons of heavy nuclei as the result of a phase transition. There are many examples of phase transitions experienced by matter, the most familiar one being the progression of water from its frozen solid state to a liquid state, and finally to the gaseous state in response to a change in temperature or pressure. There is also a phase transition of an ordinary gas to a plasma at sufficiently high pressures or temperatures. In nuclear matter, if the energy density is high enough ($\sim$ 1-3 GeV/fm^3), there is expected to be a phase transition to the QGP. Inside of the QGP, the baryon density and temperature are high enough that long range interactions are dynamically screened. This results in asymptotic freedom (weak coupling of quarks and gluons) and deconfinement of quarks and gluons from bound states. The properties of reactions occurring inside the QGP are manifest in the observable final state products resulting from the hadronization stage as the QGP cools. These final state products are observed

and used to reconstruct the initial properties of the QGP.

The collider can accelerate ion species ranging from protons to gold. The ability of RHIC to accelerate any ion species permits many other types of physics processes to be studied in addition to the search for QGP. The proton beam can be polarized, allowing for a substantial spin physics program. Of particular interest are the relative contributions of individual partons to the overall nucleon spin. The beam can be polarized either longitudinally (nucleon spin aligned along the beam axis) or transversely (nucleon spin aligned perpendicularly to the beam axis). RHIC can produce collisions at a center of mass energy of $\sqrt{s_{NN}} = 200$ GeV for Au beams, and $\sqrt{s} = 500$ GeV for proton beams.

One of the experiments that has been built at RHIC is the Pioneering High Energy Nuclear Interaction eXperiment (PHENIX) detector. The original design of PHENIX was geared toward the observation of the QGP from many different physics channels. The addition of a second muon spectrometer arm to the PHENIX experiment significantly enhanced the capabilities of the detector, and it allows for a robust spin physics program. The benefit of the second muon arm is mostly in the increased acceptance of the detector, allowing for large numbers of events to be collected. The muon spectrometer consists of two detector arms which detect muons at forward rapidities with complete azimuthal coverage. The design for each arm includes tracking in a radial magnetic field followed by a muon identifier. The south muon arm was completed in 2001 and collected its first data

during RHIC run 2 in 2001-2002. The north muon arm was completed for RHIC run 3.

There are many physics processes producing muons in the final state. Some of these processes are expected to provide signals of QGP creation, and others probe the spin structure of the nucleon. Table 1.1 shows the major physics processes that produce muons which can be studied with the PHENIX muon spectrometer.

The scope of the PHENIX muon physics program is impressive. A detailed discussion of many of the physics measurements possible with the muon arms will now be presented.

1.1 Charmonium Production

Charmonium is a bound state of a charm and anticharm quark ($c\bar{c}$). Charmonium includes η_c, J/ψ , ψ', and χ_c states. The production of charmonium is interesting for several reasons. The most basic reason is that the production mechanism of charmonium is not well understood in QCD theory. In addition, there have been interesting results from the CERN NA50 experiment suggesting that charmonium production may be suppressed in Pb-Pb collisions at $\sqrt{s_{NN}} =$ 17.3 GeV, just above the threshold for creation of the QGP. The theoretical models for J/ψ production in a QGP are at best confusing, as there exist predictions for J/ψ suppression as well as enhancement in a QGP environment.

The original charmonium production models used for calculations did not cor-

Table 1.1: Physics processes that can be studied with the PHENIX muon spectrometer and their significance.

Physics Process	Significance
Debye screening of QCD interactions	
- melting order of Υ, J/ψ , ψ'	Signature of QGP
- suppression/enhancement of J/ψ	Signature of QGP
Strangeness and Open Heavy Flavor Production	
- ϕ production	Strangeness enhancement in QGP
- Open charm and bottom production	Gluon polarization
J/ψ , ψ', and Υ Production	
- Production cross section of charmonium	Test QCD predictions
- Polarization of charmonium	Test of color octet production mechanism
Other Spin Processes	
- $W^{\pm}$ production	Quark/Antiquark helicity distribution
- Polarized Drell-Yan	Antiquark helicity distribution

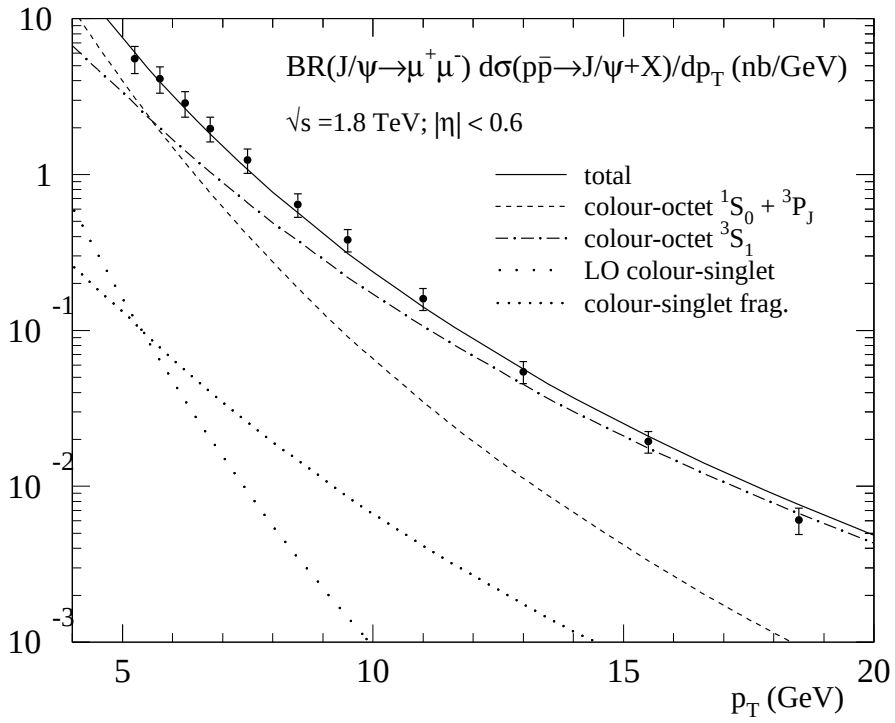

Figure 1.1: Color singlet and color octet contributions to direct J/ψ production and the Tevatron CDF data (taken from [Krä 01]).

rectly predict the production cross section of high p_t J/ψ and ψ' particles at the Tevatron. In fact, the observed cross sections were orders of magnitude larger than the prediction of the color singlet model [Bai 83][Gas 87]. The CDF collaboration obtained differential cross section data for direct J/ψ production as a function of p_t, which is compared to several charmonium production models in Figure 1.1. In the leading order color singlet model, only heavy quark pairs produced in the colorless singlet state may form the physical charmonium. This model is somewhat intuitive considering that the observable charmonium must be in the colorless singlet state. Figure 1.2a shows charmonium production via the

leading order color singlet process. The standard spectroscopic notation is used to describe the charmonium states: $^{2S+1}L_J^{(n)}$, where L is the orbital angular momentum, S is the spin, and J is the total angular momentum. The number n indicates whether the state is a color singlet ($n = 1$) or a color octet ($n = 8$). In Figure 1.2, the scaling dependence of the different production mechanisms on α_s, p_t , and the heavy quark velocity v ($v^2 \sim 0.3$ for charmonium) is shown. The model obviously fails to predict the charmonium cross section, as seen in Figure 1.1. The leading order color singlet model prediction exhibits a very large disagreement with the experimental data. The leading order color singlet prediction also scales like $\frac{1}{p_t^8}$ rather than the $\frac{1}{p_t^4}$ scaling observed in the experimental data [Krä 01]. J/ψ production via color-singlet fragmentation is shown in Figure 1.2b. In the fragmentation mechanism, a high p_t parton decays into charmonium and emits other partons. This mechanism, although of higher order in α_s, is enhanced by a factor $\frac{p_t^4}{(2m_c)^4}$, and therefore dominates the leading order singlet process at large p_t. With color singlet fragmentation included, the theory generates the correct shape for the p_t dependance, but it has incorrect normalization. With the introduction of fragmentation, the realization soon followed that a color octet charmonium state could form and become an observable color singlet state via emission of soft gluons [Bra 95]. Production of color octet state charmonium is shown in Figure 1.2c. The shaded circle represents the color octet state which continues on to the color singlet state after emission of a gluon. The color of the octet state is radiated away

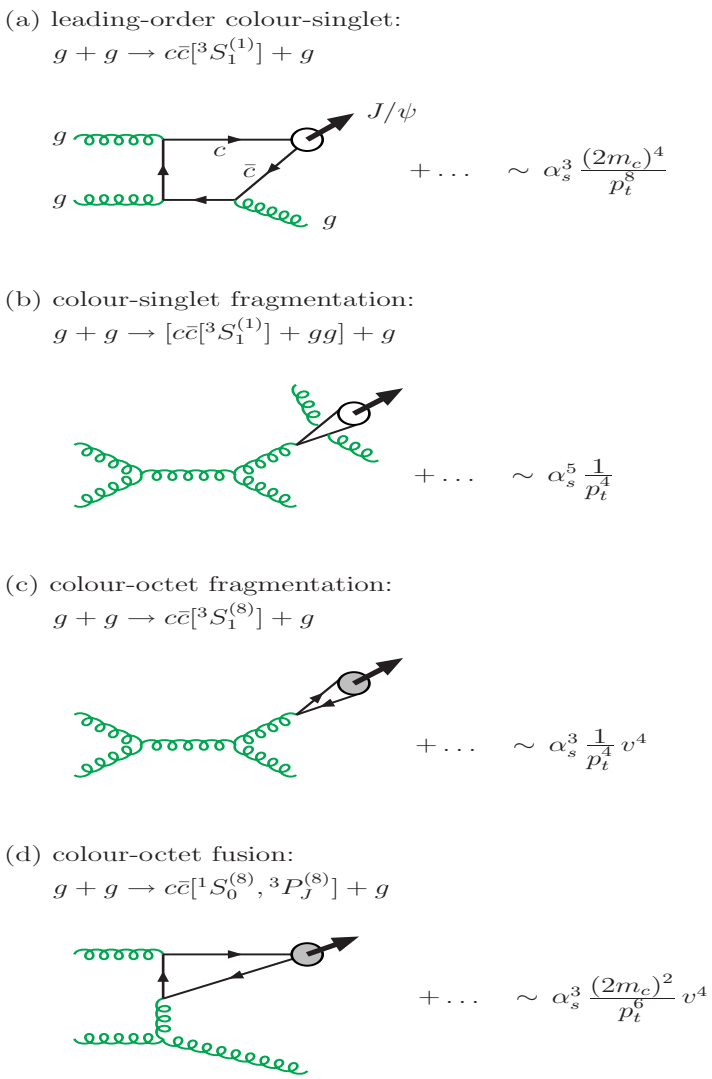

Figure 1.2: Production channels for charmonium (taken from [Krä 01]).

by the emission of the gluon, producing the observable color singlet state. This transformation of the color octet J/ψ state to the color singlet state is depicted in Figure 1.3. As an example, a red-antiblue color octet charmonium state radiates

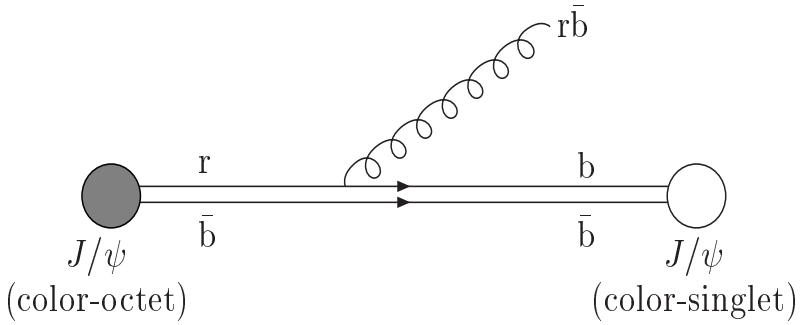

Figure 1.3: Transition of a color octet charmonium state to a color singlet state via emission of a gluon.

a red-antiblue gluon to produce a colorless blue-antiblue color singlet final state. The color octet fragmentation process is suppressed by v^4 compared to the leading order color singlet term. However, there is an enhancement of two powers in α_s which overpowers the suppression, allowing the color octet fragmentation process to become the dominant source of charmonium production at large p_t.

In addition to the color octet fragmentation process, a color octet fusion mechanism also contributes. The fusion process is shown in Figure 1.2d. This process is expected to be significant at $p_t \sim 2m_c$.

For bound states of heavy quarks (like charmonium), where quark velocities are small, the effective theory of non-relativistic QCD (NRQCD) is applicable [Bod 97]. The production cross section for $A + B \to \psi + X$ is [Ben 96]

$$\sigma_\psi = \sum_{i,j} \int_0^1 \mathrm{d}x_1 \mathrm{d}x_2 f_{i/A}(x_1) f_{j/B}(x_2) \hat{\sigma}(ij \to \psi) \ , \tag{1.1}$$

where

$$\hat{\sigma}(ij \to \psi) = \sum_n C^{ij}_{Q\bar{Q}[n]} \langle O^{\psi}_n \rangle \ . \tag{1.2}$$

In Equation 1.1, x_1 and x_2 are the fraction of the parent nucleon momenta carried by each of the two colliding partons, and $f_{i/A}$ and $f_{j/B}$ are the parton densities. In Equation 1.2, $C^{ij}_{Q\bar{Q}[n]}$ are short distance coefficients describing the production of a quark anti-quark pair in a particular color and angular momentum state n. These coefficients can be calculated with perturbative QCD and have expansions in α_s. The $\langle O^{\psi}_n \rangle$ are non-perturbative matrix elements describing the long-distance hadronization process of the $c\bar{c}$ pair. They are related to the probability for the $c\bar{c}$ pair to transition into a particular final state. The matrix elements have expansions in powers of the heavy quark velocity v. They cannot be calculated with QCD and must be extracted from experimental data.

The separation of the production amplitude into short distance perturbative coefficients and long distance non-perturbative matrix elements is known as the NRQCD factorization method. This factorization is possible because production of a charmonium state involves two different scales. The short distance perturbative process describing the generation of the onium pair involves momenta of order $m_c \sim 1.5$ GeV. The long distance process of the charmonium pair transitioning to bound charmonium involves smaller scale momenta of order $m_c v \sim 0.9$ GeV and $m_c v^2 \sim 0.5$ GeV.

The scaling of the matrix elements with v is determined by NRQCD velocity-

scaling rules. Electric and magnetic transitions can change a color singlet state to a color octet state, and a color octet state to a color singlet or another color octet state. Electric transitions obey the selection rules $\triangle L = \pm 1$ and $\triangle S = 0$, whereas magnetic transitions obey $\triangle L = 0$ and $\triangle S = \pm 1$. The dominant Fock state for charmonium is a $c\bar{c}$ color singlet state. Higher Fock states can be reached by making some number of electric and magnetic transitions from the dominant state. For each electric transition, the matrix element scales like v^2; for each magnetic transition, the matrix element scales like v^4. A matrix element generally scales like $v^{3+2L+2E+4M}$, where L is the orbital angular momentum of the $c\bar{c}$ state, and E (M) is the number of electric (magnetic) transitions needed to reach the state from the dominant Fock state [Krä 01]. It is common for the velocity scaling of the matrix elements to be listed with respect to the base state ${}^3S_1^{(1)}$. The velocity scaling rules for the most important matrix elements in charmonium production with respect to this base state are: ${}^3S_1^{(1)} \sim 1$, ${}^3S_1^{(8)} \sim v^4$, ${}^1S_0^{(8)} \sim v^4$, and ${}^3P_J^{(8)} \sim v^4$, as shown in Figure 1.2.

If the ${}^3S_1^{(1)}$, ${}^3S_1^{(8)}$, ${}^1S_0^{(8)}$, and ${}^3P_J^{(8)}$ diagrams are included in the NRQCD cross section for charmonium production, the unknown matrix elements can be chosen such that the theory agrees quite well with the CDF data [Nas 01], as shown in Figure 1.1. The matrix elements are found to be on the order of 10^{-2} GeV^3. Thus, the discrepancy between the original charmonium production models and the observed experimental results has been resolved. However, the solution comes from

the somewhat ambiguous approach of fitting the free parameters in the models to match the experimental data. More measurements of charmonium production are clearly needed to enhance our understanding and encourage development of improved theoretical models. The QCD matrix elements should be universal, meaning that once they have been determined they can be used predict the cross sections at other colliders like RHIC and in the future the Large Hadron Collider.

It would be an oversight not to mention the color evaporation model. The color evaporation model predates the color singlet model, and can describe photoproduction and hadroproduction of charmonium data well [Amu 97]. The color evaporation model ignores the charmonium color over short distances, and the appearance of a color singlet observable state depends on many soft gluon emissions over a long distance. Thus, the color evaporation model employs a factorization into the perturbative production mechanism and the non-perturbative hadronization of the pair into a charmonium state. The production of ψ (meaning J/ψ and ψ') final states is represented as

$$\sigma_\psi = \rho_\psi \sigma_{\text{onium}} \tag{1.3}$$

where σ_{onium} is the sum of the cross sections for all onium states and is computed from perturbative QCD. ρ_ψ is the fraction of the onium states which materialize as ψ's, and this parameter must be determined empirically.

There is great interest in the study of charmonium production in a QGP en-

vironment. In 1986 Matsui and Satz theorized that in a QGP, there would be significant color screening, which interferes with the creation of bound charmonium states [Mat 86]. In a QGP, large numbers of free quarks and gluons reduce the long distance effects of the color force, decreasing the probability that a charm and anticharm quark will bind into a charmonium state. Indeed, such suppression was observed by the CERN NA50 experiment in Pb-Pb collisions at $\sqrt{s_{NN}} = 17.3$ GeV [Abr 97][Abr 00], although whether the QGP was actually created at CERN is much debated. Figure 1.4 shows the observed suppression of J/ψ production as a function of energy density. The suppression is obtained by taking the observed cross section divided by the expected value after considering nuclear absorption. In a dense nuclear medium, nuclear absorption occurs when multiple scattering of the bound charmonium state within the nuclear matter increases the probability that the pair will dissociate into open charm. There is significant suppression observed for energy densities above 2.2 GeV/fm^3, and this has been attributed to charmonium melting due to deconfinement in the QGP. However, arguments have been made that the observed suppression can be explained with the expected suppression from alternative nuclear absorption models and the effect does not require the creation of a QGP [Qui 98].

PHENIX can perform this measurement at a center of mass energy of $\sqrt{s_{NN}} =$ 200 GeV, much higher than the measurement from CERN at $\sqrt{s_{NN}} = 17.3$ GeV. The CERN energy is thought to be just above the threshold for production of

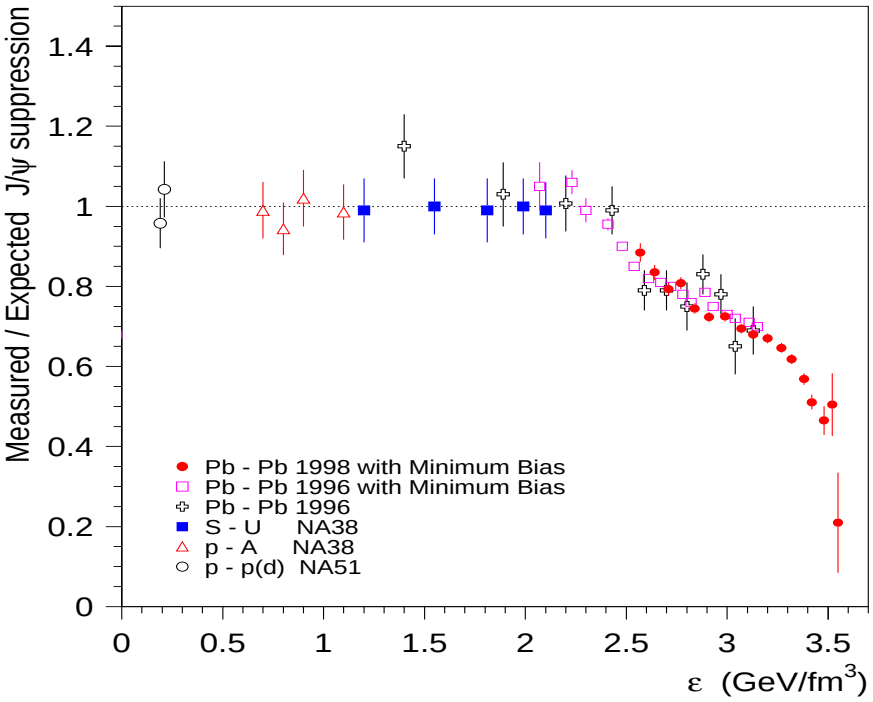

Figure 1.4: J/ψ suppression observed at NA50 as a function of energy density (taken from [Abr 00]).

a QGP, meaning that if the QGP is created, it will be short lived and have a relatively low temperature. Because of this, the signatures of QGP observed at CERN may be difficult to identify, and it is generally agreed that the higher energies of RHIC are needed to verify the existence of the QGP and to definitively confirm its existence. The QGP produced at RHIC can be expected to last much longer at higher temperatures and energy densities compared to CERN energies.

Several competing theories for charmonium production in a QGP at RHIC exist. One theory predicts that there will be absorption of J/ψ in the QGP due

to a combination of color screening and dissociation by gluon collisions [Zha 00]. A different theory suggests an enhancement factor in the range 1.2 to 5.5 for J/ψ production at RHIC [The 01]. This model theorizes that, if a region of deconfined quarks and gluons is formed, a new mechanism for charmonium bound states will become important. The mobility of heavy quarks within this deconfined region would allow a quark and antiquark from different nucleon collisions to form a bound state. Previous models have assumed that bound states are formed only in the initial nucleon collision. In the enhancement model, leftover quarks which do not form bound states in the initial nucleon collison would be able to join with quarks from other nucleon collisions inside of the deconfined region, thereby forming additional bound states. To distinguish between such different theoretical scenarios, a measurement of charmonium production in a QGP is clearly needed.

1.2 Charmonium Polarization

A polarization measurement is a very important test of the NRQCD theory for charmonium production. Each model for charmonium production (color evaporation model, color singlet model, and NRQCD with color octet mechanisms) predicts a unique value for the polarization. Theoretically, the polarization parameter can range from -1 for completely longitudinal polarization ($J_z = 0$) to +1 for completely transverse polarization ($J_z = \pm 1$). Polarization for charmonium using the color singlet model has been studied in [Van 95]. For direct color singlet

production the polarization is predicted to be $\sim$0.25. However, as has already been discussed, the color singlet model has been superceded by more advanced theories which include color octet contributions.

In the color evaporation model, transitions ${}^3S_1 \rightarrow {}^1S_1$ are not suppressed due to large numbers of gluon interactions. Any polarization of the charmonium is destroyed. Therefore, in the color evaporation model the polarization is predicted to be zero.

In NRQCD theory, large p_t charmonium production is expected to be dominated by color octet gluon fragmentation. When $p_t \gg 2m_c$ the fragmenting gluon is transversly polarized. The soft gluon emission which takes the color octet state to the color singlet state does not change the spin due to heavy quark spin symmetry, and the transverse spin is carried through to the final state. Heavy quark spin symmetry results from the fact that in NRQCD the spin of the heavy quark is conserved at leading order in v^2. Thus, for ψ' produced at large p_t via the gluon fragmentation process, the polarization from NRQCD theory is expected to be nearly 100% transverse [Cho 95]. J/ψ production is contaminated by feed down from higher states (χ_c, ψ'). The χ_c states are produced in various spin states and decay to J/ψ through radiative processes, complicating the calculation for the polarization of J/ψ. This contamination decreases, but does not eliminate, the transverse polarization at high p_t [Bra 00].

There have been several fixed target experiments (E537, E672/706, E771,

Chicago-Iowa-Princeton) and one collider experiment (CDF) at Fermilab, which have measured charmonium polarization. E537, E672/706, and E771 did not measure significant polarization. Chicago-Iowa-Princeton measured no polarization except for one data point at large x_F , which showed longitudinal polarization. The CDF experiment was in agreement with QCD predictions for J/ψ polarization at moderate p_t ranges, but showed longitudinal polarization at large p_t, in disagreement with predictions [Aff 00]. The error bars for the ψ' data are too large to make any definitive statements. Prompt J/ψ's are defined as being produced either directly or from decays of χ_c and ψ, but do not include decays of B hadrons. For prompt J/ψ's at the Tevatron, about 36% of the prompt component is from χ_c and ψ decays. The theoretical prediction for prompt J/ψ and ψ' polarization at the Tevatron along with the data from the CDF collaboration is shown in Figure 1.5, where the polarization parameter α is plotted as a function of p_t.

1.3 Open Heavy Flavor Production

Open heavy flavor production in polarized pp collisions can be used to study the polarization of the gluon [Kar 94]. The gluon polarization is particularly interesting in light of the "spin crisis," the observation that only a small fraction of the spin of the nucleon comes from the valence quarks [Ash 88]. Subsequently, the idea that gluon spin may be significant has been studied theoretically [Jaf 96]. Heavy quark production is expected to be large at RHIC ($\sigma_{c\bar{c}} \approx 200\mu$b, $\sigma_{b\bar{b}} \approx$

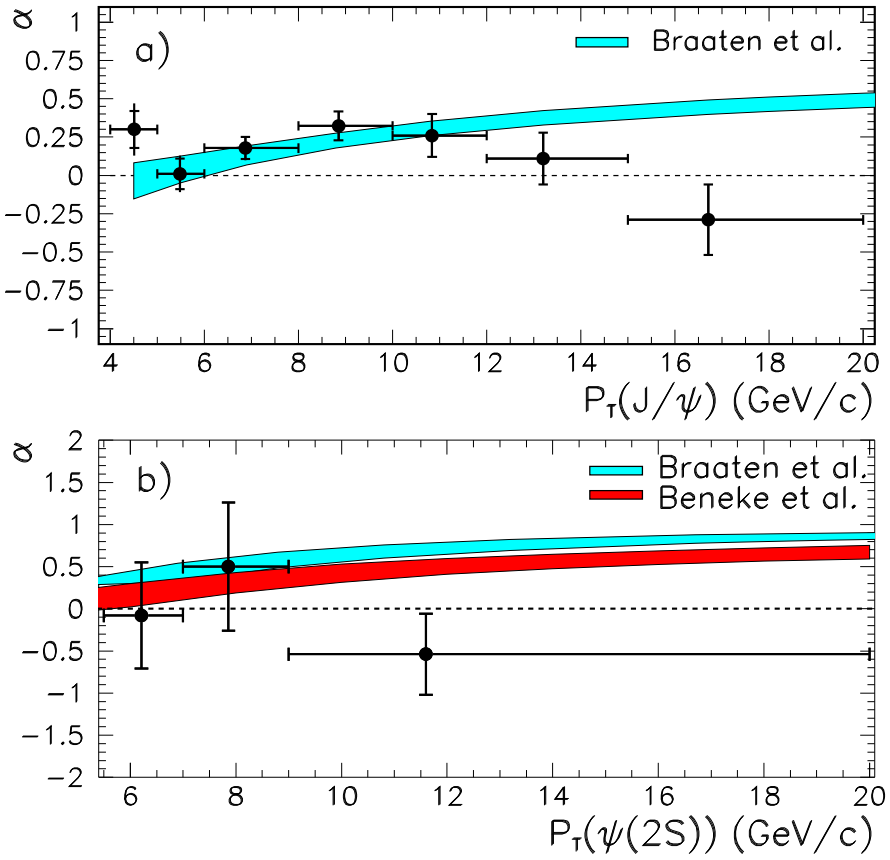

Figure 1.5: Theoretical predictions for prompt J/ψ and ψ' polarization along with the CDF data (taken from [Aff 00]).

2μb at $\sqrt{s} = 200$ GeV), and the decay width to muons is also large. In collisions of polarized beams, conservation of helicity and angular momentum will give rise to an asymmetry in the production cross sections. In general, for two longitudinally polarized beams a double spin asymmetry is defined as

$$A_{LL} = \frac{\sigma^{++} + \sigma^{--} - \sigma^{+-} - \sigma^{-+}}{\sigma^{++} + \sigma^{--} + \sigma^{+-} + \sigma^{-+}} \tag{1.4}$$

where + and - indicate the helicity state of the nucleon in the polarized beam. For example, σ^{++} is the cross section for the process of interest when the colliding nucleons have parallel spins and positive helicities. σ^{+-} indicates that the colliding nucleons have anti-parallel spins: one nucleon has positive helicity, and the other nucleon has negative helicity. Open heavy flavor production by gluon fusion is known to dominate over quark antiquark fusion at RHIC energies. Figure 1.6 depicts the fusion process, showing how the muons are derived from an intermediate $D^o\bar{D}^o$ state. The process for open bottom production is identical, except it proceeds via an intermediate $B^o\bar{B}^o$ state. The double spin asymmetry for open heavy flavor production can then be written as [Kar 94]

$$A_{LL}(x_1x_2) = \frac{\Delta G}{G}(x_1)\frac{\Delta G}{G}(x_2)\hat{a}_{LL}(\hat{s},\hat{t},\hat{u}) \ . \tag{1.5}$$

$\hat{a}_{LL}(\hat{s},\hat{t},\hat{u})$ is the parton level asymmetry for the gluon fusion process $gg \to q\bar{q}$ in terms of the Mandelstam variables. $\Delta G \equiv \int_0^1 \mathrm{d}x\Delta G(x,Q^2)$, where $\Delta G(x,Q^2) = G_+(x,Q^2) - G_-(x,Q^2)$, and $G_+(G_-)$ is the distribution for a polarized gluon with helicity parallel (antiparallel) to the parent nucleon helicity.

A study of heavy flavor production in the south muon arm has been done [Bro 98]. The parton level asymmetry $\hat{a}_{LL}(\hat{s},\hat{t},\hat{u})$ becomes large enough (~ -0.6) to perform the measurement when $p_t \geq 6$ GeV. To study open heavy flavor production it is necessary to separate the muons from heavy flavor decay from the muons coming from pion and kaon decay. There are two features of the single

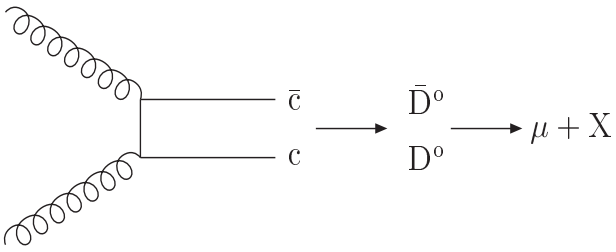

Figure 1.6: Gluon fusion process, which dominates open heavy flavor production at RHIC.

muon spectrum which can potentially be used to eliminate the background. Figure 1.7 shows the spectrum of single muons as a function of p_t from pp collisons in the south muon arm from charm, beauty, and pion decay simulated with the PYTHIA event generator at $\sqrt{s} = 200$ GeV and an integrated luminosity of 8x10^{38} cm^{-2}. At high p_t, muons from charm and beauty decay dominate the spectrum over pion decays, indicating that a p_t cut may be appropriate for selecting heavy flavor decays. A second feature of the single muon spectrum which can potentially aid in determination of the background is an asymmetry in the event vertex distribution. Pions and kaons which emanate from vertices at some distance away from one of the muon arms experience a longer decay path than those pions and kaons eminating from vertices closer to that muon arm. This longer decay path translates into a higher probability that the pion or kaon will decay to a muon before reaching the absorbing material of the muon arm. Thus, the vertex distri-

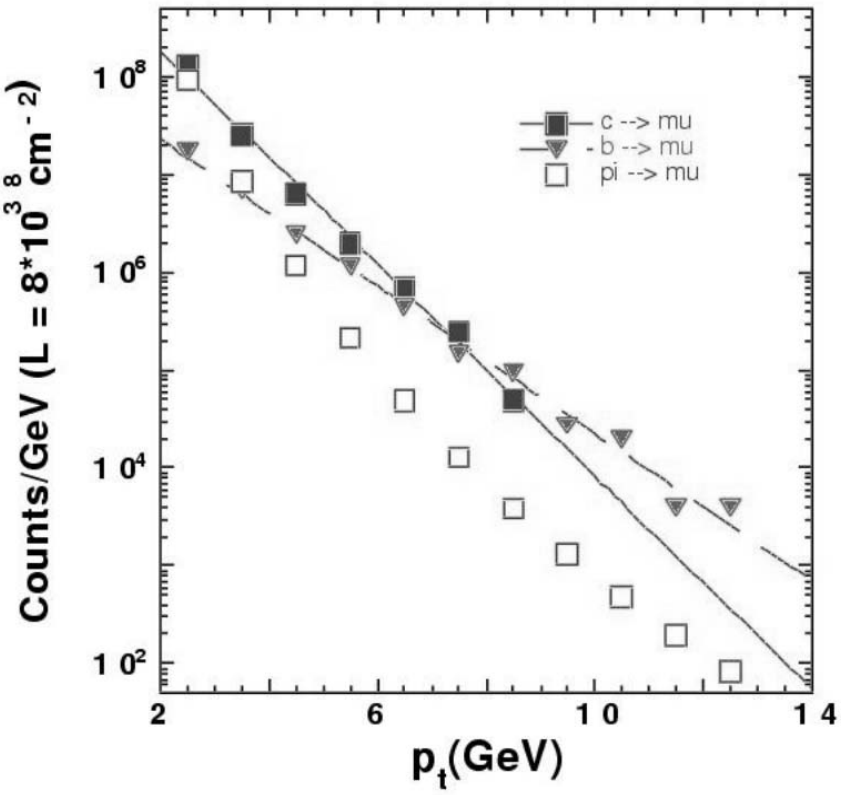

Figure 1.7: Contributions to the single muon spectrum from charm, beauty, and pion decay (taken from [PHE 94]).

bution from pion and kaon decays exhibits a mean centroid which is shifted away from the muon arm. In principle, a relation between the vertex centroid and the fraction of muons coming from pion and kaon decays could be determined and utilized as a correction to the heavy flavor spectrum.

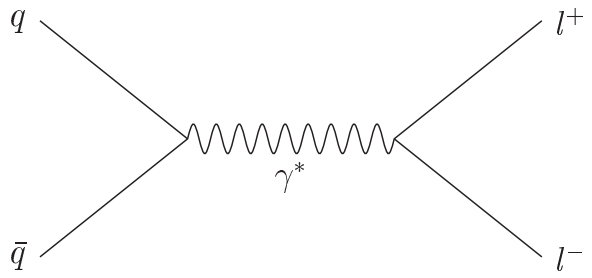

Figure 1.8: Drell-Yan production mechanism.

1.4 Polarized Drell-Yan Production

Polarized Drell-Yan production, shown in Figure 1.8, provides a very direct way to measure the antiquark helicity distributions of the nucleon [Dre 99]. The process produces a dilepton pair, making it suitable for study with the muon spectrometer via the detection of dimuons. A measurement by the Fermilab E866 experiment has observed that $\bar{d} > \bar{u}$ in the nucleon sea [Tow 01], which has increased interest in the study of the flavor asymmetry. The double spin asymmetry in the Drell-Yan process is sensitive to the antiquark helicity distributions. The double spin asymmetry is given by [Kam 98][Sof 98]

$$A_{LL}(x_1, x_2) = \frac{\sum_a e_a^2[\Delta q_a(x_1)\Delta\bar{q}_a(x_2) + \Delta q_a(x_2)\Delta\bar{q}_a(x_1)]}{\sum_a e_a^2[q_a(x_1)\bar{q}_a(x_2) + q_a(x_2)\bar{q}_a(x_1)]} \ . \tag{1.6}$$

For ranges of $x_F \geq 0.2$, the x dependence of the structure functions (shown in Figure 1.9) causes the denominator of Equation 1.6 to be dominated by the term $q_u(x_1)\bar{q}_u(x_2)$. Recall that $x_F = x_1 - x_2$, and if x_F is large, then x_1 is large and x_2

is small. As seen in Figure 1.9, the probability of finding a valence quark at large x is high, whereas the probability of finding a sea antiquark at large x is small. Thus, the term $q_a(x_1)\bar{q}_a(x_2)$ dominates the term $q_a(x_2)\bar{q}_a(x_1)$. Furthermore, $q_u(x)$ dominates over $q_d(x)$. In the numerator, the same argument causes the term $\Delta q_a(x_1)\Delta\bar{q}_a(x_2)$ to dominate the term $\Delta q_a(x_2)\Delta\bar{q}_a(x_1)$. Equation 1.6 can then be simplified (using the notation $q_u(x) \equiv u(x)$, $q_d(x) \equiv d(x)$) to

$$A_{LL}(x_1, x_2) \approx \frac{\Delta u(x_1)}{u(x_1)}\frac{\Delta \bar{u}(x_2)}{\bar{u}(x_2)} + \frac{1}{4}\frac{\Delta d(x_1)}{u(x_1)}\frac{\Delta \bar{d}(x_2)}{\bar{u}(x_2)} \ . \tag{1.7}$$

Then, introducing approximate expressions for the Deep Inelastic Scattering structure functions (recall that $g_1^p(x) = \frac{2}{9}\Delta u(x) + \frac{1}{18}\Delta d(x)$, $g_1^n(x) = \frac{2}{9}\Delta d(x) + \frac{1}{18}\Delta u(x)$, and $F_1^p(x) = \frac{2}{9}u(x) + \frac{1}{18}d(x)$):

$$u(x) \approx \frac{9}{2}F_1^p(x) \ , \tag{1.8}$$

$$\Delta u(x) = \frac{18}{15}(4g_1^p(x) - g_1^n(x)) \ , \tag{1.9}$$

$$\Delta d(x) = \frac{18}{15}(-g_1^p(x) + 4g_1^n(x)) \ , \tag{1.10}$$

Thus, Equation 1.7 can be further simplified to

$$A_{LL}(x_1, x_2) \approx A_{LL}^{DIS}(x_1)[\frac{16}{15}\frac{\Delta \bar{u}}{\bar{u}}(x_2) - \frac{1}{15}\frac{\Delta \bar{d}}{\bar{u}}(x_2)] \ , \tag{1.11}$$

where $A_{LL}^{DIS}(x) = \frac{g_1(x)}{F_1(x)}$ is the Deep Inelastic Scattering asymmetry. The simplification to Equation 1.11 also requires that $g_1^n \approx 0$ for $x \geq 0.2$, which is satisfied as shown in Figure 1.10. A further simplification can be made if one assumes

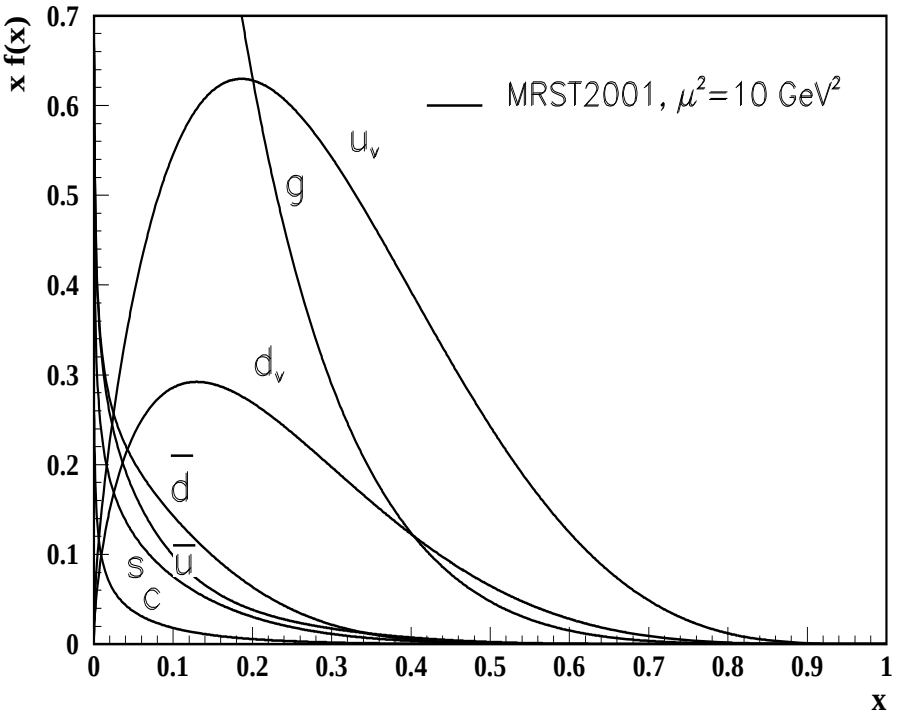

Figure 1.9: Dependence of quark structure functions on x (taken from [Hag 02]).

$\Delta\bar{u} = \Delta\bar{d}$. Then Equation 1.11 becomes

$$A_{LL}(x_1, x_2) \approx A_{LL}^{DIS}(x_1)\frac{\Delta\bar{u}}{\bar{u}}(x_2) \ . \tag{1.12}$$

The asymmetry is now a measure of the antiquark helicity distribution in the proton at x_2. It may be preferable to perform the measurement at energies of $\sqrt{s}$ = 50 GeV, because charm decay becomes a serious source of background at $\sqrt{s}$ = 200 GeV.

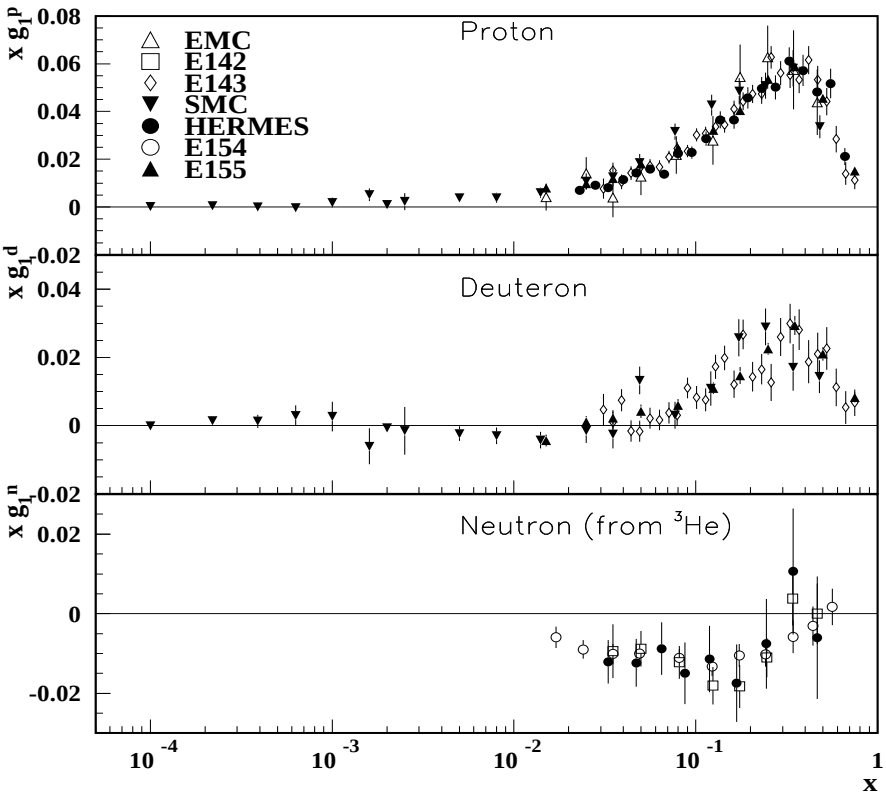

Figure 1.10: $g_1(x)$ structure function from deep inelastic lepton scattering from several experiments. Data for the neutron is shown in the bottom panel. (taken from [Hag 02]).

1.5 $W^{\pm}$ Production

$W^{\pm}$ production is also a probe of the polarized quark structure functions, and the measurement is complementary to the polarized Drell-Yan process. In the Standard Electroweak Model, $W^{\pm}$ production occurs via a purely left-handed current. The parity violating single spin asymmetry (requiring only one polarized

beam to measure) for W^+ production is [Sof 98]

$$A_L^{W^+}(x_1, x_2) = \frac{-u(x_1)\Delta\bar{d}(x_2) + \bar{d}(x_1)\Delta u(x_2)}{u(x_1)\bar{d}(x_2) + \bar{d}(x_1)u(x_2)} \ . \tag{1.13}$$

One simply interchanges the quark flavors ($u \leftrightarrow d$) to get the formula for W^- production. An interesting aspect of $W^\pm$ production is the ability to select which flavor of quark or antiquark one wishes to study by placing cuts on $x_{_F}$ and choosing either the W^+ or W^- channel. For large $x_{_F}$, in Equation 1.13 the terms containing $\bar{d}(x_1)$ are small, and in the corresponding equation for W^- the terms containing $\bar{u}(x_1)$ are small. Thus, the asymmetries reduce to

$$A_L^{W^+}(x_1 \gg x_2) \approx -\frac{\Delta\bar{d}(x_2)}{\bar{d}(x_2)} \ , \tag{1.14}$$

$$A_L^{W^-}(x_1 \gg x_2) \approx -\frac{\Delta\bar{u}(x_2)}{\bar{u}(x_2)} \ . \tag{1.15}$$

Similarly, if one chooses the negative $x_{_F}$ range, in Equation 1.13 the terms containing $u(x_1)$ are small, and for the W^- case the terms containing $d(x_1)$ are small. This leads to the approximations

$$A_L^{W^+}(x_1 \ll x_2) \approx -\frac{\Delta u(x_2)}{u(x_2)} \ , \tag{1.16}$$

$$A_L^{W^-}(x_1 \ll x_2) \approx -\frac{\Delta d(x_2)}{d(x_2)} \ . \tag{1.17}$$

The measurement technique utilizes the detection of high p_t single muons. The main background at high p_t is from decays of heavy quarks. Figure 1.11 shows a PYTHIA simulation for muon decays from heavy flavor, W bosons, and Z bosons

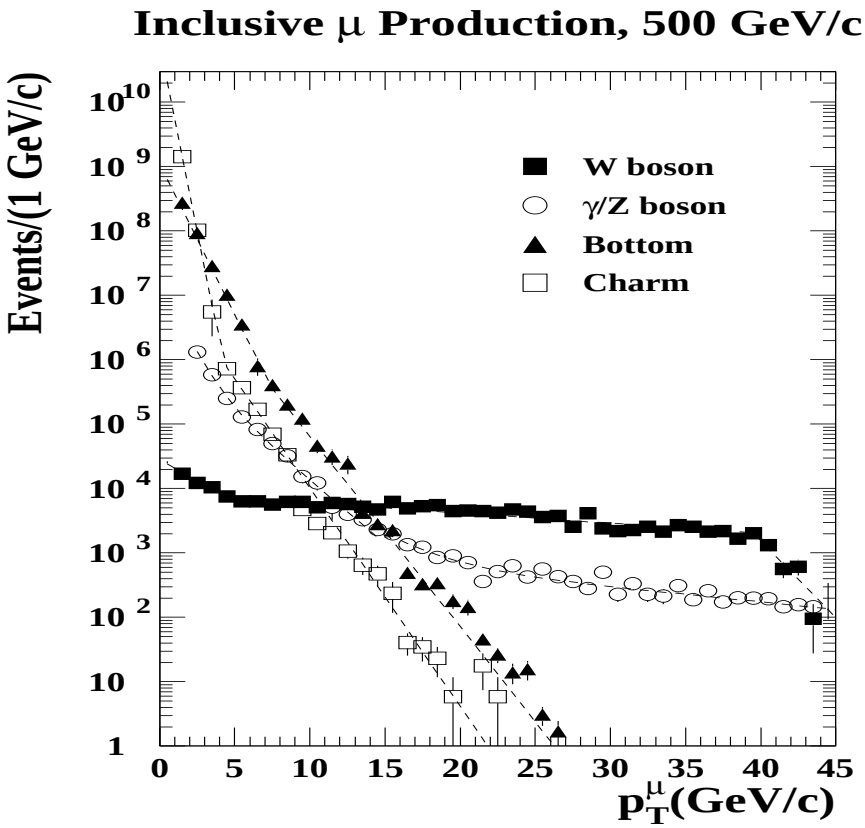

Figure 1.11: PYTHIA simulation for muon decays from heavy flavor, W bosons, and Z bosons (taken from [Sai 95]).

in the PHENIX muon spectrometer at $\sqrt{s} = 500$ GeV using an integrated luminosity of 2x10^{39} cm^{-2}. Clearly, for $p_t \geq 25$ GeV the single muon spectrum is dominated by W boson decay.

1.6 Melting Order of Quarkonium

The production rates of Υ, ψ', and J/ψ may provide a signature of the production of a QGP. Bound states of heavy quarks are expected to experience Debye color screening in a QGP [Gao 90]. If the bound state radius is larger than the Debye screening length the bound state cannot exist. Because the radii of Υ, ψ', and J/ψ are related by $\mathrm{r}(\Upsilon) < \mathrm{r}(\mathrm{J}/\psi) < \mathrm{r}(\psi')$, the temperature at which these onium states experience dissociation may also follow this relation [Mül 95]. Other effects contribute to the overall dissociation process, such as the relative binding energies, dynamic fermions, high energy gluons, and increased probablilites for dissociation of intermediate D states in the charmonium decay. The net effect is that excited charmonium states ψ' and χ_c should dissociate immediately upon reaching the critical temperature for deconfinement ($T_c \approx 170$ GeV), the J/ψ is expected to dissociate at $\frac{T}{T_c} \approx 1.2$, and the Υ is expected to dissociate at $\frac{T}{T_c} \approx 2.5$. Global variables such as the average transverse momentum $\langle p_t \rangle$, the rapidity distribution of the hadron multiplicity $\frac{\mathrm{d}N}{\mathrm{d}y}$, and the rapidity distribution of the transverse energy $\frac{\mathrm{d}E_t}{\mathrm{d}y}$, are quantities sensitive to the formation of a QGP. In particular, $\frac{\mathrm{d}N}{\mathrm{d}y}$ is related to the energy density, which scales like T^4 in a QGP [McL 85] . Thus, a study of the relative production rates of Υ, ψ', and J/ψ as a function of the hadron multiplicity and energy density can serve as a QGP probe.

1.7 Strangeness Enhancement

It has been suggested that there will be significant enhancement of strangeness in a QGP [Raf 82]. s and $\bar{s}$ quarks will be produced mainly by gluon collisions in a QGP, and the strange quark abundance will saturate on a time scale comparable to the lifetime of the plasma ($\sim 2\text{x}10^{-23}\ s$). The strangeness abundance would be reflected in an enhanced production rate of strange mesons, such as the ϕ, which is an $s\bar{s}$ state. An observable quantity which can study enhanced ϕ production is a comparison of the relative production rates of ϕ compared to ρ or ω [Sho 85]. This ratio has been observed at $\sim$0.05 for proton-proton collisions [Dri 81]. The relative suppression of ϕ production compared to ρ and ω is due to the Okubo-Zweig-Iizuka (OZI) rule, requiring that transitions proceed via connected quark diagrams [Fra 77]. In a QGP, abundant s and $\bar{s}$ quarks would form ϕ mesons during the hadronization period, and would not be suppressed by the OZI rule since the quarks are deconfined. The production ratio ϕ/ω in a QGP is predicted to increase by an order of magnitude compared to the proton-proton collision case [Sho 85]. The decay of ϕ to dimuons provides a way to study this. In addition, the ϕ meson has a small cross section for scattering from non-strange hadrons, meaning that the ϕ may carry information about the hadronization phase of the QGP.

1.8 Muon Spectrometer Design Requirements

As discussed in the previous sections, the physics program of the PHENIX muon spectrometer is broad and ambitious. The physics goals place certain requirements on the design of the detector. The detector must be able to perform in both *pp* and Au-Au collisions, where multiplicities and event rates can vary substantially. The signal to background rates and detector acceptance must be large enough to collect significant statistics for a wide variety of physics processes. To allow for the study of $W^{\pm}$ physics, determination of particle charge up to a momentum of ~ 50 GeV is needed. A mass resolution of 100 MeV at the J/ψ mass is required to separate J/ψ from ψ'. A mass resolution of 200 MeV at the Υ mass is required to separate $\Upsilon(1S)$ from $\Upsilon(2S+3S)$. These resolution goals translate into a spatial resolution requirement of 100 μm in the tracking chambers. The muon identifier portion of the spectrometer will provide π/μ rejection (fraction of pions misidentified as muons) of $\sim 2.5\text{x}10^{-4}$.

2 DETECTOR SPECIFICATIONS

A diagram of the RHIC complex is shown in Figure 2.1. The basic components are a Tandem Van de Graaff accelerator, a proton source and LINAC, the Alternating Gradient Synchrotron (AGS), and the RHIC acceleration and storage ring. Gold ions are initially accelerated in the Van de Graaff where the atomic electrons are partially stripped off. A booster performs additional stripping before injecting the ions into the AGS. The AGS accelerates the ions to ∼10 GeV/nucleon before injecting them into the RHIC rings. RHIC then performs the final acceleration to 100 GeV/nucleon. Protons are generated at the proton source, accelerated by the LINAC, injected to the AGS by the booster, injected to RHIC at ∼28 GeV, and undergo a final acceleration to 250 GeV. The design luminosity is $\sim 10^{26}$ cm^{-2}s^{-1} for Au beams, and $\sim 10^{31}$ cm^{-2}s^{-1} for proton beams. The storage lifetime is ∼10 hours.

There are six interaction points equally spaced around the collider ring where collisions can occur. One of these interaction points is occupied by the PHENIX detector. The PHENIX detector, shown in Figure 2.2, is quite large and complex. PHENIX is designed to study the QGP and perform measurements of nucleon spin physics via a variety of physics channels. The detector will sample data from *pp*, *p*A, and AA collisions. PHENIX is composed of two central arms at mid-rapidities, and two muon arms at forward rapidities. Figure 2.3 shows the rapidity and ϕ

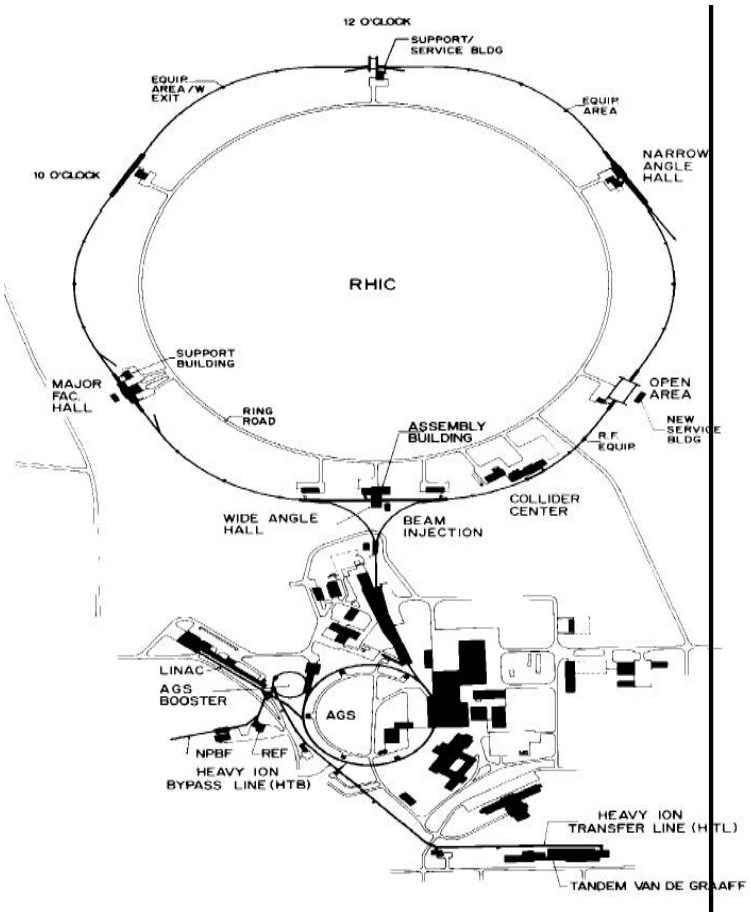

Figure 2.1: Overview of the RHIC accelerator complex.

angle coverage of the PHENIX detectors. The central arms utilize many different detector technologies designed to detect hadrons, electrons, and photons. The central arms include drift chambers, pad chambers, time expansion chambers, ring imaging Cherenkov detectors, time of flight detectors, and electromagnetic calorimeters. Three detectors, the zero degree calorimeters, beam-beam counters, and the multiplicity/vertex detector, provide global measurements to characterize

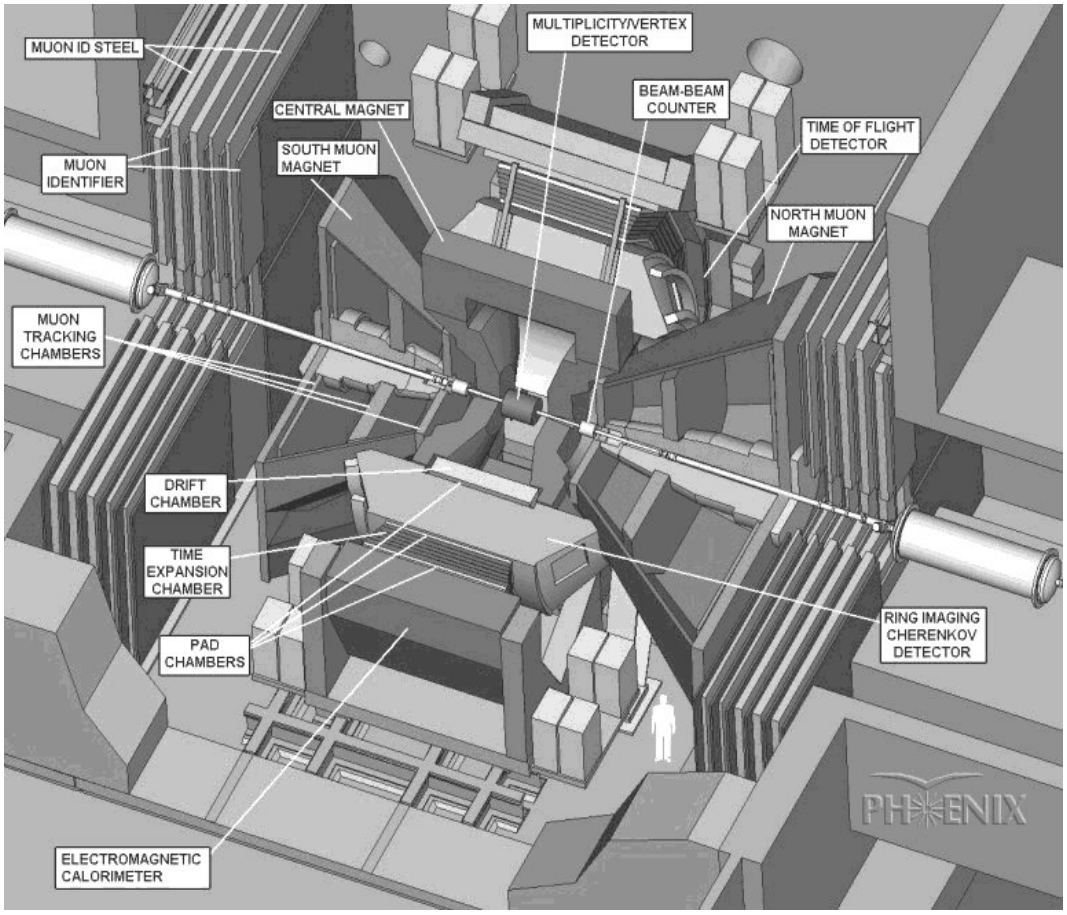

Figure 2.2: Overview of the PHENIX detector.

the collisions. These global measurements include the rapidity distribution for charged particles and the total event multiplicity. The north and south arms of PHENIX are dedicated to the detection of muons. Figure 2.4 shows a depiction of the north muon arm and its relation to the PHENIX central magnet. The south arm is similar. There are two large magnets each containing three stations of tracking chambers which comprise the two muon trackers (MuTr), and interleaved

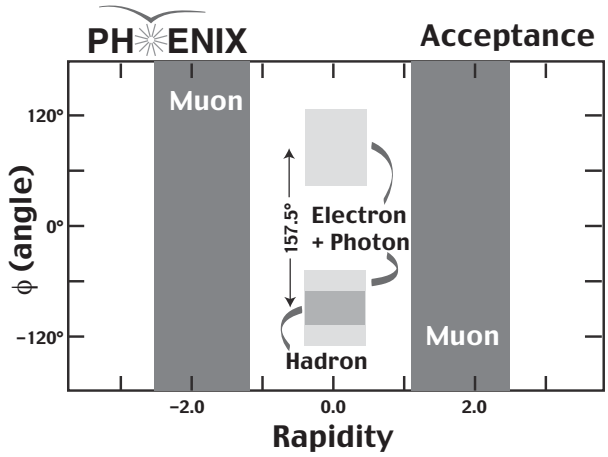

Figure 2.3: Rapidity and ϕ angle coverage of the PHENIX detector.

steel and proportional tube counters which comprise the two muon identifiers (MuId). The range of rapidity coverage is -2.2 $< y <$ -1.2 for the south arm, and 1.2 $< y <$ 2.4 for the north arm. The design aspects of the PHENIX muon spectrometer arm have been discussed in great detail in [PHE 98] and [Aki 03]. The remainder of this chapter will highlight the most important aspects of the spectrometer design.

2.1 Muon Magnets

The north muon magnet was designed to have a p_t kick of 200 MeV/c and $\int B \cdot \mathrm{d}l = 0.72$ Tm at $\theta = 15^{\circ}$. The south arm was added to the PHENIX detector after the original design, and therefore had to be slightly smaller than the north arm. The south arm is also able to be moved out of the interaction hall on tracks.

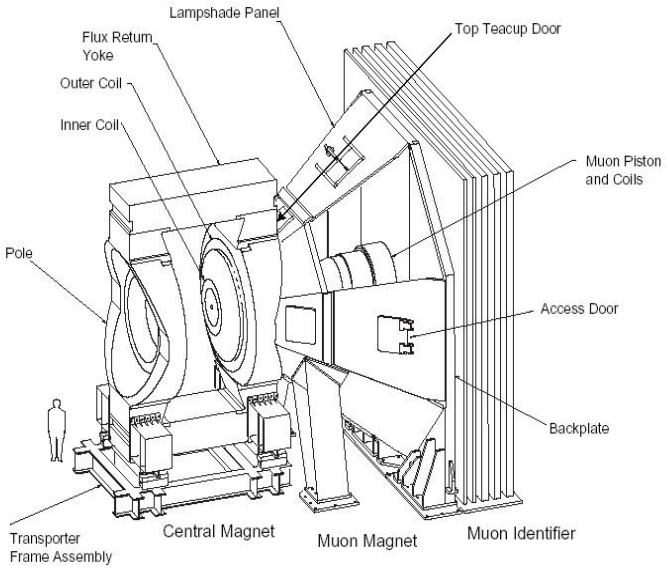

Figure 2.4: Depiction of the PHENIX north muon arm and central magnet.

The south arm was designed to have $\int B \cdot \mathrm{d}l = 0.76$ Tm at $\theta = 15^{\circ}$. Each magnet is eight-sided, and the top five steel panels are removable. The panels are referred to as "lampshades." With all lampshade panels installed, the interior of the north magnet can be accessed via a small access door, whereas the interior of the south magnet is not accessible.

The field is radial, traveling from the lampshade panels to the magnet piston for the south arm, and in the opposite direction for the north arm. Figure 2.5 shows the field lines for the PHENIX central magnet and the two muon arm magnets. The radial field causes particles to follow a spiral-like path as they traverse the magnet. The field strength is typically a few kG. Several types of absorbing

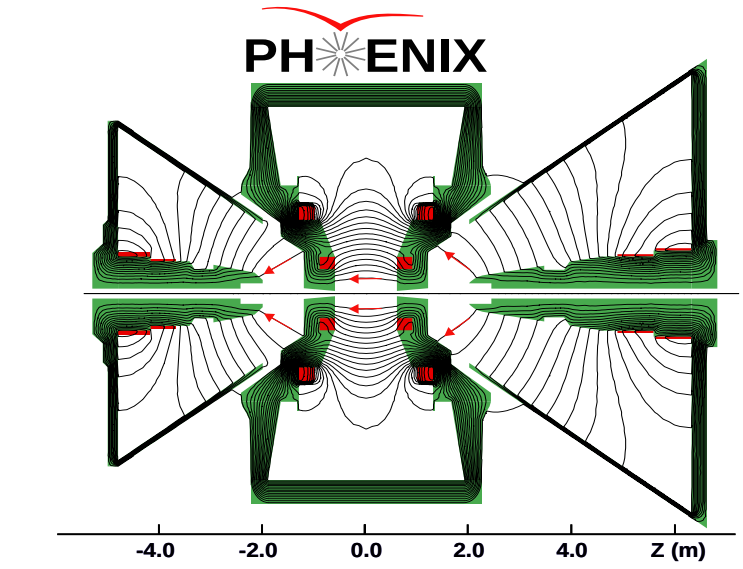

Figure 2.5: Field lines for the PHENIX central and muon magnets. The north arm is on the right.

material are used to reduce the rate of hadron showers. Figure 2.6 shows the location of the absorbing materials in the north arm. The south arm is identical in design, except it has a slightly shorter nosecone. The copper nosecone works in conjunction with the central magnet steel to reduce hadrons from the collision point. The copper insert absorbs hadron showers at small angles to prevent them from hitting the muon magnet piston. The iron plug prevents particles from showering off the muon magnet piston into the first station of tracking chambers.

The position of the second station of tracking chambers is determined by observing where the point of maximum deflection occurs for a track passing through the magnetic field. Figure 2.7 shows the z position of the point of maximum de-

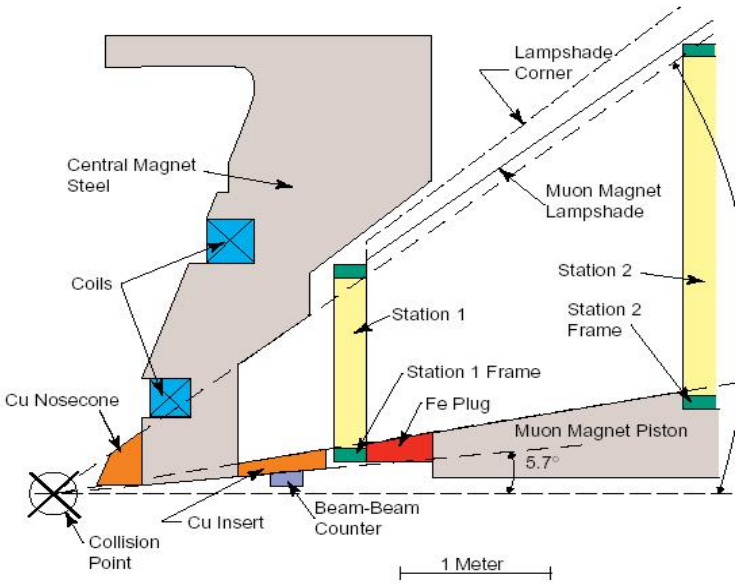

Figure 2.6: Absorbing materials in the north muon magnet. The south arm is similar.

flection for a 10 Gev muon track in the south arm at different θ angles (the z axis is defined to be the beam axis, with z=0 being the collision point). The north arm is similar, but because it is slightly larger the maximum deflection point occurs at a larger z value.

2.2 Muon Tracker Cathode Strip Chambers

There are three stations of tracking chambers. The construction is that of a conventional wire chamber, using cathode strips and anode wires at high voltage in an ionizing gas medium. Station 1 and 3 chambers have identical design, whereas station 2 empolys a different construction to minimize multiple scattering. Figure 2.8 depicts the construction technique for the station 1 and 3 chambers. Anode

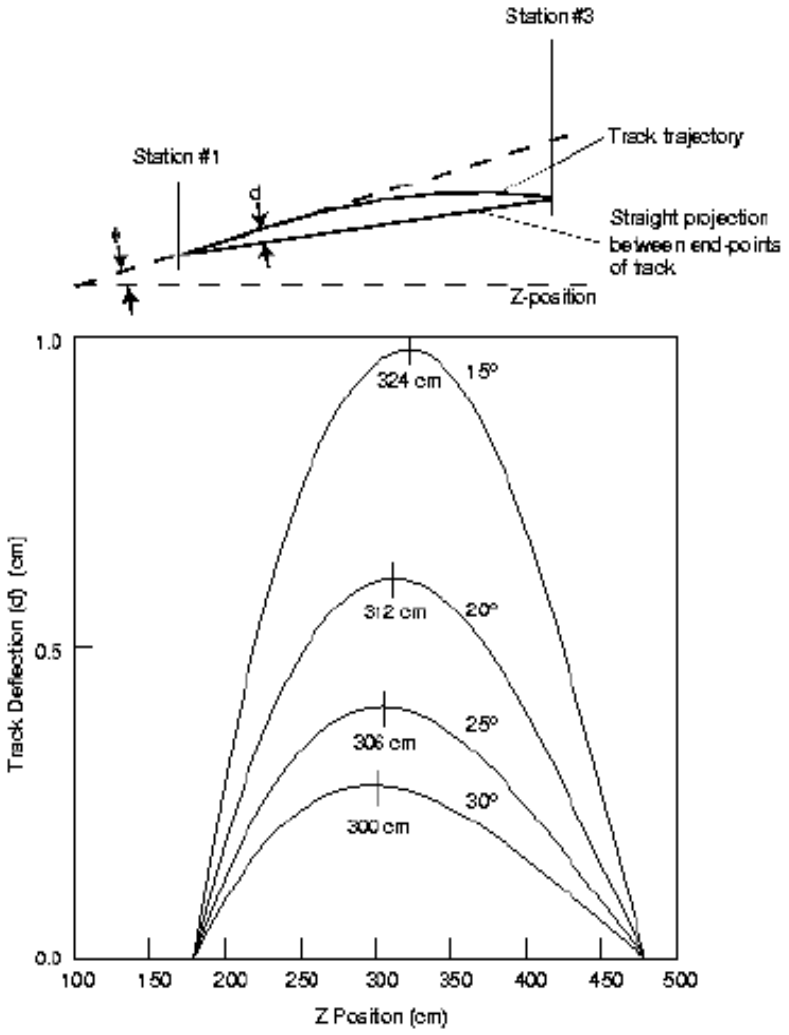

Figure 2.7: Point of maximum track deflection for 10 GeV muons in the south arm.

wires are sandwiched between two cathode strip planes. The anode wires alternate between field and sense wires. The chamber cathode planes are fabricated from copper clad FR4 honeycomb panels, and an etching machine is used to create strips in the copper coating. The cathode strip width is 1 cm, and every other strip is

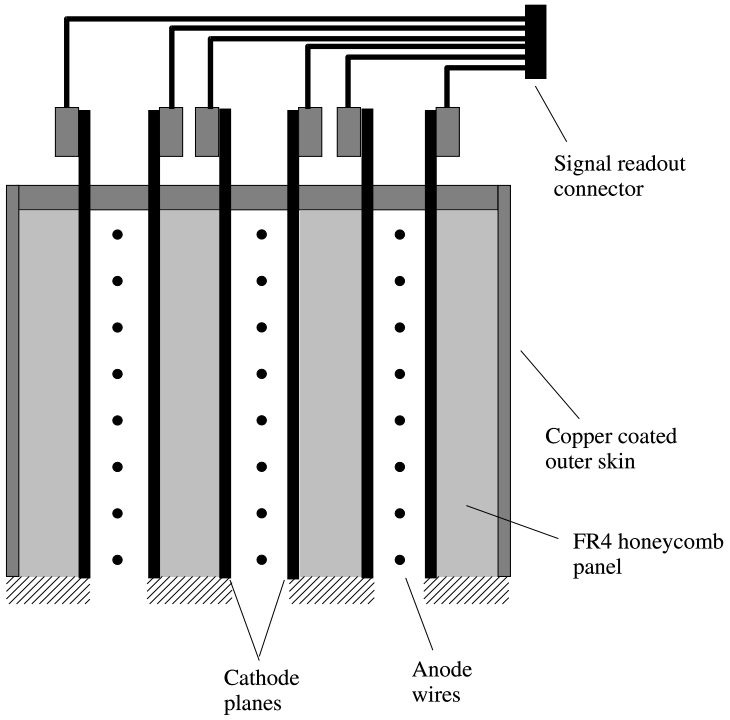

Figure 2.8: Basic chamber design for station 1 and 3 chambers.

read out. The signals from each plane are routed to a common readout connector. The construction of the station 2 chambers is designed for minimum thickness ($\leq$0.1% of a radiation length) to allow for good resolution at small momentum. The materials used for the station 2 cathode planes are copper coated mylar foils with etched strips. The chambers each have six cathode planes and three anode planes. The anode planes use 20 μm gold plated Tungsten sense wires, and 75 μm gold plated Cu-Be field wires. The sense wire spacing is 10 mm. Two cathode planes and one anode plane form a "gap," so that each chamber has three gaps.

All three gaps are read out at stations 1 and 2, but only 2 gaps are read out at station 3. Readout of one plane in station 3 was descoped from the project for budgetary reasons.

Station 1 is the smallest of the three stations, with a length of $\sim$1.25 m, and is located closest to the collision vertex. Station 1 is divided into four detector segments, called "quadrants." The station 2 chambers are $\sim$1.9 m in size. Station 2 is divided into eight "octants." The station 3 chambers have the same construction design as station 1, with a size of $\sim$2.4 m. Station 3 is also divided into eight octants. Fig. 2.9 shows how the eight octants are arranged into a chamber to provide complete azimuthal coverage. The size of the chambers quoted here is for the south arm, the north arm chambers are somewhat larger.

The mass resolution of the Υ is influenced by energy straggling and multiple scattering in the absorber material as well as the resolution of the detector. The Υ mass resolution dependence on the chamber resolution comes from the fact that muons from Υ decay typically have moderately large momenta, resulting in a small deflection at station 2. Thus, small uncertainties in the sagitta (maximum deflection of the track momentum) measurement at station 2 can significantly affect the mass resolution. The muons from J/ψ decay have smaller momenta, producing a large deflection at station 2, and therefore the resolution of the J/ψ is dominated by energy straggling and multiple scattering of the muons in the absorbing material before entering the detector. For this reason, the chamber

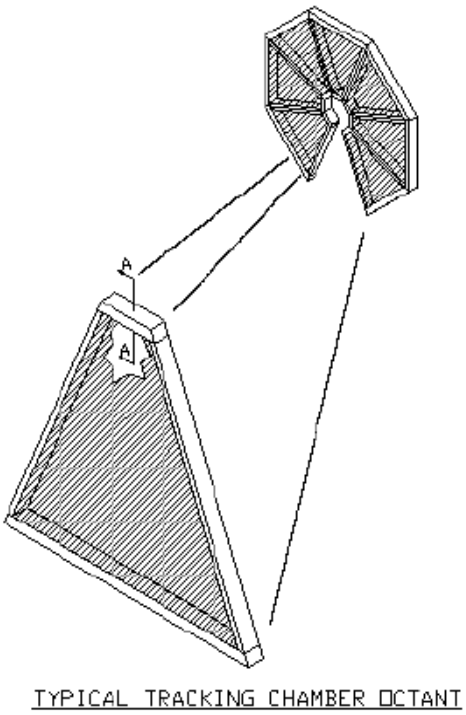

Figure 2.9: Arrangement of eight chamber octants to form a tracking station.

resolutions are studied using the Υ decay.

To acheive an Υ mass resolution of 200 MeV, 100 μm spatial resolution on each of the six cathode planes is required. Position resolution is acheived by orienting some of the cathode planes with the cathode strips perpendicular to the anode wires, and others at angles with respect to the perpendicular ranging up to $\pm 11.25^{o}$. Cathode planes are generally either labeled as "straight" or "stereo." Straight planes have the cathode strips perpendicular to the anode wires, and stereo planes have the cathode strips at an angle with respect to the anode wires.

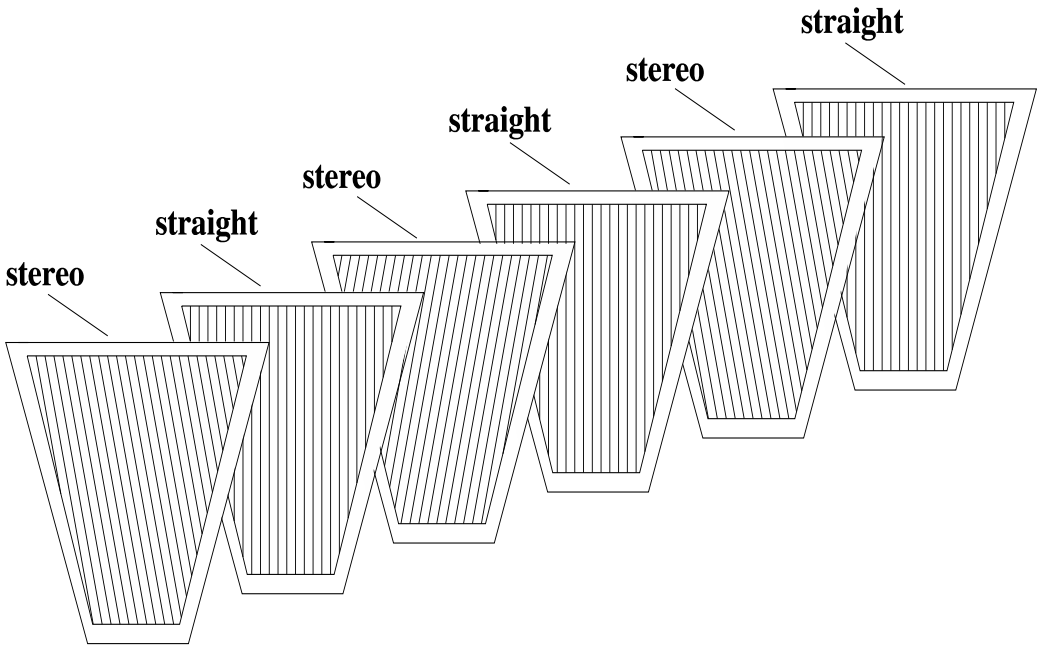

Figure 2.10: Stacking of six cathode planes with different strip orientations to form a chamber.

Figure 2.10 shows an example of how six cathode planes, some straight and some stereo, can be stacked to make a chamber. The stacking order of the chambers for stations 1 and 3 is stereo, straight, stereo, straight..., and for station 2 the order is straight, stereo, straight, stereo... Signals are read out from each cathode plane, and the position of the chamber hit can be determined by finding the location where the hit cathode strips in each plane intersect.

The gas mixture used is Ar:CO_2:CF_4 in the mixture ratio 50%:30%:20%. This gas mixture was chosen because it is non-flammable, has a wide efficiency plateau, produces a charge distribution which is appropriate for our preamplifier chip, has

a reasonable drift time, and has a small Lorentz angle. The Lorentz angle is the angle of the drift of electrons with respect to the electric field. The direction of drift is altered by the magnetic field, creating the Lorentz angle. The size of the Lorentz angle effect depends on the speed of the ionization electrons within the gas, therefore different gases will exhibit unique Lorentz angles depending on the speed of that gas. When the chambers are operated at 1850 V this gas mixture produces a gain of 2x10^4. A minimum ionizing particle produces $\sim 10^5$ electrons in the chamber, which gives a total charge of $\sim$80 fC on the cathode strips.

2.3 Muon Tracker Electronics

The main purpose of the MuTr front end eletronics (FEE) is collection and digitization of the cathode signals read from the wire chambers. There are approximately 46,000 cathode channels in the MuTr spectrometer. To maintain the 100 μm spatial resolution, the noise at the input to the electronics was required to be 0.8 fC for an average input charge of 80 fC.

Most components of the FEE are located inside the large PHENIX muon magnets. Charge from the wire chamber cathode strips travels over a short analog readout cable into a cathode preamplifier chip (CPA). Ideally, the preamplifier chip would be located directly on the wire chambers to reduce noise pickup which can occur when signals travel through cables. In our application space constraints would not permit this.

The CPA chip has 8 channels of charge sensitive amplifiers followed by shaping amplifiers. Inside this chip, the shaping amplifier outputs a voltage signal proportional to the input charge. The gain is 3.5 mV/fC, meaning that a typical input charge of 80 fC will be converted to a pulse of height 280 mV by the preamplifier chip.

This voltage signal is then stored in the analog memory unit of an analog memory unit/analog to digital converter (AMU/ADC) chip. The AMU/ADC chip is 32 channels of analog memory with a 12 bit analog to digital convertor, although in our application we are using it in 11 bit mode, so that the digitized pulse height is encoded as an ADC value between 0 and 2047. The relation between pulse height and the corresponding digitized ADC value is 2 mV $\sim$ 1 ADC count. Therefore, with an 11 bit dynamic range, we can digitize voltages up to $\sim$ 4 V, although saturation in the preampilfier chip becomes a factor at very large values. Digitization of the pulse by the analog to digital converter portion of the chip is controlled by a field programmable gate array (FPGA). The FPGA performs digitization of the pulse upon receipt of a trigger from the PHENIX trigger system. This process creates 64 digitized values of the input pulse sampled every 106 ns (the period of the accelerator beam clock). Figure 2.11 shows the shape of the pulse and the 64 digitized samples for various pulse amplitudes.

From these 64 digitized samples, we choose 4 samples to be transferred to the data collection system of PHENIX for analysis. The location of these samples is

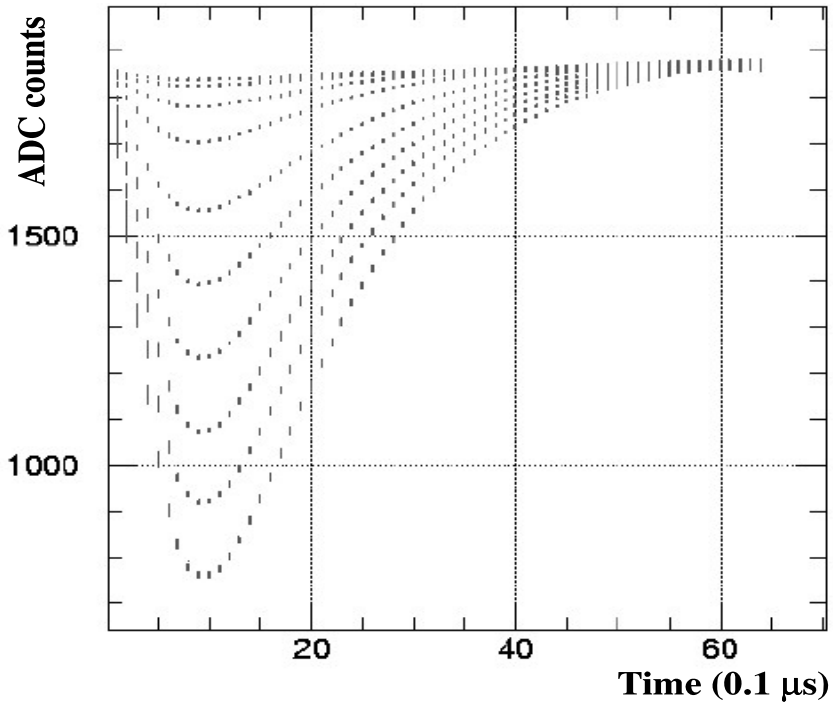

Figure 2.11: Shape of the digitized pulses from the CPA chip for various pulse amplitudes. The ADC value as a function of time is shown.

chosen so that we can obtain the height of the digitized pulse with good accuracy. The 4 samples are required to be digitized in a time period of <40 μs per event to allow the PHENIX data aquisition system to collect data at its design rate. Up to five events can be buffered at one time.

The electronics for the south arm are divided into 168 Front End Modules (FEM), each of which contains 16 cathode preamplifier chips, 4 AMU/ADC chips, 1 FPGA, and 1 ARCNet interface card. An FEM is segmented into one control card, which contains the FPGA and ARCNet card, and two cathode readout

cards (CROC), which contain two AMU/ADC chips and 8 CPA chips each. The control and CROC cards in an FEM are seated in a common backplane. The backplane allows the control and CROC cards to communicate with each other, and also has connectors to accept signal cables from the cathode chambers and cables which allow data flow to and from the PHENIX data aquisition system. A thin metal plate is inserted between the control card and the two CROC cards to isolate the noise from digital activity of the FPGA and ARCNet card from the noise sensitive CROC card components. One FEM accepts 128 channels of input from the chambers. Each FEM operates independently of the others, providing for good protection against large scale failure if one FEM should malfunction.

A local area network (ARCNet) is used to provide configuration information to the electronics. An ARCNet receiver/transmitter card provides an interface to the main PHENIX ARCNet server. Communication happens by passing a token around a ring of ARCNet nodes. A token is a packet of information sent out on the network. Each ARCNet node will examine the token packet. The node will decide whether to accept the packet, and then send the token on to the other nodes in the ring. Communication speeds approaching 2.5 Mbps can be realized. A maximum of 255 nodes make up the network. In the PHENIX MuTr, the nodes are configured in a daisy chain fashion. The FEE for the MuTr has many features that may be configured remotely. ARCNet provides a way to configure the electronics by passing configuration information to the FEMs over

Table 2.1: Functions performed by ARCNet in the MuTr electronics.

ARCNet functionality in the muon tracking electronics
- Configure the CPA chips
- Configure the AMU/ADC Chips
- Configure the FPGA serial configuration string
- Provide an external reset to the FPGA
- Download the FPGA EEPROM
- Communicate with the Dallas monitor chips
- Configure the calibration card pulse DAC and drivers
- Monitor the Glink/Clink card 5V and 3.3V regulators
- Provide a reset signal to the glink cards

the ARCNet network. Each FEM has an ARCNet daughter card that can accept the network tokens, and perform the appropriate actions.

ARCNet is responsible for many functions pertaining to the MuTr electronics. These functions are summarized in Table 2.1. Configuration of the CPA chips involves setting the correct output voltage levels and the baseline level restore value to shape the pulse as needed. The AMU/ADC chips must be set to the proper reference voltage and ramp rate. The FPGA serial string provides information to the FPGA like the FEM ARCNet node ID, and can put the FPGA into

various test modes. The Dallas monitor chips (named because they are manufactured by Dallas Semiconductor) provide information about the supply voltages, temperatures, and current draw of the FEM and Glink/Clink cards. The FPGA EEPROM can be downloaded via ARCNet, allowing for complete remote control of the FEM functionality. The calibration system also uses ARCNet to control the size of injected pulses and the channels to be pulsed.

The ARCNet interface card used by PHENIX is quite versatile, because it has an 8051 style microcontroller on it. The 8051 I/O ports are used to set up serial data clocking schemes, serial communication with the Dallas chips, and even an embedded JTAG (Joint Test and Action Group) port for downloading the FPGA EEPROM. Control of the 8051 I/O ports is achieved with C programs, compiled with an 8051 C-compiler, and downloaded in HEX format to the ARCNet boards.

Clock and trigger information travels from a PHENIX timing module over many meters of fiber optic line and is fed through two stages of fanout modules. The single clock/trigger signal is fanned out into 168 separate signals, providing one input for each FEM. The fiber optic signal is converted by a fiber optic to copper signal translator card (Glink/Clink card) to a standard copper line signal outside the magnet volume. Copper cables carry the signal through small openings in the magnet steel to the FEE inside. Digitized data travels from the FEMs over copper cable and is translated into fiber optic signals, which continue on to the main PHENIX data aquistion system.

Calibration of the system is essential for the data analysis. For this purpose a pulse generating module is used to inject pulses onto a subset of the anode wires for each wire chamber. This induces an observable signal on the cathode strips. The system can be configured to fire any subset of cathode planes with any desired pulse amplitude. By observing the response on the cathode strips for various injected pulse amplitudes, the gain of each strip can be determined. The calibration system also determines the pedestal voltage levels and electronic noise levels for every strip.

2.4 Muon Identifier Panels

The MuId is designed for a π/μ rejection factor of $2.5\text{x}10^{-4}$. Approximately 10^{-2} of the rejection factor comes from the absorbing material which preceeds the MuId, namely the central magnet steel, the nosecone, and the thick steel plate which forms the backs of the muon magnets. The remainder of the rejection power comes from 60 cm of steel in the MuId itself. This steel thickness is segmented into 4 plates of thickness 10 cm, 10 cm, 20 cm, and 20 cm. The panels closer to the interaction point are thinner to increase the ability to detect the ϕ meson and also to improve tracking within the identifier.

The MuId uses Iarocci tubes assembled into panels which are interleaved with the steel. These are basically proportional counters constructed from a group of 100 μm gold plated Cu-Be wires inside of graphite coated tubes. The tubes are

operated at 4.5 kV with a gas mixture of CO_2 and isobutane in the approximate ratio 80%:20%. Half of the tubes are oriented horizontally, and the other half are oriented vertically. The tubes are assembled into panels, and there are six panels for each of the five gaps between the steel. The panels are arranged around the hole which houses the beam pipe.

2.5 Muon Identifier Electronics

The MuId electronics digitize the signals from the Iarocci tubes and provide level 1 (LVL1) trigger information to the PHENIX data aquisition system. A muon identifier readout channel consists of the anode output of two tubes which have been staggered by half a channel and whose outputs have been OR'd together. This is done to decrease the response time in order to ensure the signals can be processed before the next beam crossing every 106 ns. For maximal noise suppression, signal amplification is performed in the panels and the amplified signal is carried over 30 m cables to crate based processing electronics. Each electronics crate contains two types of cards, a read out card (ROC) and an FEM. A typical input charge to the electronics is about 100 pC, which is transformed to a signal of $\sim$250 mV.

The ROC cards perform the analog signal processing, event synchronization, data buffering, and serial control. Data from each ROC is sent to the PHENIX LVL1 trigger and an algorithm determines if there are muon track candidates.

Table 2.2: Functions performed by ARCNet in the MuId electronics.

ARCNet functionality in the muon identifier electronics
- Set/readback threshold DACs
- Set/readback programmable delays
- Set/readback selected delays
- Set/readback pulser selects, MUX selects, output mask selects
- Download FPGA programs

Buffering of data from each beam crossing is accomplished with three 32 bit 64 deep FIFOs. If the event satisfies the LVL1 trigger the data is moved to an FPGA based 112 bit 5 deep FIFO which can transmit the data to the PHENIX data aquisition system. This buffer can store up to 5 events.

A MuId FEM is essentially a crate controller. It interfaces to the PHENIX data aquisition system and controls the ARCNet functionality. The responsibilities of the ARCNet serial interface are summarized in Table 2.2. These responsibilities are control of the signal threshold DACs, control of programmable delays for signal synchronization, control of an on board diagnostic pulser and spy multiplexer (MUX), and downloading of FPGA code.

2.6 Muon Identifier Trigger

Each MuId ROC sends data to the PHENIX LVL1 trigger. An algorithm searches for muon track candidates. The algorithm searches for patterns in the hit tubes that are consistent with tracks. The algorithm is steerable, meaning that the search window in which hit tubes for a given track are expected to exist depends on the vector projection of hits in the previous two gaps. Skipped gaps are permitted in the algorithm. The muon trigger identifies shallow and deep roads, and a dimuon trigger can consist of any combination of shallow and/or deep roads.

2.7 Ancillary Systems

Gas supply for the MuId tubes and the MuTr chambers is mixed by a series of flow meters and regulators in the PHENIX gas mixing house. The gas is recirculated for environmental and economical reasons. An oxygen analyzer is used in the muon tracking system to measure contamination which may occur from air diffusing into the system. Protection against over-pressure is critical considering the thinness of the station 2 chamber mylar windows.

The MuTr chambers utilize an optical alignment system, depicted in Figure 2.12, to monitor the relative positions of the chambers during the data taking period. These corrections can then be applied offline in the track finding software. The system uses a light source to transmit light over fiber optic lines to station

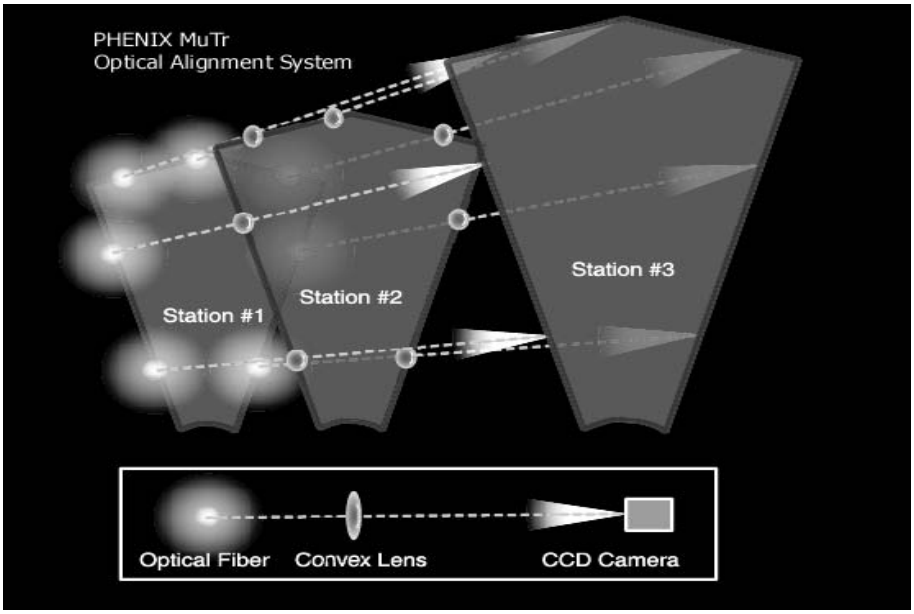

Figure 2.12: Optical alignment system for the PHENIX muon tracker.

1. The light beam is transmitted from station 1 through a lens at station 2 onto a CCD camera at station 3. The position of the light spot in the camera is monitored, and the relative chamber positions can be calculated. Each octant has 7 light paths.

The MuTr electronics make use of ARCNet to monitor the temperatures, voltages, and current inside the FEMs and on the Glink/Clink boards. A battery monitor chip from Dallas Semiconductor is used. Each FEM has 7 of these chips which are controlled by the serial port on the ARCNet card's embedded 8051 processor. The analog and digital supply voltages, current usage, and the temperature on the boards are digitized by the chip with good accuracy. It is desired

to operate the electronics at temperatures below 40° C.

Both the MuId and the MuTr circulate dry air in the volumes containing the readout electronics. The MuTr circulates cooling water to the FEMs which travels through cold plates in contact with the boards to reduce the temperature during operation.

3 DETECTOR SIMULATIONS

Particle physics experiments rely heavily on simulations to understand detector performance and acceptances for various physics processes. Simulations relevant to the design and performance expectations of the PHENIX muon spectrometer have been performed in [PHE 98]. A variety of event generators have been used. For charm production, PYTHIA is generally used for proton collisions, and HIJING (based on PYTHIA) is generally used for heavy ion collisions. For Drell-Yan production, the CERN PDFLIB structure function library is used. HIJET and the CERN UA1 event generator are used for generation of heavy ion minimum bias background events.

The simulation of the detector volume is handled by PISA. PISA tracks particles through the PHENIX detector and stores all the hits which occured in active detector volumes. Figure 3.1 shows the PISA geometry used for the PHENIX muon arms simulations.

3.1 Muon Tracking Performance

The geometry of the detector used in the simulation is the same as the actual physical construction described in Chapter 2. The chambers are modeled with 1 cm wide cathode strips, anode wires separated by 1 cm, and a 1% noise level, which reproduces the 100 μm spatial resolution. The central magnet steel, copper

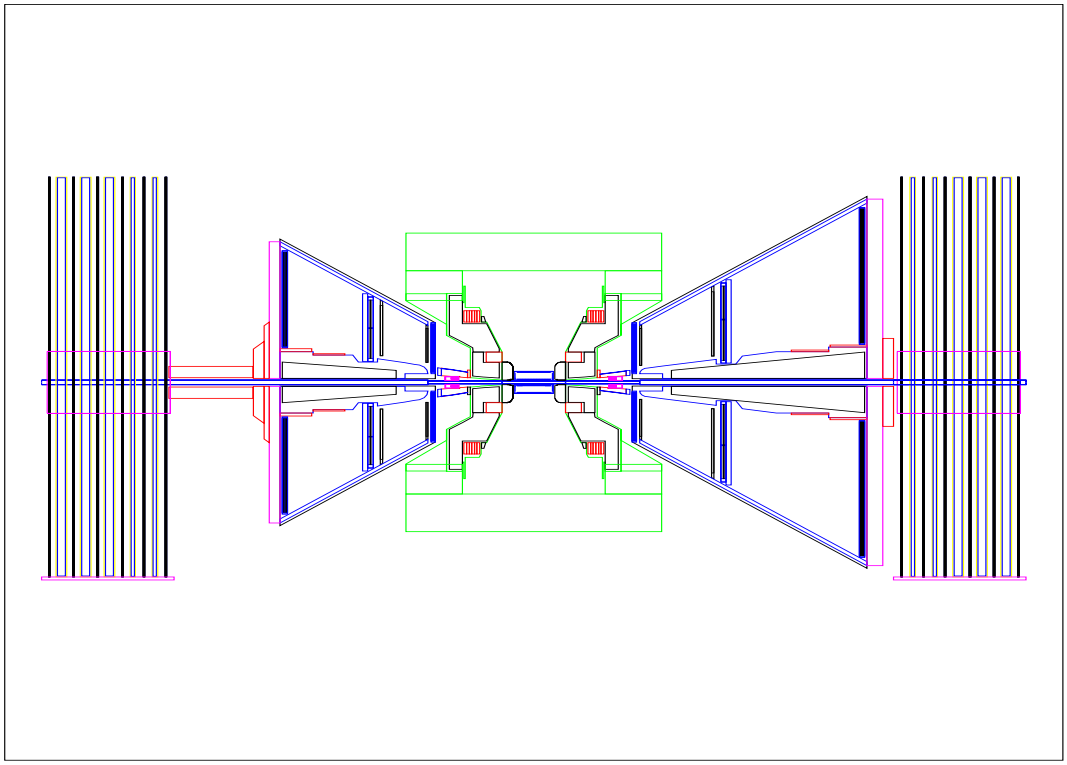

Figure 3.1: PISA geometry for the PHENIX muon arms simulations.

nosecone and insert, and iron plug absorbers are also included in the simulation. The response of the cathode strip chambers is based on work by Mathieson [Mat 88]. The Mathieson function is used to determine the amount of charge deposited on the cathode strips. Muon track reconstruction was based on the GEANE package [Inn 91] and a Kalman filter [Inn 93].

The momentum spectrum of muons ranges from 2 GeV, which is the minimum momentum required to reach the muon identifier, to greater than 50 GeV for muons from weak decays. The momentum resolution of the muon tracking

Table 3.1: Integrated magnetic field values ($\int$B·dl) in units of Gm used in the momentum resolution studies (taken from [PHE 98]).

	15^o	20^o	25^o	30^o
North arm	7311.33	4921.06	3594.15	2775.69
South arm	7737.99	4937.44	3442.67	2549.40

chambers has been studied at momenta of 2, 3, 5, 7, 10, 30, and 100 GeV. Four polar angles have been used to describe the magnetic field strength. Table 3.1 shows the integrated magnetic field in units of Gm at the four chosen angles. Figure 3.2 shows the obtained momentum resolution (momentum uncertainty divided by the momentum) for the muon arms, and the ratio of the resolutions in south and north. At large momentum the north arm performs better simply because it is longer in the z direction.

The Υ decay has been chosen to study the dependence of the mass resolution on chamber resolution. This is because decay muons from J/ψ and ϕ decays are at low enough momenta that their resolution is determined by scattering in the absorber material, rather than the chamber resolution. The decay muons from Υ, however, occur at high enough momenta that the chamber resolution is important for the mass resolution. Figure 3.3 shows the relationship between the Υ mass resolution and the chamber resolution from the simulation. To separate Υ(1S) from Υ(2S+3S) requires a mass resolution of $\sim$200 MeV, which can be

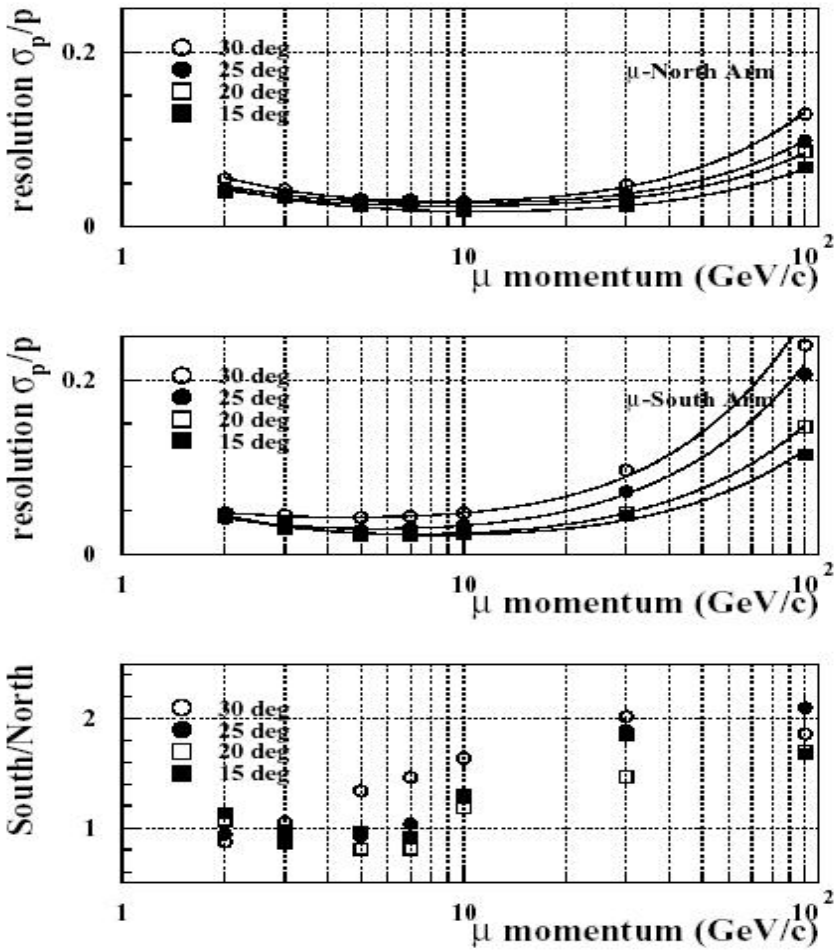

Figure 3.2: Simulated momentum resolution of the muon arms (taken from [PHE 98]).

achieved with 100 μm resolution in the chambers. The south arm, being shorter in the z direction, has somewhat worse performance, giving a mass resolution of $\sim$260 MeV for a 100 μm chamber resolution. The mass resolution depends more heavily on the resolution of the station 2 chambers because they are responsible for measuring the track sagitta. Thus, the Υ mass resolution for the south arm

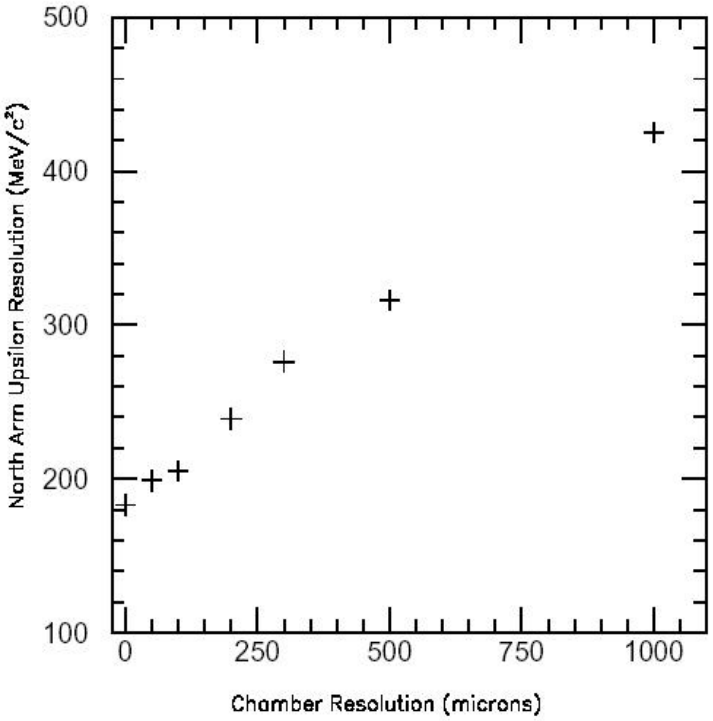

Figure 3.3: Simulated Υ mass resolution as a function of chamber resolution (taken from [PHE 98]).

can be improved by requiring a better resolution at station 2.

Figure 3.4 shows the simulated mass resolutions for the ϕ and J/ψ . The mass resolution for ϕ is 87 MeV for the north arm and 55 MeV for the south arm. The mass resolution for J/ψ is 117 MeV for the north arm and 94 MeV for the south arm. Because the resolution for ϕ and J/ψ is dominated by scattering in the absorber material, the south arm performs better because it has a shorter nosecone.

The radial dependence of the chamber occupancy is such that it decreases as

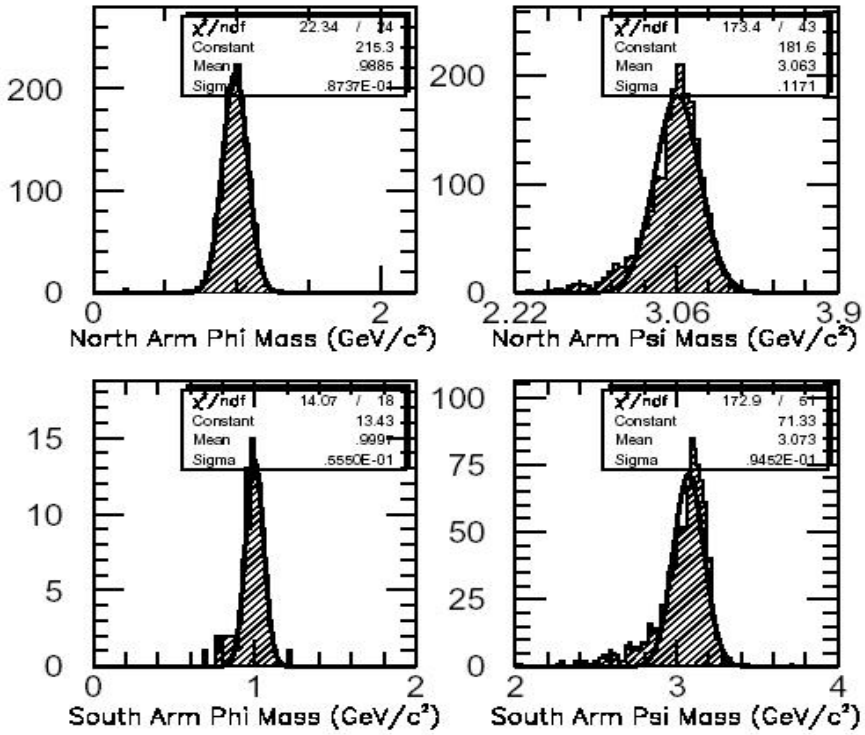

Figure 3.4: Simulated ϕ and J/ψ mass resolutions as a function of chamber resolution (taken from [PHE 98]).

the distance away from the magnet piston increases. Track finding in regions of low occupancy is expected to be straightforward, but at large occupancies may suffer from ghost tracks and cathode cluster overlapping. Ghost tracks are tracks which share many of the same chamber hits but have been identified as separate tracks by the track finding algorithm. Cluster overlapping can occur if there are two hits in a chamber very close to each other such that the charge distributions interfere with each other. This can make fitting of the clusters difficult. Table 3.2 shows the track finding efficiency in the north arm from Υ decays embedded

Table 3.2: Track finding efficiencies for different chamber occupancies in the north arm for Υ decays (taken from [PHE 98]).

Occupancy in Chambers (%)	Track Finding Efficiency (%)
0-3	100
3-5	96
5-7	97
7-9	92
9-12	85

in a HIJING background event for different chamber hit occupancies. Table 3.3 shows the track finding efficiency for different track multiplicities. The efficiency is defined as the number of reconstructed tracks divided by the number of tracks in the active detector volume which passed through all three tracking stations.

3.2 Muon Identifier Performance

For central events using the UA1 simulation, the mean occupancy at gap 3 is only 1 hit per event. Events from beam gas (a particle from the accelerated beam striking a random gas particle inside the beam pipe) are expected to be a more significant source of background. Absorbing material is required around the beam pipe in the region of the muon identifier to reduce the beam gas background. For 80% of J/ψ mesons, both muons reach at least the third MuId plane, of which

Table 3.3: Track finding efficiencies for different track multiplicities in the north arm for Υ decays (taken from [PHE 98]).

Track Multiplicity (%)	Track Finding Efficiency (%)
0-5	100
5-10	97
10-15	95
15-20	96
20-25	87

97.4% will satisfy the LVL1 trigger. For ϕ mesons, 18% will reach the third MuId plane, of which 80% will satisfy the LVL1 trigger. The LVL1 trigger efficiency is flat over the rapidity range of the muon identifier.

To realize a π/μ separation of $\sim 10^{-4}$ requires that the MuId road must match to a track in the MuTr, the track in the MuTr must extrapolate to within 40 cm of the vertex, the MuId road must have a correct penetration depth/momentum relation, and the invariant mass of the dimuon pair must be > 1 GeV.

3.3 Detector Acceptances

The acceptance of the PHENIX muon spectrometer arms for dimuons from decays of ϕ, J/ψ , ψ', Υ, and Drell-Yan has been studied. Figure 3.5 shows the acceptance in p_t and rapidity for the vector mesons decaying to dimuons in the

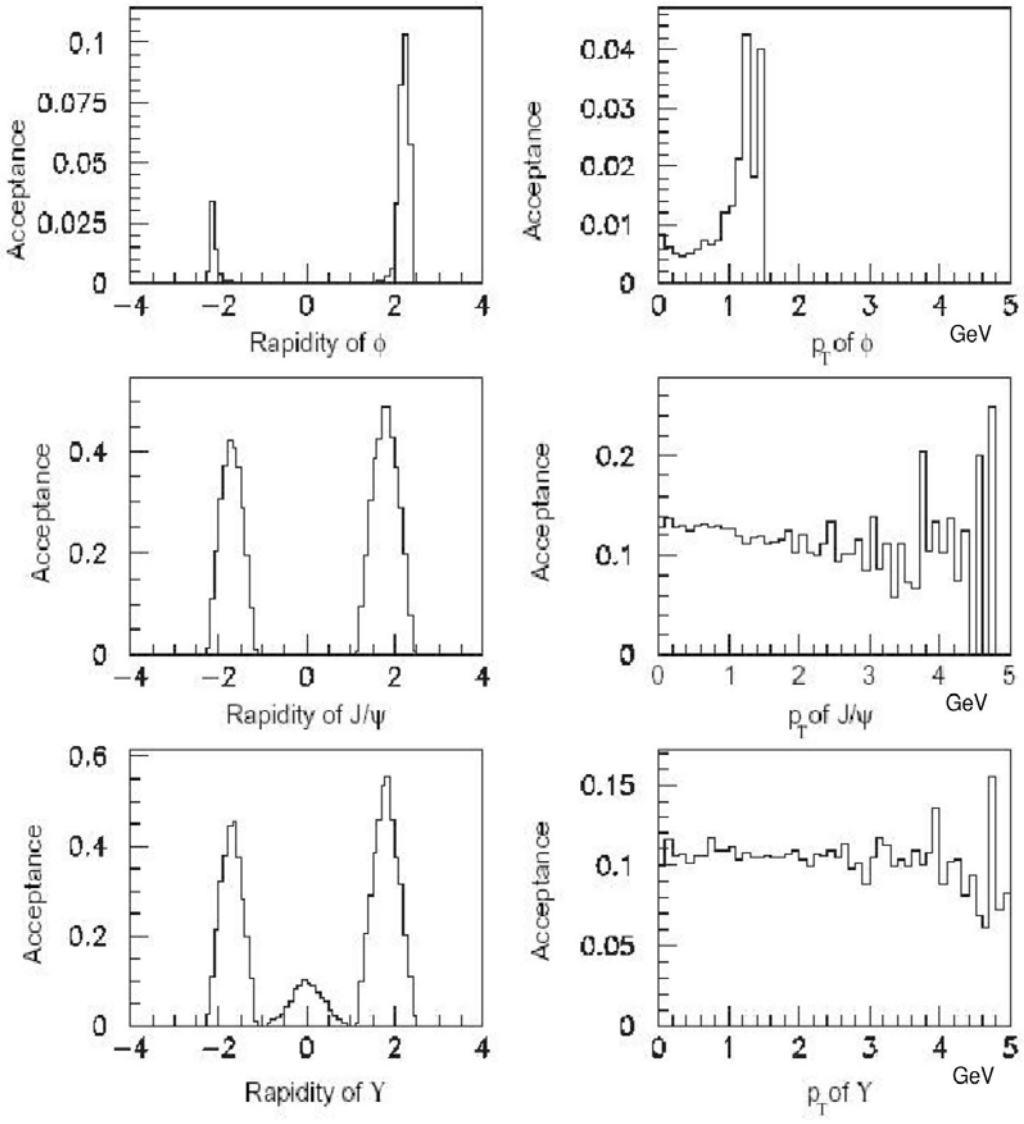

Figure 3.5: Simulated acceptances for vector mesons decaying to dimuons in the PHENIX muon spectrometer arms (taken from [PHE 98]).

muon spectrometer arms. The piston of the south magnet is slightly larger than the north magnet, which produces a reduced acceptance for tracks at small polar angles when compared to the north arm. This effect is particularly pronounced

for the ϕ meson, which produces decay muons at small angles due to its small mass. Υ decays which produce one muon in each arm allow for some acceptance in the mid-rapidity range. The acceptances in pair mass, p_t, rapidity, and $x_{_F}$ for Drell-Yan events is shown in Figure 3.6.

Another important aspect of the detector acceptance is a calculation of the expected event rates. Table 3.4 shows the expected number of events in the north arm, south arm, and one muon in each arm, for one RHIC year of Au ion running. A RHIC year for Au running is taken to be 2000 hours at a luminosity of $2.2\text{x}10^{27}\text{cm}^{-2}\text{s}^{-1}$. The expected yields for proton collisons are estimated by using a proton beam luminosity of $1.1\text{x}10^{31}\text{cm}^{-2}\text{s}^{-1}$ and scaling the Au numbers by $\frac{1.1\text{x}10^{31}}{2.2\text{x}10^{27}}\frac{1}{197^2}$. The resulting yield expectations for one RHIC year of proton running are shown in Table 3.5.

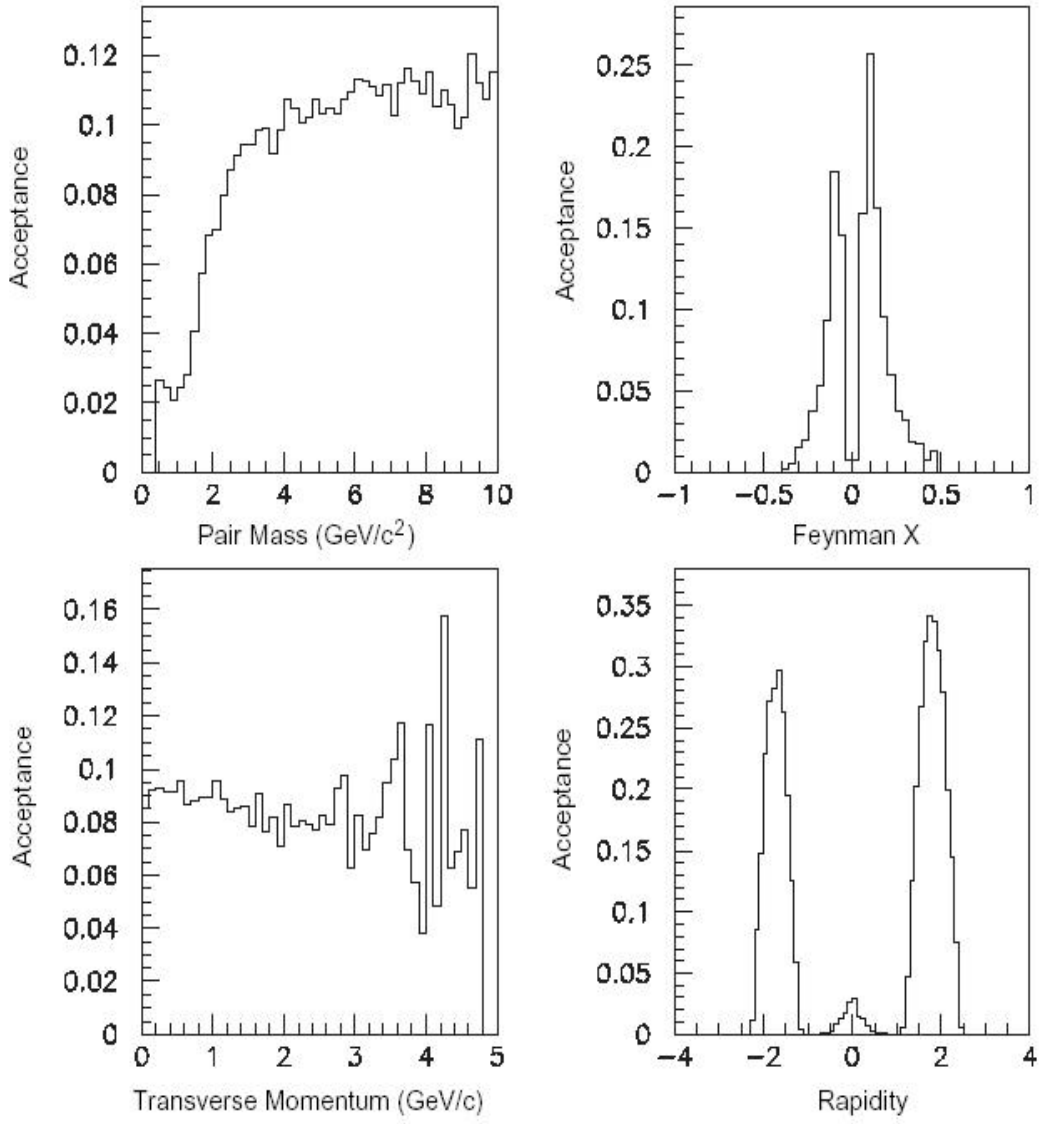

Figure 3.6: Simulated acceptances for Drell-Yan events producing dimuons in the PHENIX muon spectrometer arms (taken from [PHE 98]).

Table 3.4: Expected event rates for one RHIC year of Au ion running (taken from [PHE 98]).

Signal	North arm	South arm	One in each arm
ϕ	500 k	69.8 k	0
J/ψ	1.73 M	1.34 M	0
ψ'	24.2 k	18.7 k	0
Υ	4.92 k	4.10 k	4.06k
Drell-Yan (1.5-2.5 GeV)	216 k	147 k	0
Drell-Yan (2.5-3.5 GeV)	67 k	56 k	0
Drell-Yan (3.5-4.5 GeV)	30 k	27 k	842
Drell-Yan (4.5-5.5 GeV)	13 k	10 k	2.7 k
Drell-Yan (5.5-6.5 GeV)	6.6 k	5.5 k	3.5 k
Drell-Yan (6.5-7.5 GeV)	3.5 k	2.9 k	2.5 k
Drell-Yan (7.5-8.5 GeV)	1.8 k	1.6 k	1.6 k

Table 3.5: Expected event rates for one RHIC year of pp ion running (taken from [PHE 98]).

Signal	North arm	South arm	One in each arm
ϕ	64.5 k	9 k	0
J/ψ	223 k	172 k	0
ψ'	3.12 k	2.4 k	0
Υ	634	529	524
Drell-Yan (1.5-2.5 GeV)	28 k	19 k	0
Drell-Yan (2.5-3.5 GeV)	8.6 k	7.2 k	0
Drell-Yan (3.5-4.5 GeV)	3.9 k	3.5 k	109
Drell-Yan (4.5-5.5 GeV)	1.7 k	1.3 k	348
Drell-Yan (5.5-6.5 GeV)	850	710	450
Drell-Yan (6.5-7.5 GeV)	450	370	320
Drell-Yan (7.5-8.5 GeV)	230	206	206

4 DETECTOR PERFORMANCE FOR RUN 2

The south muon arm was completed in 2001. The first data was collected during the second RHIC running period in 2001-2002. In run 2 PHENIX collected data from Au ion collisions with a total integrated luminosity of $\sim$24 μb^{-1}, and from proton collisions with a total integrated luminosity of $\sim$150 nb^{-1}. Because this was the first data collected by the south muon arm, a study of its performance is both interesting and necessary before physics analysis can proceed. An overview of the performance of the south muon arm during RHIC run 2 will now be presented.

4.1 Muon Tracker Cathode Strip Chamber Performance

Prior to installation of the tracking chambers in the PHENIX collision hall, a test was performed with one station 2 octant and its corresponding readout electronics. Two scintillators were used to provide a cosmic ray trigger. Tracks through the chamber were identified, and the resolution was computed. The hits in five of the six cathode planes were fit with a straight track and the track was projected to the sixth plane. Only tracks approximately perpendicular to the face of the chamber were used. A residual was then computed as the distance between the intersection of the projected track with the sixth plane and the hit on the sixth plane. Figure 4.1 shows the residual distribution. The composite chamber

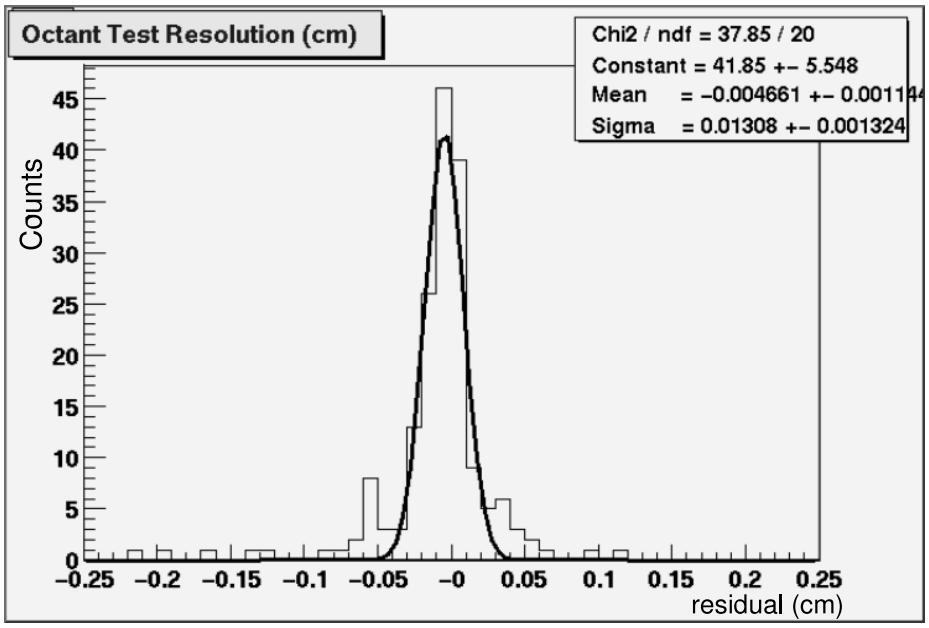

Figure 4.1: Resolution for a station 2 chamber from cosmic rays.

plus projection error is ∼131 μm, consistent with the design goal of 100 μm for the chamber and readout alone.

After this successful performance test of the station 2 chamber, all the chambers which comprise the south muon arm were installed in the PHENIX interaction hall. The chambers did not suffer any broken wires. The most serious problem encountered was the inability to hold some fraction of the channels at the operating voltage. This was apparently caused by a combination of two factors: failure of capacitors on the anode plane circuit boards, and a sensitivity to ambient humidity due to insufficient conformal coating on the circuit boards. This resulted in a loss of acceptance during the data taking period. Figure 4.2 shows the x and

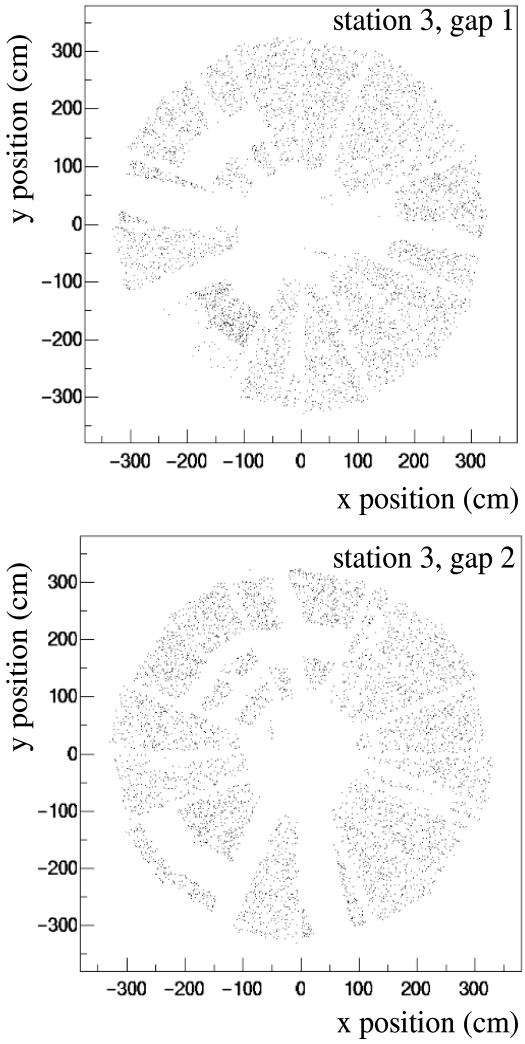

Figure 4.2: Position locations of clusters on the two station 3 cathode gaps.

y location of clusters on the two station 3 chamber gaps for a typical high voltage configuration. The circular region devoid of hits in the center is the location of the magnet piston. Areas of inactive high voltage appear as swaths devoid of

hits in the phi direction. Areas of inactive readout electronics typically appear as swaths in the radial direction. The high voltage channels which were disabled varied from run to run. A comprehensive log of the high voltage state was kept during the run. It is possible to lose one cathode plane in a station and still be able to reconstruct a track passing through that area using the remaining planes. Acceptance losses occur in areas with two or more planes which have overlapping inactive regions. The estimated acceptance loss for dimuons due solely to inactive high voltage regions for run 2 was approximately 15%.

Before tracks can be assigned an accurate momentum, an alignment of the tracking stations must be performed. The alignment for the south muon arm has been studied [Cho 02]. There are several different alignment parameters which must be determined. First, the relative alignment of the cathode planes within a chamber must be understood. The alignment studies are done using data taken without a magnetic field to produce straight tracks. The relative alignments between cathode planes can by studied by computing the spatial positions of the hits within a chamber and seeing how well they conform to a straight line fit. For each plane, a hit position is determined and subtracted from the hit positon in a different plane. A correction for the angle of incidence of the tracks is included. Using many tracks, a distribution of the relative offsets for all the planes is determined. If the offset of the centroid in the distribution is greater than 100 μm a correction is applied to the relative alignment of the cathode

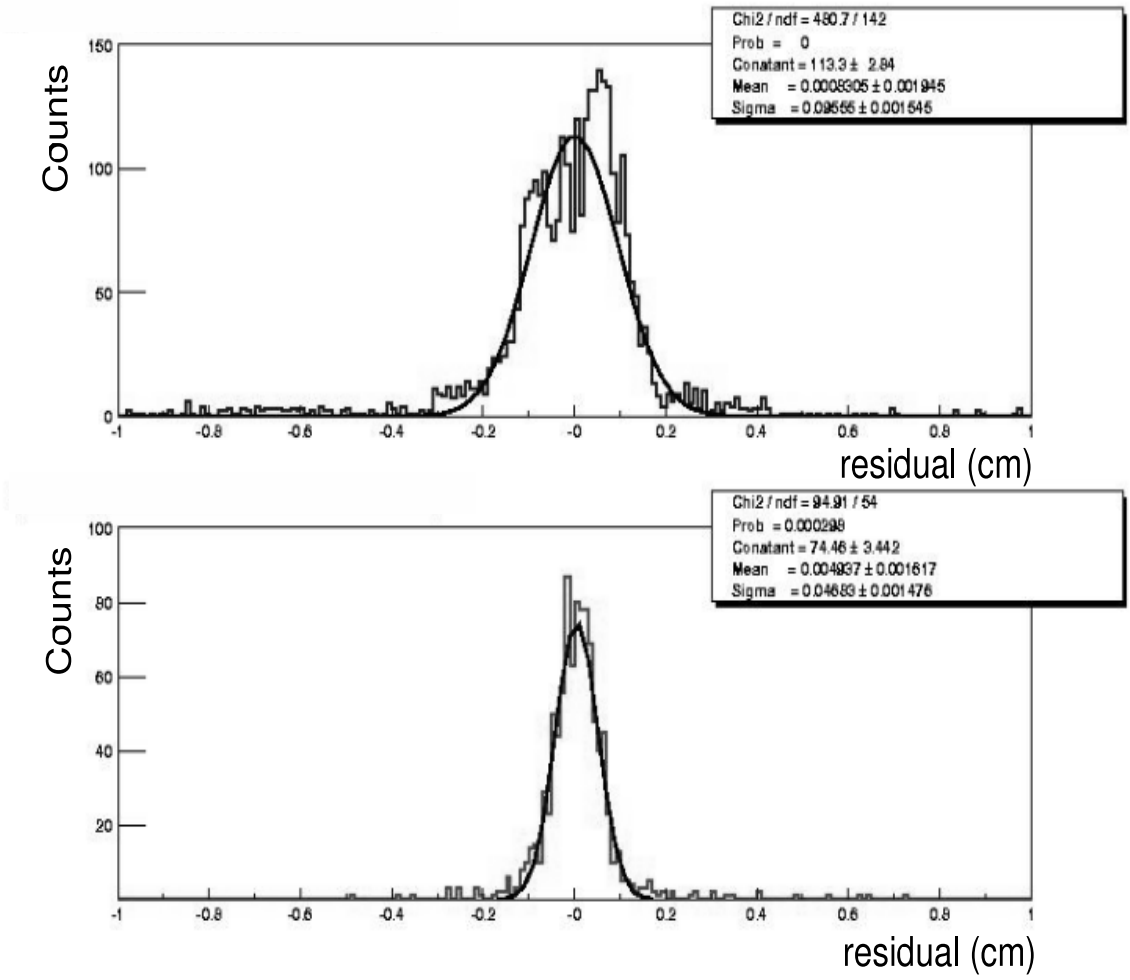

Figure 4.3: Improvement in the alignment of two station 3 cathode planes after corrections are applied. The units are centimeters.

planes. Figure 4.3 shows the improvement in the alignment of two of the station 3 planes when corrections are applied. After alignment correction, the centroid of the distribution is centered on zero, and the resolution determined by the gaussian fit has improved. Combining the resolutions for each of the six cathode planes in a chamber, the overall chamber resolution can be calculated. The current

resolution for the tracking chambers is $\sim$150 μm. These numbers may improve with more study of the function used to fit the charge distribution across strips. The resolution can also benefit from reduced noise levels in the readout electronics.

In addition to alignment of the cathode planes within a chamber, the relative alignment between stations is also studied. A straight line fit is performed between the station 1 hits and the station 3 hits for a given track. The deviation of the station 2 hits from this line is then determined. Figure 4.4 shows the deviation of the station 2 hits from the straight line fit. From simulation, it is known that the deflection due to multiple scattering scales with the momentum. The deflection in centimeters is expected to be approximately $0.19/p$. The width of the distribution in Figure 4.4 is about 1.3 mm, consistent with the expected deflection for tracks having a momentum $\sim$1 GeV. The centroid for the distribution of hits in each half octant was adjusted to better than 100 μm, much less than the deflections caused by multiple scattering. This means that the track resolution is dominated by multiple scattering and not by the relative alignment of the cathode planes.

It is interesting to study the occupancy of individual strips in the cathode chambers. Figure 4.5 shows the hit average (fraction of events for which the strip is hit) for each of the six cathode planes in a half octant of station 1 for several runs of Au data. Recall that the cathode strips in different planes are oriented at different angles. Thus, some of the half octant planes have their shortest strips at the edges, and others have their shortest strips towards the

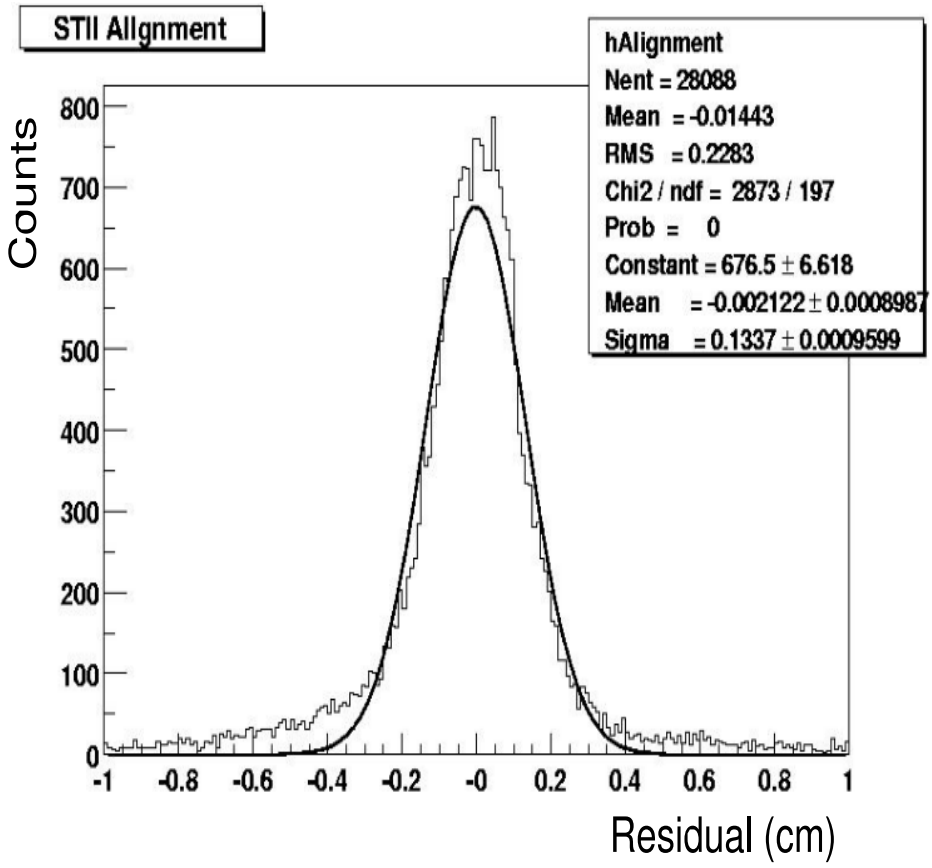

Figure 4.4: Deviation of station 2 hits from a straight line fitted to the station 1 and station 3 hits. The units are centimeters.

center. The occupancy of a strip is dependent on its length. The dependence of strip occupancy on length is apparent in Figure 4.5. The hit average ranges from near zero for the shortest strips, to about 0.18 for the longest strips. Because of the smaller number of particles produced in proton collisions, we should expect the hit average to decrease dramatically for the proton data. Figure 4.6 shows the hit average for the same six cathode planes for several runs of proton data.

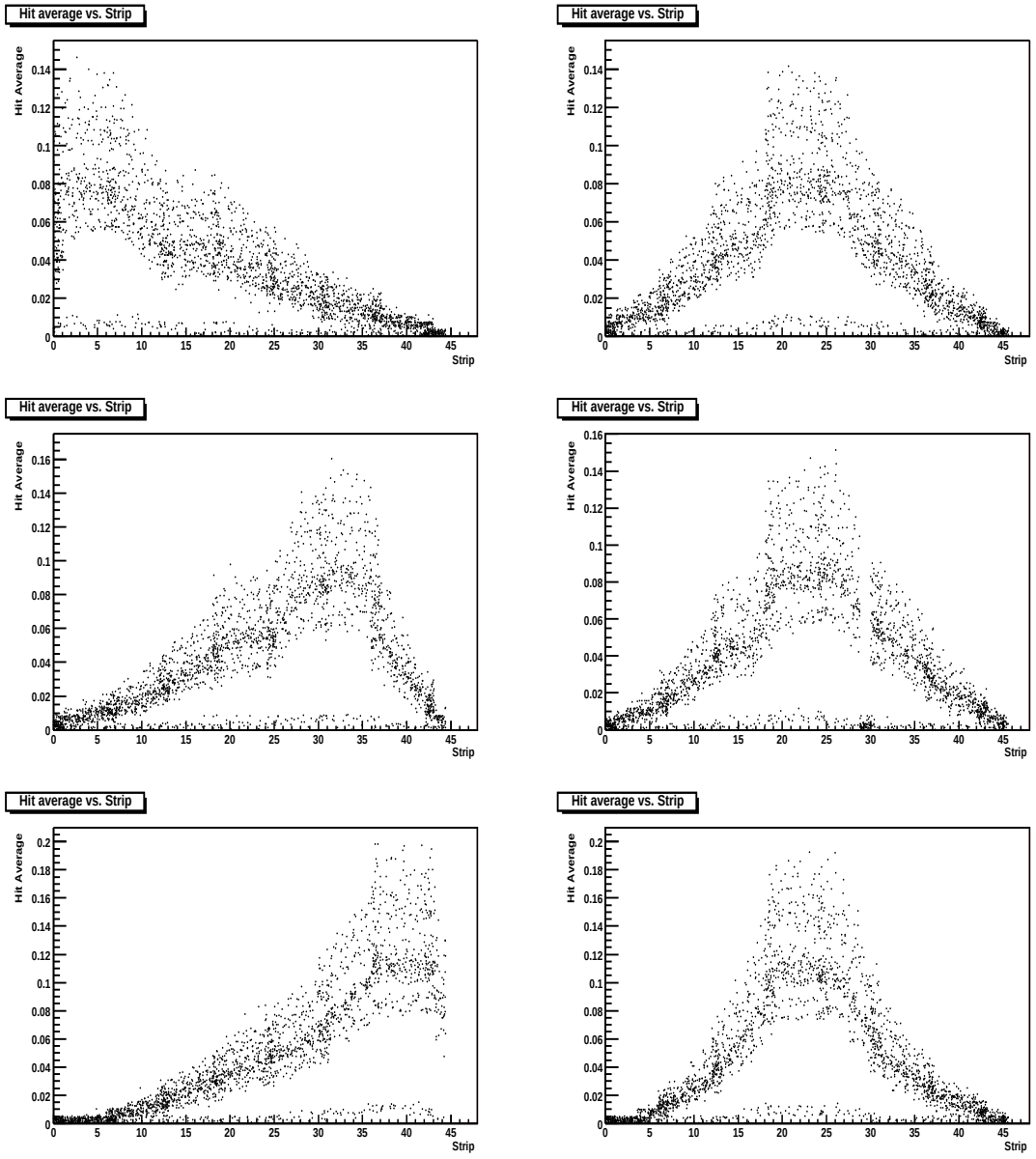

Figure 4.5: Hit average for strips on each of the six cathode planes for a half octant of station 1 (Au data).

In this case the hit average for the longest strips is about 0.0025.

Another interesting property to study is the overall strip occupancy in the chambers; that is, for a given event, how many cathode strips in a chamber are hit. A starting point for this calculation is the average number of fitted cathode clusters per event for each cathode plane of the detector. Figure 4.7 shows the average number of fitted cathode clusters per event for all cathode planes in stations 1, 2, and 3 for one run number of Au data. Station 1 has 48 planes (6 planes/octant times 8 octants), station 2 has 48 planes, and station 3 has 32 planes. Only events which have at least one cluster in each of the three tracking stations are considered. The large fluctuations from plane to plane are caused by disabled high voltage or areas of the chambers affected by disabled readout electronics. The cluster width is defined as the number of cathode strips over which the charge in a cluster is distributed. The average cluster width is about 2.5 strips for Au data. On a good cathode plane, the average number of fitted clusters per event is about 3.5 for stations 1 and 2, and about 2.5 for station 3. Thus, the number of hit strips in a cathode plane per event is 8.75 for stations 1 and 2, and 6.25 for station 3. Using that the number of strips in a cathode plane is 100 for station 1, 160 for station 2, and 220 for station 3, we can compute the chamber strip occupancy for Au collisions. The occupancies are 8.75% for station 1, 5.47% for station 2, and 2.84% for station 3.

Figure 4.8 shows the average number of fitted cathode clusters per event per

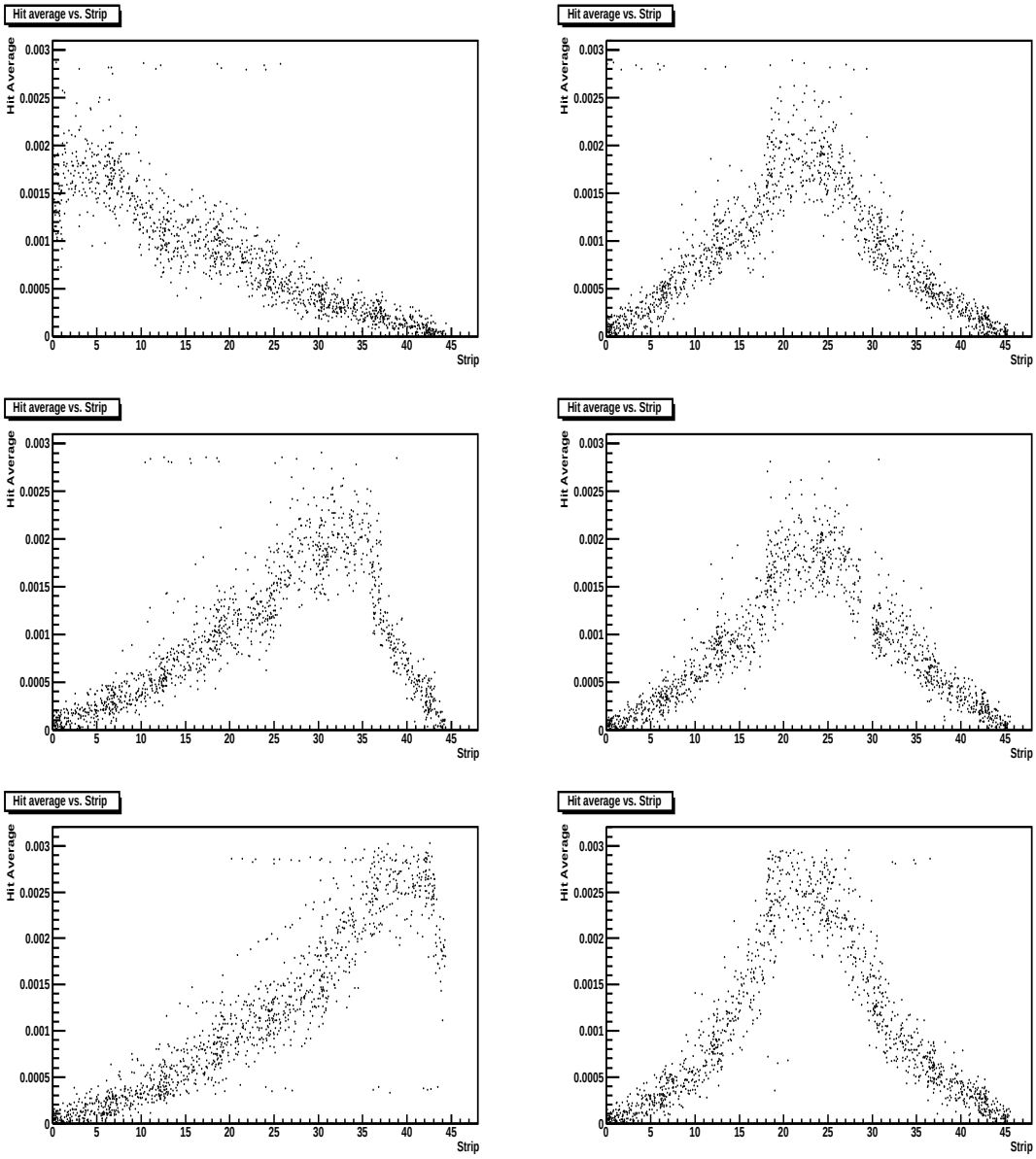

Figure 4.6: Hit average for strips on each of the six cathode planes for a half octant of station 1 (pp data).

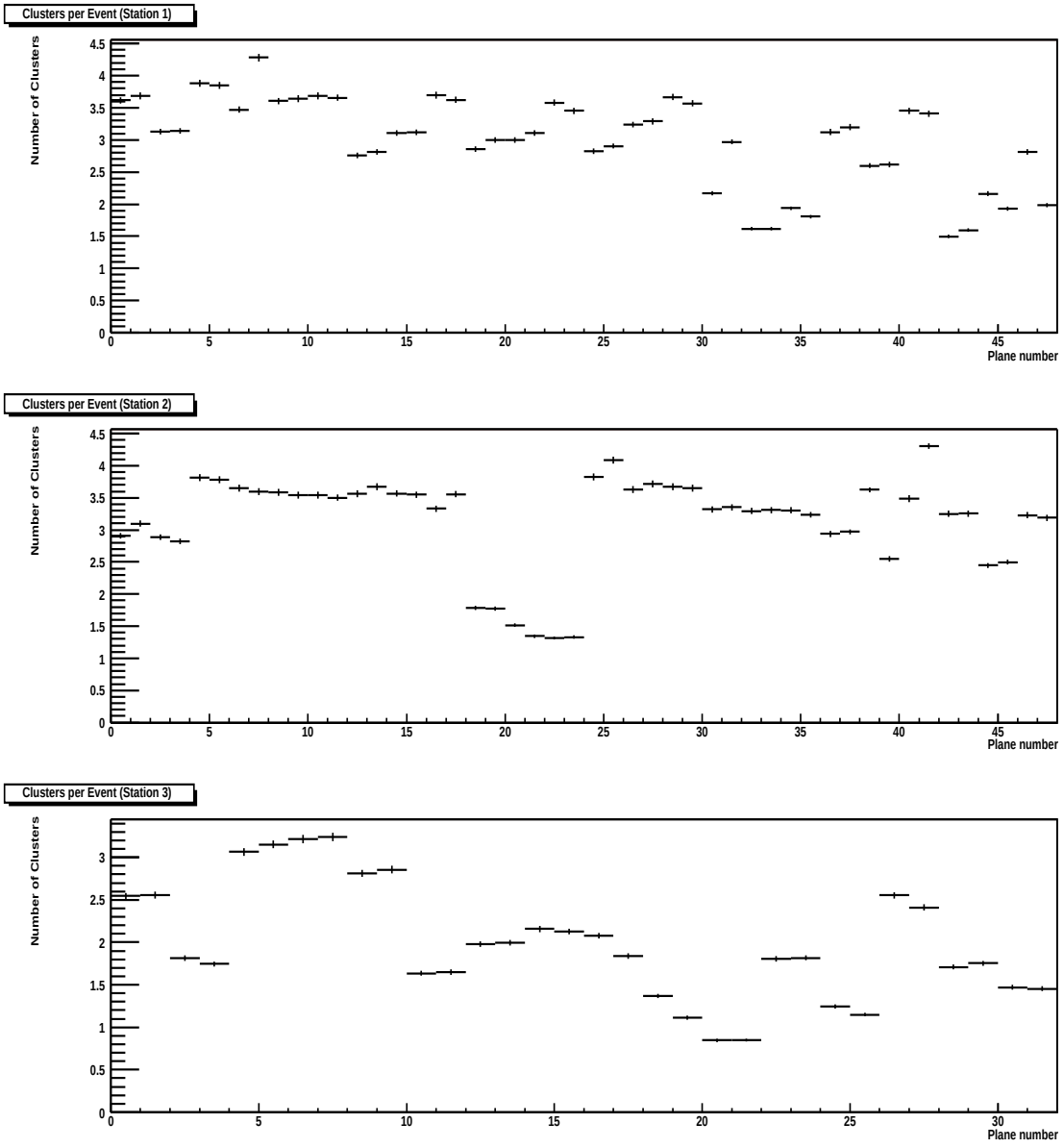

Figure 4.7: Average number of fitted cathode clusters per event for all the cathode planes (one run of Au data). Station 1 is at the top, station 2 in the middle, and station 3 at the bottom.

plane for one run number of proton data. Using an average number of fitted clusters per event of 0.25 for station 1, 0.25 for station 2, and 0.20 for station 3, and an average cluster width of 2.1 for proton data, the chamber strip occupancies are 0.53% for station 1, 0.33% for station 2, and 0.19% for station 3. These numbers are just a snapshot taken for one particular run number, and the occupancies are dependent on the beam luminosity and collision rate. However, we can make two observations: the chamber occupancy is significantly larger for Au data compared to proton data, and the occupancy of station 1 is larger than station 2 which is larger than station 3. Both of these observations are consistent with expectations.

There is also a clear correlation between the number of hits observed at station 1 and the total charge recorded by the beam-beam counter (BBC) detector. Figure 4.9 shows this trend. This is a clear indication that clusters in the tracking chambers are coming from collisions, and not beam gas events. If the events were beam gas, there would be many hits in peripheral events, which produce a small BBC total charge.

The optical alignment system (described in section 2.7) was able to detect movement of the chambers during the run. Radial motion is defined as movement in a direction transverse to the beam axis. Azimuthal motion is defined as movement which occurs in the plane oriented transversly to the beam axis (in the plane formed by the eight chambers in a station). Figure 4.10 shows a movement in the radial and azimuthal directions when the south magnet field was turned

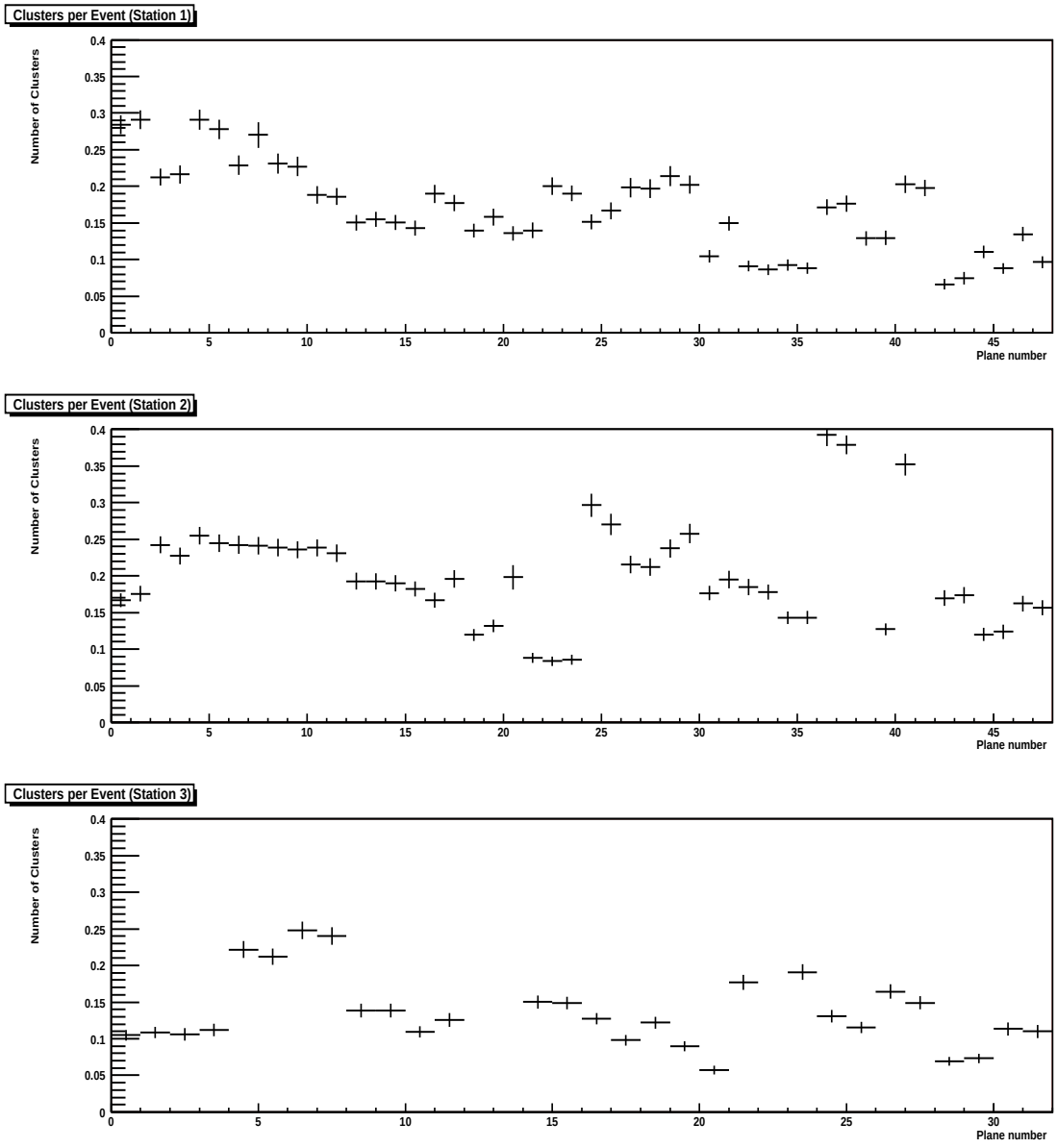

Figure 4.8: Average number of fitted cathode clusters per event for all the cathode planes (one run of pp data). Station 1 is at the top, station 2 in the middle, and station 3 at the bottom.

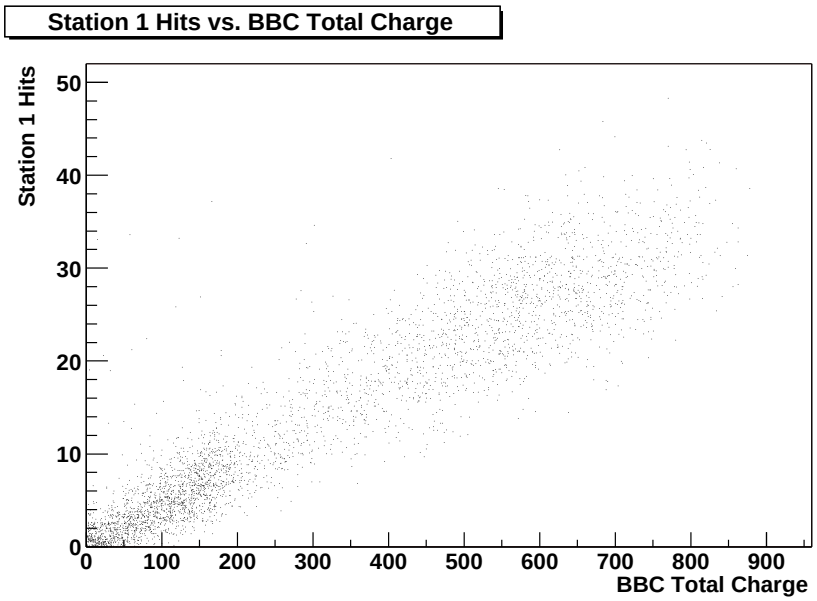

Figure 4.9: Number of hits on station 1 as a function of BBC total charge.

on. The deflection is about 40 μm. This data can be used to provide run by run corrections to the chamber alignment.

In summary, the performance of the muon tracking chambers during run 2 was consistent with expectations for this new detector. Some unexpected issues with humidity sensitivity and capacitor failure were identified and will be addressed before the next RHIC run. The chamber resolution is close to the design value and may improve further. The chamber occupancies for Au data are less than 10%, and for proton data are less than 1%. The instantaneous luminosity during the later stages of the Au running period were close to the design goal. The proton luminosity was about a factor of 10 below its design goal. The average

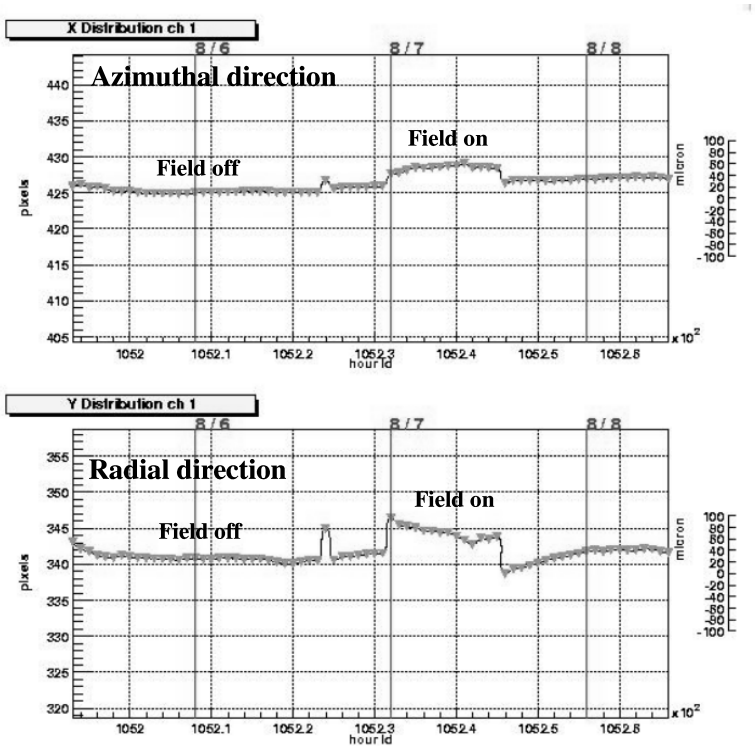

Figure 4.10: Movement of cathode chambers in the azimuthal direction (top), and radial direction (bottom) during activation of the magnetic field.

instantaneous luminosity per store for RHIC run 3 is expected to increase by a factor of 2 for Au running, and a factor of 10 for proton running. The chamber occupancies will increase accordingly.

4.2 Muon Tracker Electronics Performance

During design of the muon tracker electronics, a property of the preamplifier chip related to its baseline level restore (BLR) value was observed. The BLR value determines the shape of the digitized pulse. It was observed that the chip becomes

unstable if the BLR value is set too high, making accurate measurements of the pulse shape impossible. The maximum BLR value that one can use before this behavior becomes evident is approximately 29. Another observed characteristic of the CPA chip is that the time required for a CPA channel voltage to return to baseline after injection of a pulse can be quite long when the BLR is set to the maximum allowable value ($\sim$200 μs). The return to baseline is much faster ($\sim$ 10 μs) if the BLR value is set to 0. A fast return to baseline is desirable because it increases the rate at which successive pulses can be sampled. This suggests that BLR = 0 may be preferable to a higher BLR setting for data taking. Unfortunately, the pulse shape is quite different for BLR = 29 and BLR = 0, raising concerns that the best fitting algorithm may not be identical for both settings, and that possibly BLR = 0 pulses can not be fit with the same level of precision as is possible for higher BLR settings. The dynamic range over which we must accurately fit pulses extends from 0 V to approximately 3V, with a typical pulse being on the order of a few hundred millivolts. Figure 4.11 shows 64 time samples from a 3 volt pulse with BLR = 28 (just below the BLR = 29 limit), where the pulse is plotted as being positive instead of the negative going shape in Figure 2.11. The horizontal axis is time (in units of 0.1 μs, so the total time shown is 6.3 μs), the vertical axis is ADC counts. There is a quick rise to the peak followed by a gradual decay back toward the baseline. Figure 4.12 shows a 3 volt pulse with BLR = 0. Notice that the pulse shape is quite different, with

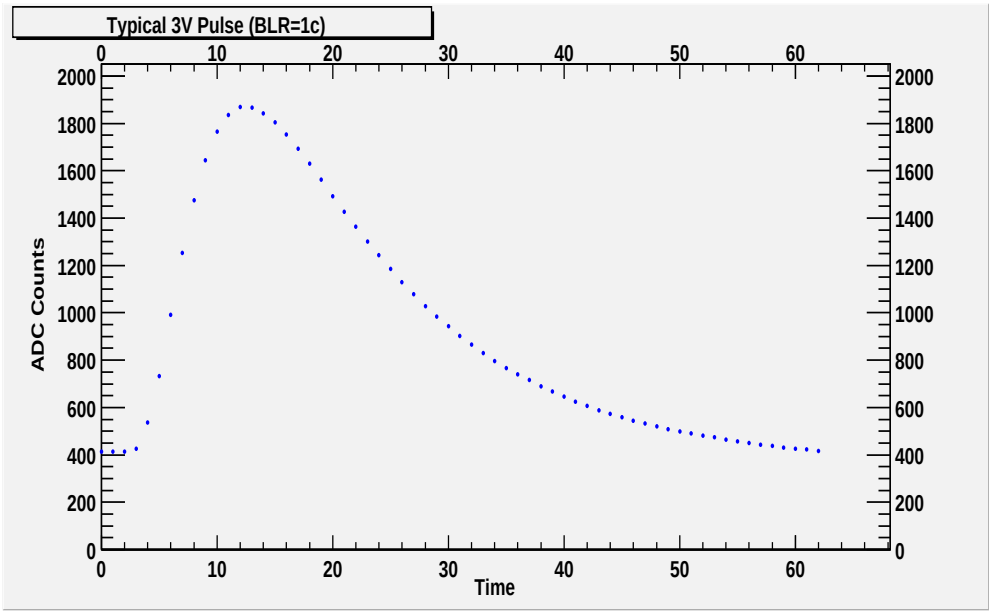

Figure 4.11: A 3 volt pulse with BLR = 28. The time is given in units of 0.1μs.

a much faster drop after the peak. The data actually goes beyond the dynamic range of the CPA chip (represented by an ADC count of zero) before returning to the baseline. The readout electronics will collect four samples from the 64 samples shown in the pulse data of Figs. 4.11 and 4.12. These four samples will then be fitted with an appropriate function to derive the amplitude of the pulse and the time at which the pulse began. The spacing of the three samples was chosen to have one sample on the rising edge of the pulse and three samples straddling the peak. Placing one sample on the rising edge of the pulse allows for determination of the start time when the pulse samples are fitted with a functional form. This can potentially be used to reject out of time pulses or pulses suffering from charge

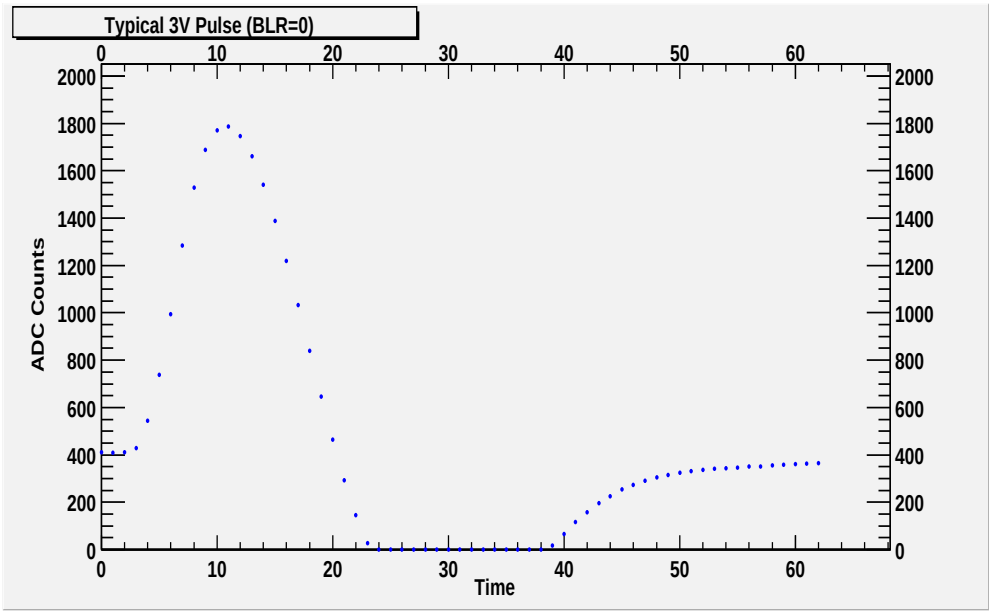

Figure 4.12: A 3 volt pulse with BLR = 0. The time is given in units of 0.1μs.

pileup from successive events. Pulse fitting for BLR = 29 pulses has previously used the function shown in Equation 4.1 to fit the 4 data samples,

$$f(t, p_0, p_1, p_2, p_3) = p_0[1 - e^{\frac{-(t-p_1)}{p_2}}]e^{\frac{-(t-p_1)}{p_3}} + \text{pedestal} \tag{4.1}$$

where t is time, the p_n are free parameters, and the pedestal is the nominal pedestal voltage level of that particular CPA chip channel (computed with a calibration system, not a free parameter). This fit function is not appropriate for BLR = 0 pulses. A study has shown that BLR = 0 pulses can be fitted with accuracy comparable to BLR = 29 pulses by using a simple quadratic function. For the first data collected with the south arm, the fitting routines were not used in the interest of simplicity. We chose to use BLR = 28 and simply take the average

of the last three samples to get the pulse height. The probability of out of time pulses or pulse pileup was low enough that the start time of the pulse was set to zero for all events. In the future, we will likely choose to fit the pulse samples and make a determination of the start time to perform more detailed corrections.

The muon tracker electronics experienced a number of challenges and some hardware failures after installation in the PHENIX interaction region. This is certainly not unexpected for a new detector of this complexity. The first challenge was controlling the noise levels in the detector. The front end of the electronics is extremely sensitive to input charge, and is complicated by the fact that the preamplifier chips are not located on the wire chambers, due to space constraints. A number of different grounding configurations were studied. The final arrangement which seemed to work best was to ground all the chamber frames and the metallic boxes housing the electronics boards to the south magnet steel. Fortunately, the operation of the magnet power supplies had no effect on the noise levels. A second contribution to the noise was found to be electromagnetic pickup from the station 2 chambers. Stations 1 and 3 have thick outer skins which provide good shielding for incoming radiation. Station 2, however, has very thin mylar windows. For Station 2, electromagnetic pickup was reduced by covering the station 2 mylar chamber windows with thin aluminum foil grounded to the chamber frames.

With this grounding scheme, the noise levels were close to the design specification ($\sim$ 1.5 ADC counts). Most areas of stations 1 and 3 had noise levels around

1.5 ADC counts, with isolated areas of higher levels. Station 2 had larger noise levels overall, with an average of around 3 ADC counts. Figure 4.13 shows the rms noise levels in ADC counts for the cathode strips on the six planes in one octant of station 1. Figure 4.14 shows the rms noise levels for an octant in station 2. The station 2 noise levels show a dependence on the strip length, similar to the hit averages discussed previosly. This is likely due to the increase in capacitance value as the strip length increases.

During the data taking period 10 of the 168 front end modules in the south arm experienced a hardware failure which prevented them from taking useful data. The loss of an FEM takes out all cathode planes in that area because of the way the analog cables are attached. Thus, the acceptance loss due to inoperative electronics is more severe than for disabled high voltage anode planes, since in the case of disabled high voltage a track can still be found even if one plane is missing. The distribution of the disabled FEMs is also important for the overall acceptance. We experienced an FEM failure rate of 10% for station 1, 6.25% for station 2, and 3.1% for station 3. The approximate acceptance loss for dimuons from electronics failure alone was estimated to be 35%. Combined with the 15% loss from disabled high voltage, the total acceptance loss for dimuons in run 2 was approximately 50%.

The gain of the cathode chambers is measured by the calibration system. A programmable pulse generator injects a voltage pulse onto a subset of the

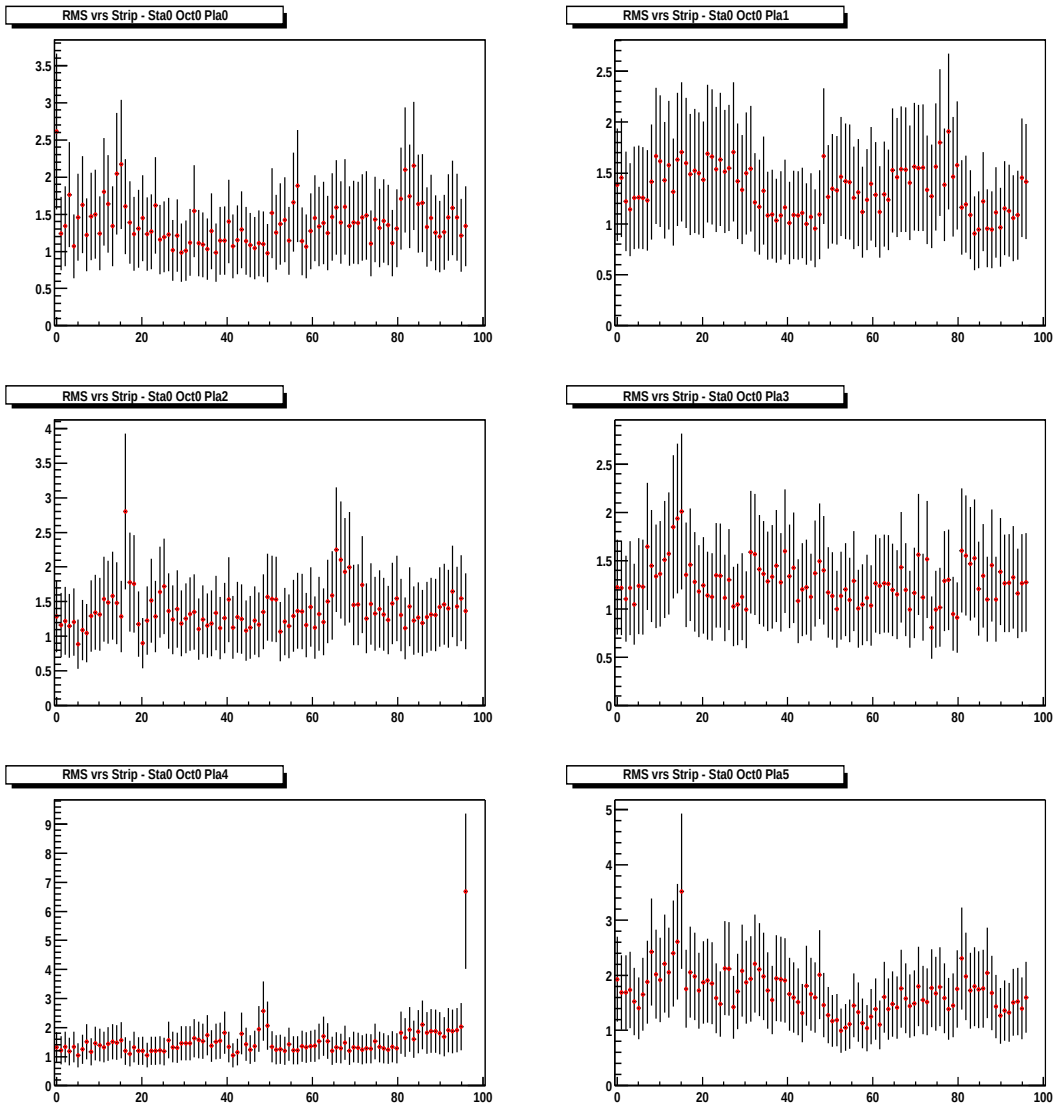

Figure 4.13: RMS noise in ADC counts for the six planes in one octant of station 1. The vertical axis is the rms noise, the horizontal axis is the strip number.

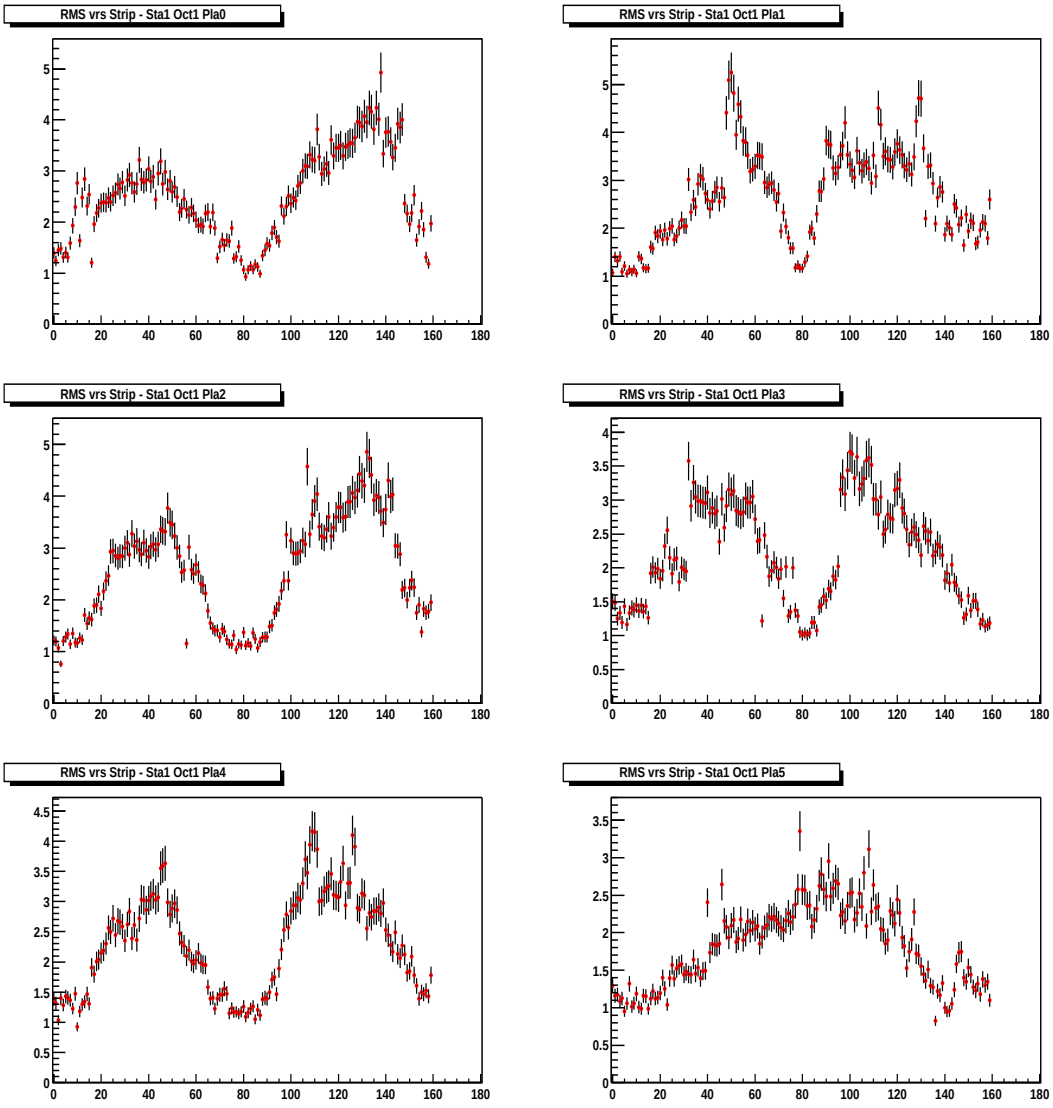

Figure 4.14: RMS noise in ADC counts for the six planes in one octant of station 2. The vertical axis is the rms noise, the horizontal axis is the strip number.

anode wires in each chamber. This induces a pulse on the cathode strips which is digitized. The gain is defined as the digitized pulse amplitude on a cathode strip divided by the DAC setting of the pulse generator. Several DAC amplitudes are used in a typical calibration run, and a plot of the cathode strip pulse amplitude versus the input DAC setting is made. The plot is then fitted with a straight line, and the slope of the line is the gain. Figure 4.15 shows the gain for the six planes in one octant of station 1. The average gain for our system is about 10. The gain is quite linear over most of the dynamic range. If a graph is made of the output pulse amplitude versus the calibration pulser DAC setting, a residual can be determined by fitting the graph with a straight line and computing the deviation from that line at different pulser DAC settings. Figure 4.16 shows the residuals from a linear fit for six cathode strips in station 2. Generally, the residuals from a straight line fit are less than two ADC counts.

The signal to noise ratio was designed to be 100:1. Figure 4.17 shows the peak charge for cathode clusters at station 2 in ADC counts. The distribution peaks around 120 ADC counts. With an RMS noise level of about 1.5 ADC counts, this gives a signal to noise ratio slightly less than the design value. Station 2 is somewhat worse because of its larger noise levels. A small secondary peak at large ADC values indicates a saturation effect in the preamplifier.

The muon tracking electronics suffered from some component failure during its first data taking period, but overall the performace was close to the design speci-

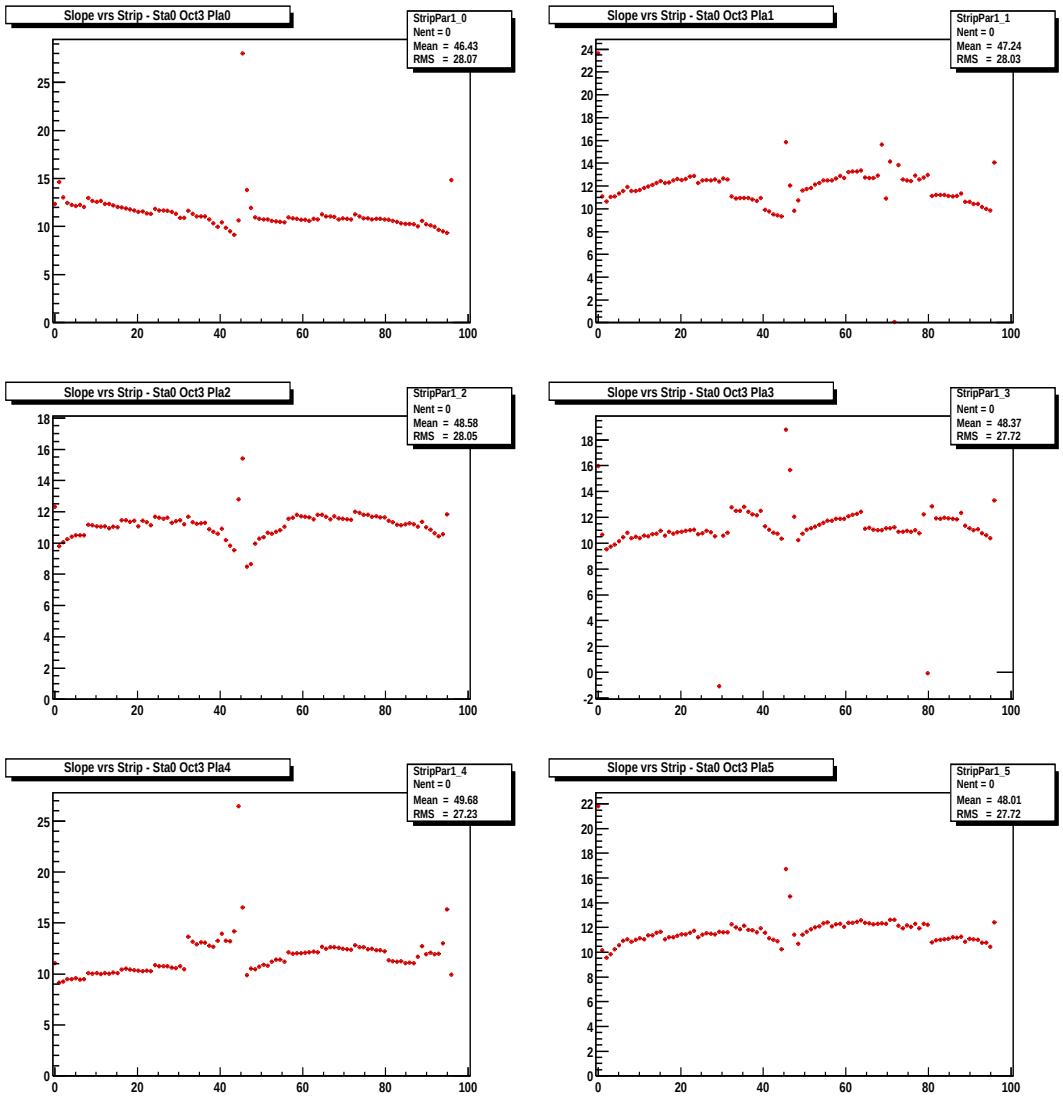

Figure 4.15: Measured gain for the six planes in one octant of station 1. The vertical axis is the gain, the horizontal axis is the strip number.

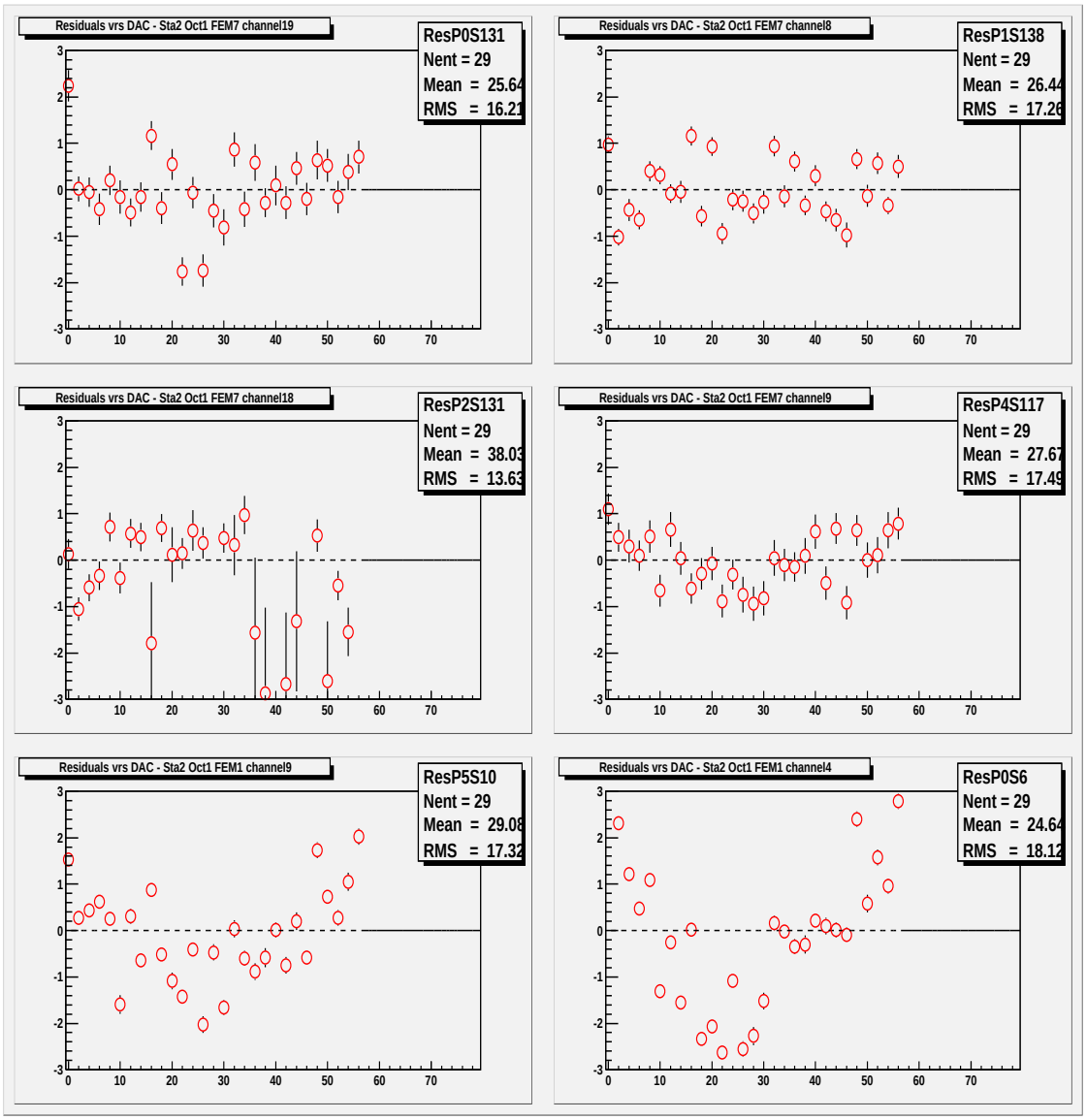

Figure 4.16: Residuals from a straight line fit of output pulse height versus pulser DAC setting for six cathode strips in station 2. The vertical axis is ADC counts, the horizontal axis is the pulser DAC setting.

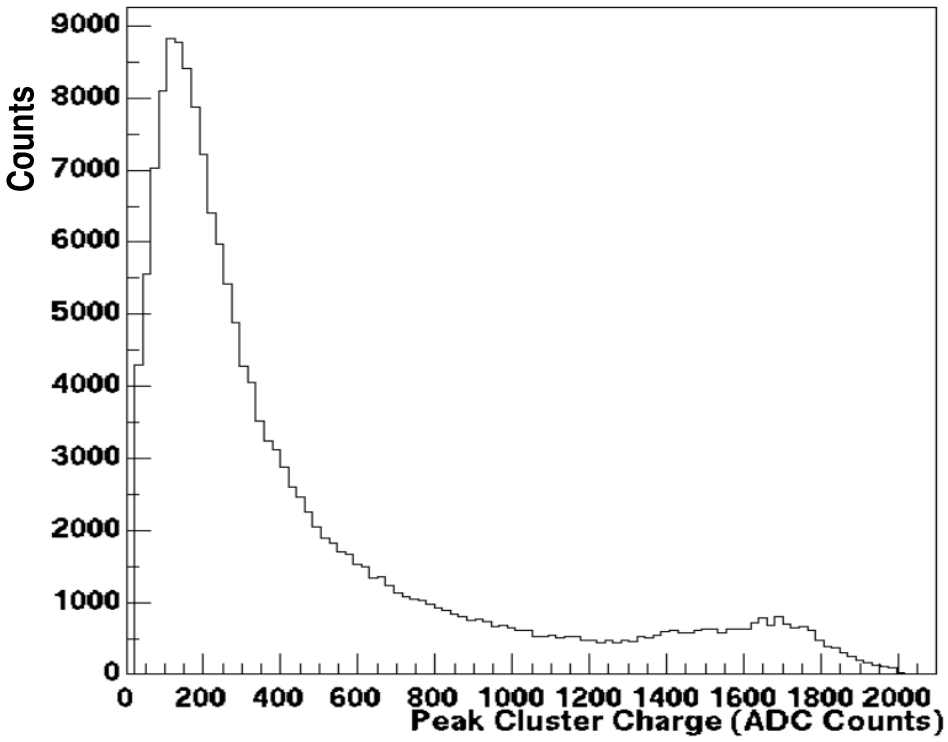

Figure 4.17: Peak charge in ADC counts for cathode clusters at station 2.

fications. There is room for further improvement in the area of noise suppression, in particular on station 2 electronics. In addition, the FPGA code used for run 2 can be improved. The data conversion time per event needs to be reduced from 55 μs to 40 μs to accomodate higher event rates, and the code is only able to buffer data for four events, instead of the design specification of five events.

4.3 Muon Identifier Performance

The muon identifier had one serious problem which was addressed during the run. This problem arose from very high hit rates due to events coming from the beam pipe and also from one of the RHIC beam magnets, which is located close to the detector [Cia 02]. These extra hits complicate the road finding and degrade the rejection power of the muon triggers. The percentage of hits orginating from the beam pipe area was as large as 80%. Six inches of iron shielding were added to the floor and two walls of the square hole, which houses the beam pipe in the center of the muon identifier. The ceiling was left unshielded due to lack of time to engineer a solution for how to support it. After installation of the shielding, the hit rates of the identifier panels were reduced by 5%, 23%, 63%, and 58% for gaps 1, 2, 3, and 4 respectively. The rejection factor (factor by which background events are rejected) for the dimuon trigger increased from 6 to 44 with the iron shielding.

To affirm that the muon identifier hits are from collisions and not beam gas events, the total number of hits should increase with the BBC total charge. The relation is shown in Figure 4.18, where a strong correlation is observed.

Figure 4.19 shows a comparison of the hit occupancy of the MuId tubes as a function of their distance from the beam axis. A reduction of hit occupancy as the distance from the beam axis increases is observed in the simulation and the

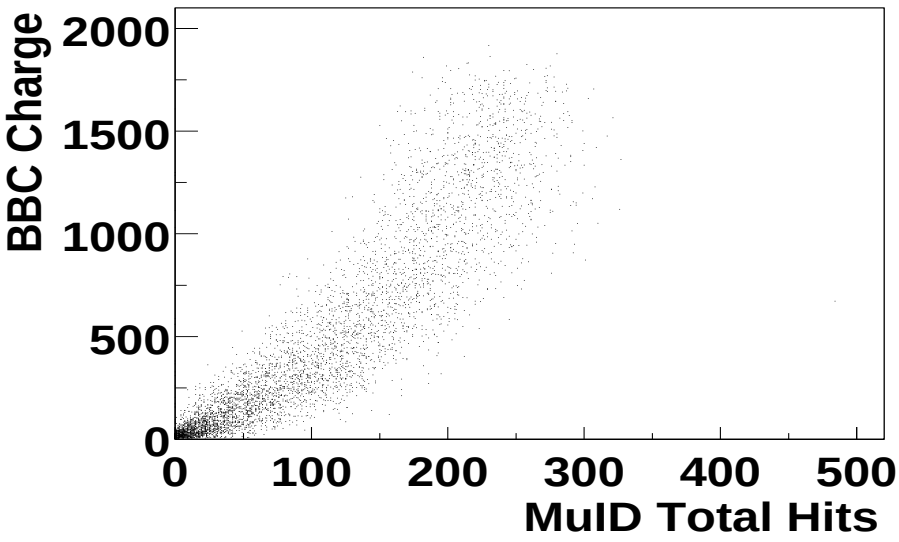

Figure 4.18: Observed correlation of MuId hits with BBC total charge (taken from [Cia 02]).

experimental data, with good agreement.

Figure 4.20 shows the occupancy of the five MuId gaps for simulation and data. The occupancy decreases as the distance traveled into the MuId increases. Gap 4 is slightly higher than gap 3 due to particles eminating from the beam pipe area.

4.4 Integrated Performace

As an integrated system, the muon spectrometer has demonstrated the ability to identify muon tracks. Figure 4.21 shows a PHENIX event display depiction of a cosmic ray track in the detector. The muon identifier panels are displayed, along with the hit cathode strips in the three tracking stations. A line connecting

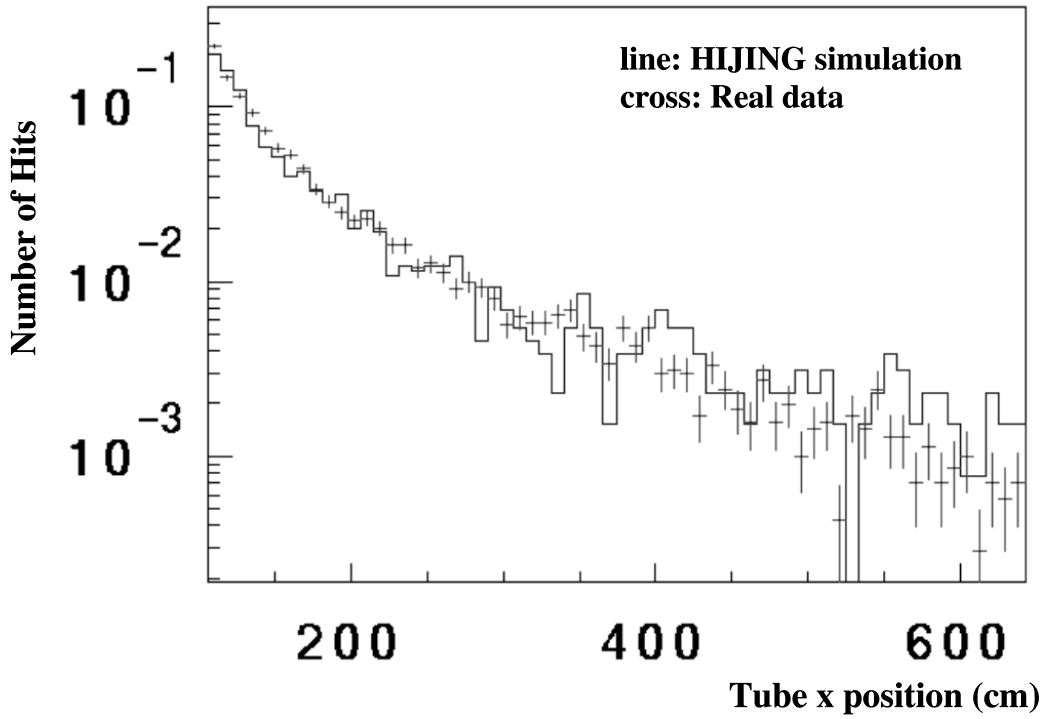

Figure 4.19: MuId tube hit occpancy as a function of distance from the beam axis.

the cathode strip hits and the MuId hits represents the muon track. Figure 4.22 shows the average momentum distribution of tracks for several runs of Au data. The track momentum drops off sharply below 2 GeV, the approximate minimum momentum required to reach the muon identifier. Figure 4.23 shows the $x_{_F}$ distribution for single muons in the south arm from several runs of Au data. The conclusive evidence that we are observing muon tracks can be obtained by the observation of the J/ψ mass resonance. This will be the topic of Chapter 5.

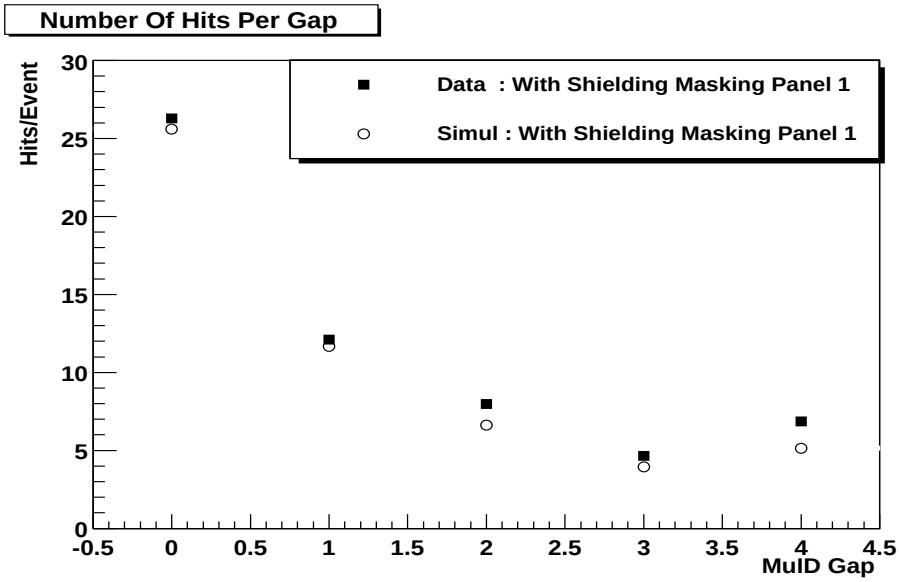

Figure 4.20: MuId gap occpancy for simulation and real data.

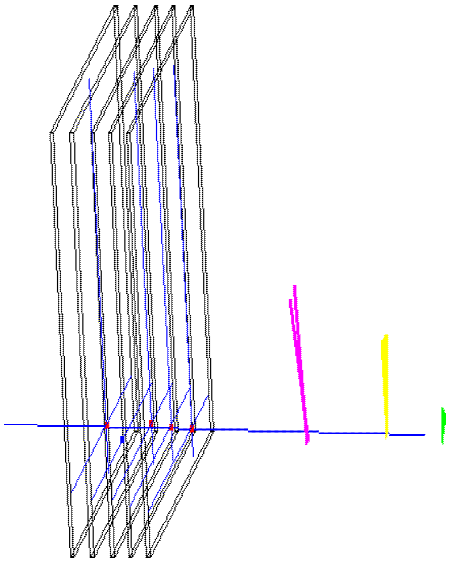

Figure 4.21: Event display depiction of a cosmic ray track in the south muon spectrometer.

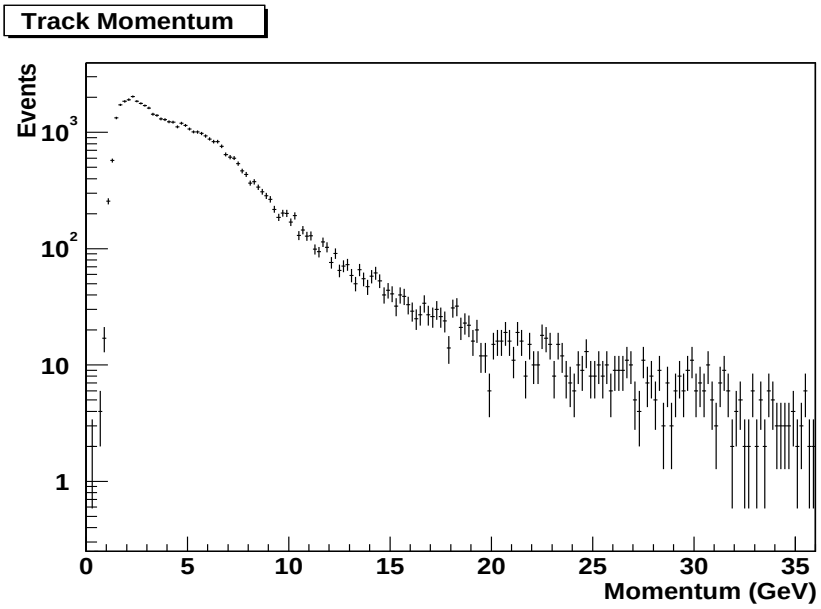

Figure 4.22: Momentum distribution of found tracks for a collection of Au runs.

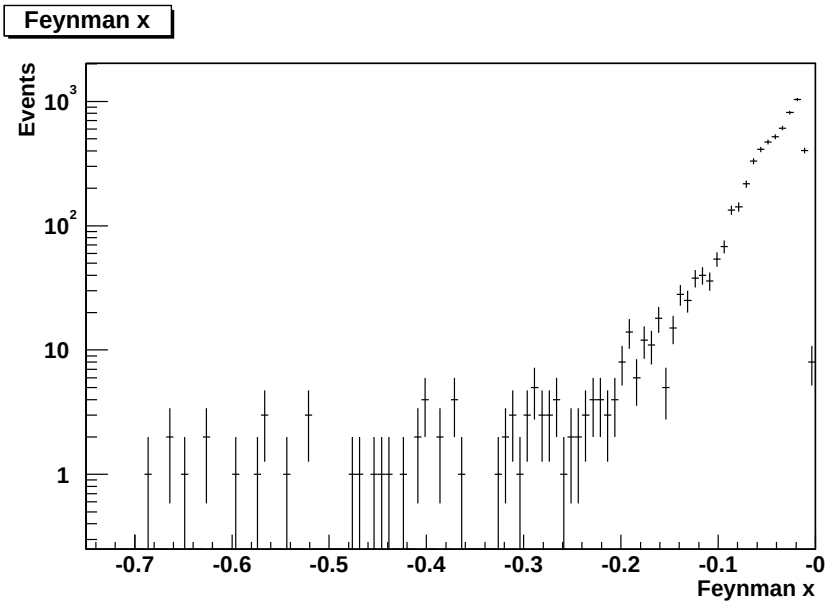

Figure 4.23: Feynman x for single muons from several Au runs.

5 DIMUON ANALYSIS FROM RUN 2 PROTON DATA

An important feature of the dimuon mass spectrum is the J/ψ resonance. Observation of the J/ψ will serve as an important confirmation that the detector is functioning properly, and there is also interesting and important physics which can be studied via the dimuon channel. A presentation of the dimuon analysis from run 2 proton data follows, with emphasis on extraction of the J/ψ mass peak, a measurement of the J/ψ cross section, and an outline for performing a J/ψ polarization measurement.

5.1 Dimuon Identification Algorithm

Construction of muon tracks is performed in an iterative process involving both the muon identifier and the muon tracker. The process begins by projecting a road from the muon identifier onto station 3 of the muon tracker. A search window on station 3 is defined to find hits which may be compatible with the muid road. If muon tracker hits are found inside this search window, the hits are connected to the muid road and the track is started. Next, a search window is defined at station 2, with allowances for multiple scattering within the chambers and the bending of the track in the magnetic field. If hits are found within that window, the track is extended from station 3 to those hits at station 2. The procedure is continued for station 1, and finally the track is projected to the vertex

position. This initial track is adjusted until the least squares fit is found. Dimuon tracks for an event are made by forming all possible combinations of single tracks.

5.2 Data Set Summary

This analysis uses pp events which have fired the muon identifier dimuon trigger. The data files used are from the third dimuon reconstruction pass (completed in June 2002), which used the pro.27 libraries and version 2 of the MuTr alignment constants. Some runs have been excluded due to hardware or DAQ problems (HV trips, HV studies, GLINK problems). Only runs with a Muon Tracker high voltage duty factor (fraction of channels enabled) > 0.89 are used. In addition, run numbers below 39000 are not used. This is done for two reasons. First, it is consistent with the run numbers used for the preliminary PHENIX J/ψ cross section measurement [Sat 02], and second, an analysis of run numbers below 39000 shows only 3 counts in the J/ψ mass region. Therefore, these runs are almost entirely background events. Several event selection cuts were applied. These cuts are:

- muon tracks must not be tagged as ghosts
- muon probability flag must be 1
- number of reconstructed tracks in the event < 50
- muon track χ^2 per degree of freedom (χ^2/DOF) must be < 200
- a valid BBC vertex which satisfies -38 cm $<$ z vertex $<$ +38 cm is required
- $x_F < 1$ and $p_T < 15$ GeV for dimuon pairs

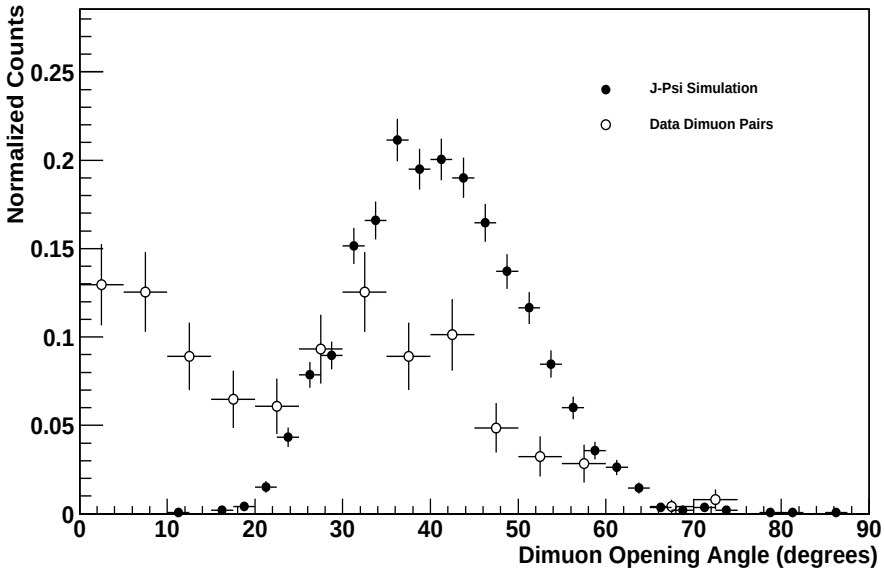

Figure 5.1: Dimuon opening angle for simulation and real data. Solid points represent the simulated J/ψ opening angle, open points represent the opening angle for unlike sign dimuon pairs from the real pp data.

- opening angle of the dimuon pair is $> 10^{o}$

Most of these cuts are simply to eliminate occasional spurious tracks produced by the track finding routines. The cut on the opening angle of the dimuon pair, however, is used to reduce the background. Figure 5.1 shows the opening angle for J/ψ simulated with PYTHIA and the detector response, along with the unlike sign dimuon pairs from the pp data. The simulation and real data histograms have been normalized by their respective number of entries. One can see that all dimuon pairs originating from simulated J/ψ decays have an opening angle greater than 10^{o}, whereas the unlike sign dimuon spectrum from the real pp data has opening angles below 10^{o}. Thus, a cut on the opening angle of the dimuon

pair greater than 10° is used to reduce the background while not affecting the J/ψ signal.

5.3 J/ψ Simulation

To study J/ψ production in the south muon arm, PYTHIA was used to generate J/ψ events, PISA simulated the geometrical configuration of the detector, and the simulation detector response and reconstruction software was used to model inactive detector regions and electronic noise. Run 40087 was used to simulate the inactive HV regions and to retrieve the electronics calibration parameters from the database. The list of inactive muon tracker FEMs was constant during the run and those FEMs were turned off in the simulation. Real muon identifier tube efficiencies are used. The simulated J/ψ events are required to fire the muon identifier dimuon trigger (one deep/one shallow road or two deep roads). The vertex distribution for the events is smeared with an rms of 22 cm. Figure 5.2 shows the ϕ angle distribution for one of the decay muons for simulated J/ψ events and for the real dimuon data. The similar shapes in the ϕ distribution show that run 40087 does a reasonably good job at simulating the active regions of the real detector. The statistics for the real data are considerably less than for the simulation, which will produce some random variations when comparing the two distributions. Figure 5.3 shows the reconstructed dimuon mass for the simulated J/ψ signal in the south muon arm at $\sqrt{s} = 200$ GeV. The mass peak is fitted with

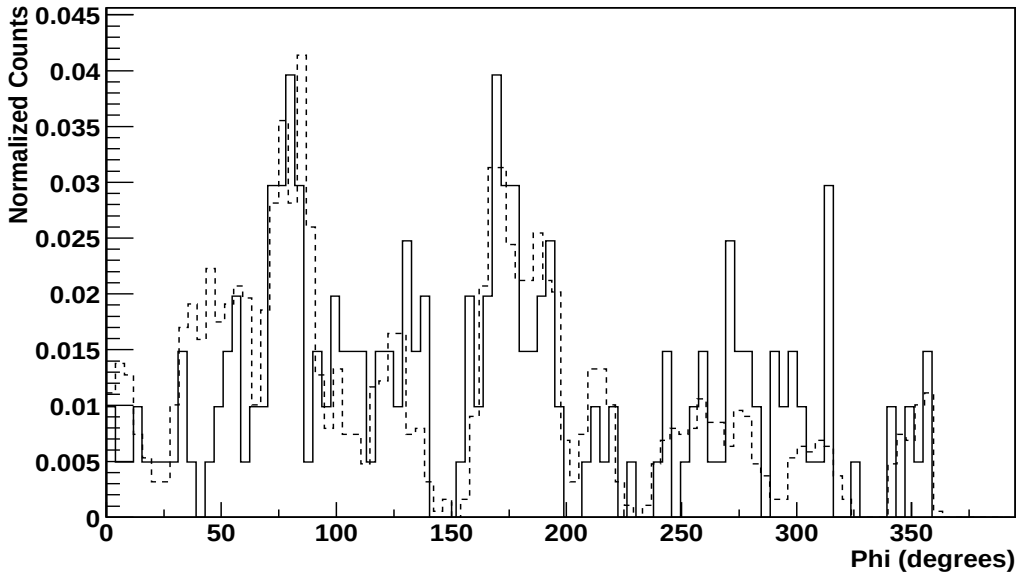

Figure 5.2: ϕ angle distribution of one decay muon for simulated J/ψ events (dashed line) and the real dimuon data (solid line). The histograms are normalized by their number of entries.

a gaussian function. The mean of the mass peak fit is at 3.12 GeV, very close to the known J/ψ mass of 3.097 GeV. The mass resolution is 213 MeV. Mass resolutions on the order of 120 MeV can be attained using a completely active detector and an electronics noise level of 2 ADC counts. Because this simulation includes inactive high voltage areas, inactive electronics, and actual electronics noise levels, the mass resolution is decreased from the ideal case.

Figure 5.4 shows the p_t spectrum for the simulated J/ψ events for which both decay muons are reconstructed in the south muon arm, and Figure 5.5 shows the $x_{_F}$ spectrum. The rapidity spectrum for simulated J/ψ events in the south arm is shown in Figure 5.6. The coverage is -2.2 $< y <$ -1.2.

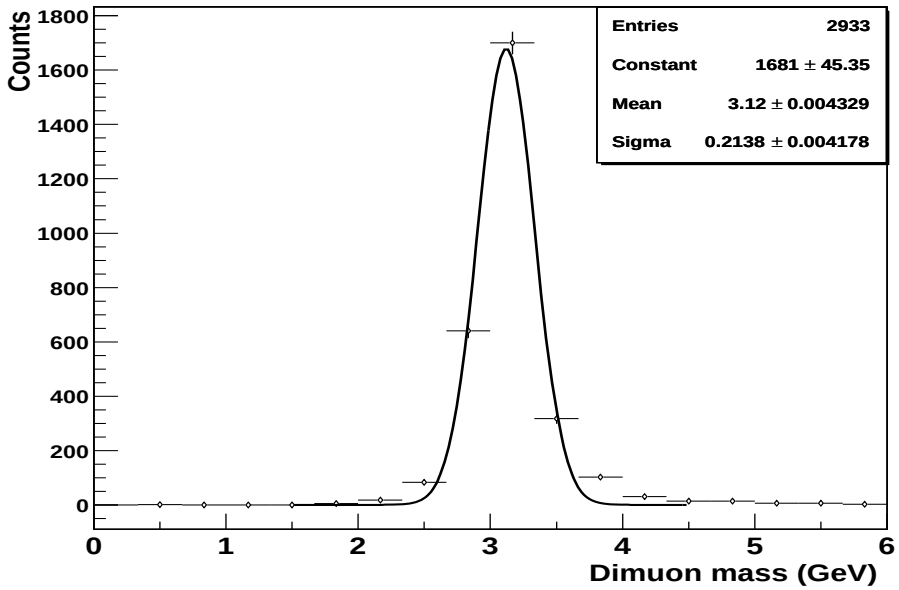

Figure 5.3: Dimuon mass for a simulated J/ψ signal in the south muon arm at $\sqrt{s} = 200$ GeV.

5.4 Comparison of Real Data to Simulation

A comparison will be made between the J/ψ simulation and the real data. It is important to verify that the simulation reproduces the same properties that are observed in the data.

To perform the comparisons, the J/ψ simulation data will be compared to the unlike sign muon pairs from the real data in the mass range 2.3 GeV to 4.0 GeV. Because there is very little background from like sign pairs in the J/ψ mass region this should provide a reasonably good comparison. For these comparisons, real pp data chamber hits were embedded into the simulation to reproduce the effect of realistic multiplicities on the track finding routines.

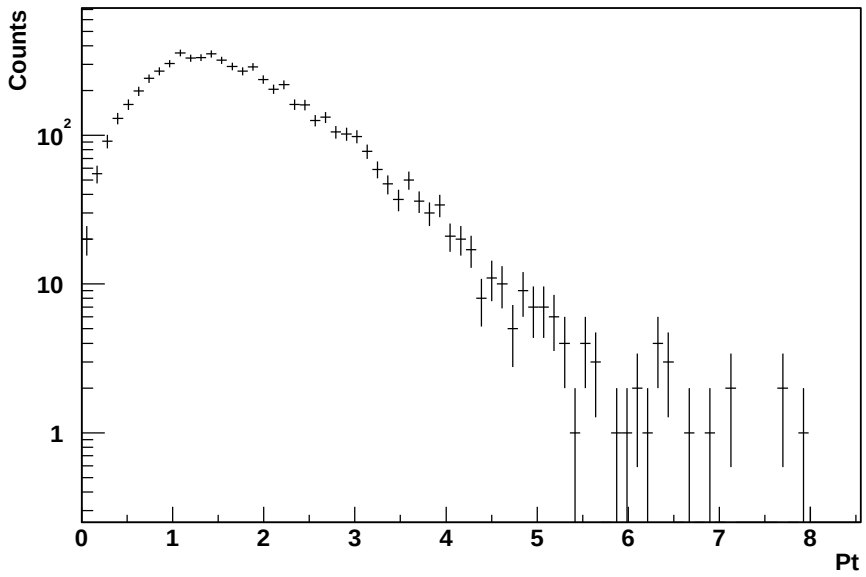

Figure 5.4: p_t spectrum for simulated J/ψ events in the south muon arm at $\sqrt{s}$ = 200 GeV.

The opening angle of the dimuon pairs is shown in Figure 5.7. It can be seen that the J/ψ dimuons always have an opening angle of at least 10°. The simulation and real data distributions are in good agreement.

The match position is defined by projecting a MuId road for a track onto station 3 of the MuTr and computing the distance from the projected road to the position of the fitted track at station 3. The match angle has a similar definition, it is the difference between the θ angle of the track and the projected MuId road at station 3. Figure 5.8 shows the match position, and Figure 5.9 shows the match angle for simulation and real data. The match position peaks at about 10 cm, and most tracks have a match position less than 30 cm. The match angle is

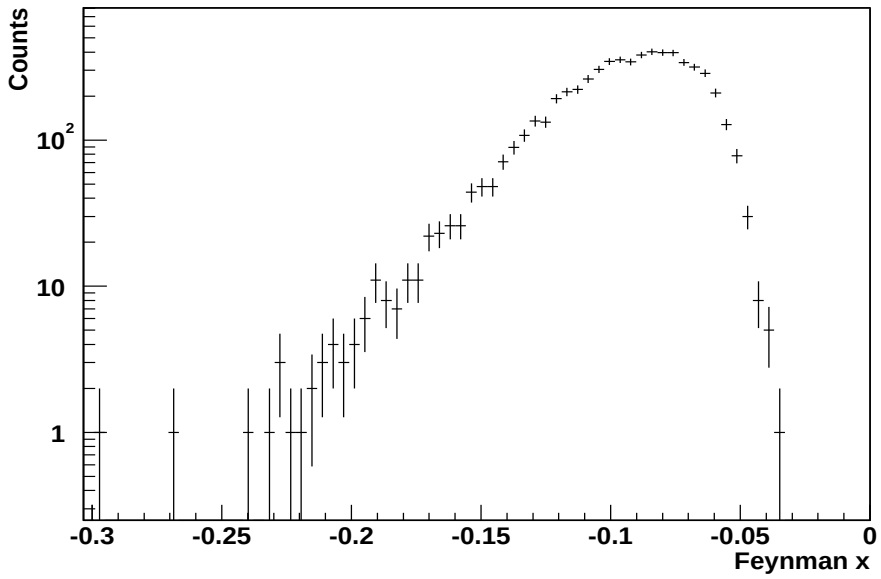

Figure 5.5: x_F spectrum for simulated J/ψ events in the south muon arm at $\sqrt{s}$ = 200 GeV.

typically less than 10^o. The simulation and data are in good agreement.

For each track a χ^2/DOF value is computed. Tracks with a small χ^2/DOF have small deviations between the chamber hits and the fitted track. Figure 5.10 shows the χ^2/DOF distribution for the simulation and real data. The simulation and data are in good agreement, with the majority of tracks occuring at small χ^2/DOF values. A track which is well fitted will give a χ^2/DOF of about 1. In Figure 5.10 many of the tracks have values approaching 1, implying that the tracks being found are good fits to the chamber hits.

A muon vertex position can be computed from a track by calculating the distance of closest approach of the track to the z axis. This muon vertex can be

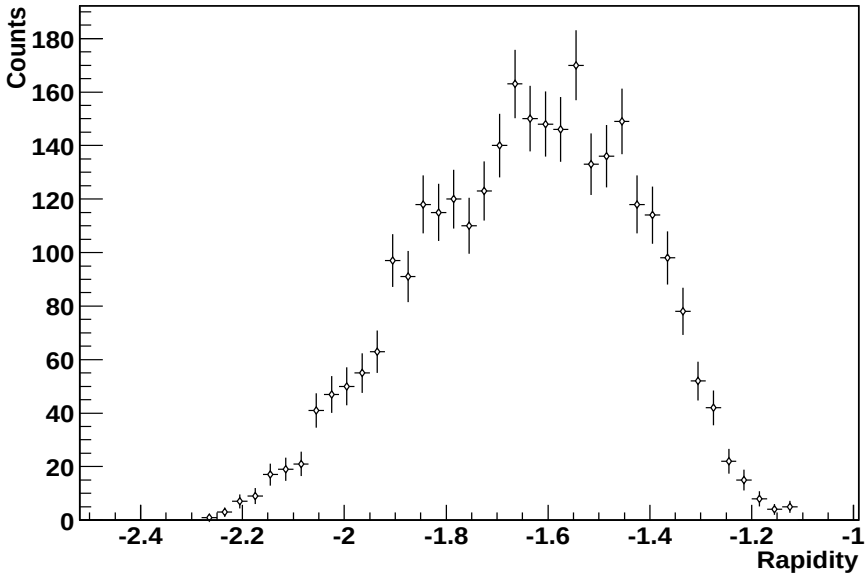

Figure 5.6: Rapidity spectrum for simulated J/ψ events in the south muon arm at $\sqrt{s} = 200$ GeV.

compared for the two muons in a dimuon event to see if both muons are coming from the same vertex. A comparison can also be made between the muon vertex and the event vertex from the BBC detector. Figure 5.11 shows the difference between the two muon vertices for a dimuon event, and Figure 5.12 shows the difference between the muon vertex for one of the dimuon tracks and the BBC vertex. Both distributions are centered on zero as expected. The two muon track vertices and the muon track and BBC vertices generally agree within 30 cm.

Figure 5.13 shows the sum of the last MuId plane reached by the two muons in the dimuon pair. The five MuId planes are numbered from 0 to 4. The simulation is in good agreement with the data, showing that dimuons from J/ψ decay

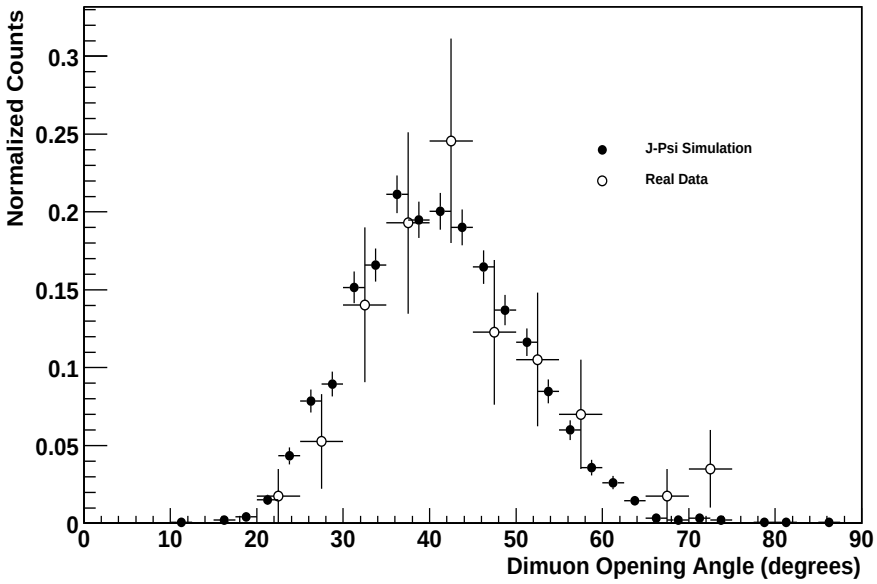

Figure 5.7: Opening angle of the dimuon pair for the simulation and real data.

generally have a last plane sum ≥ 6.

Figure 5.14 shows the p_t distribution for dimuons reconstructed in the south muon arm for the simulation and the real data. The simulation and real data are in good agreement.

Finally, Figure 5.15 shows the $x_{_F}$ distribution for dimuons reconstructed in the south muon arm for the simulation and the real data. Again, the simulation and real data are in good agreement.

Overall, the J/ψ simulation is in good agreement with the observed data when comparing basic track quality parameters as well as physics properties like p_t and $x_{_F}$ distributions. This increases the confidence in acceptance and efficiency

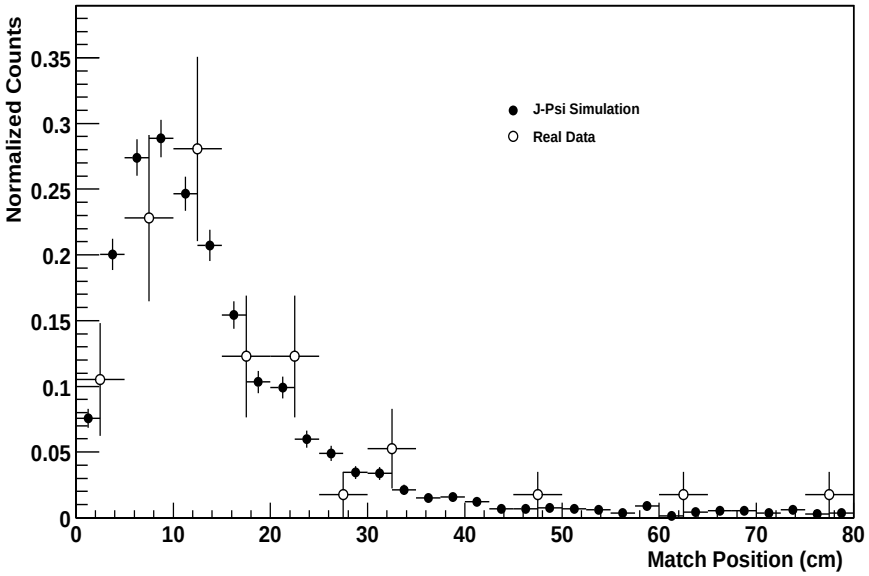

Figure 5.8: Match position at station 3 for the simulation and real data.

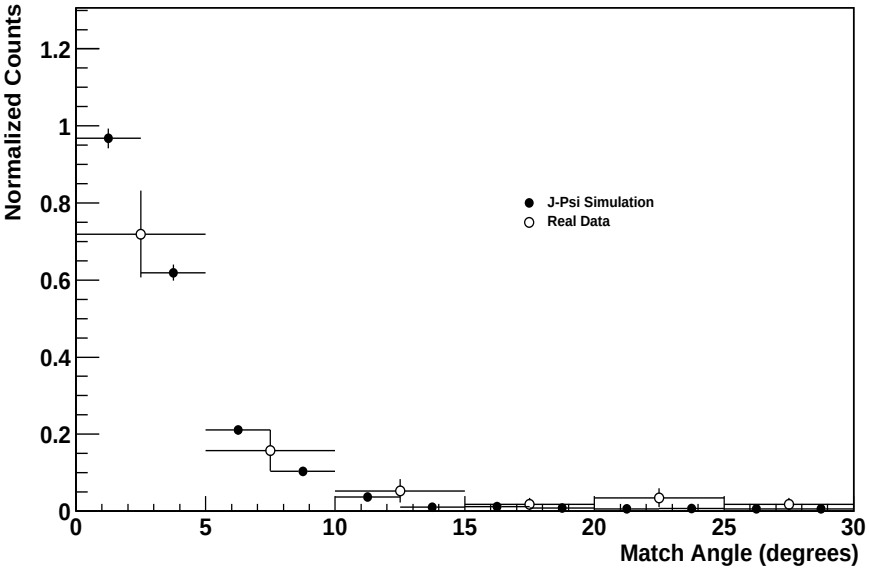

Figure 5.9: Match angle at station 3 for the simulation and real data.

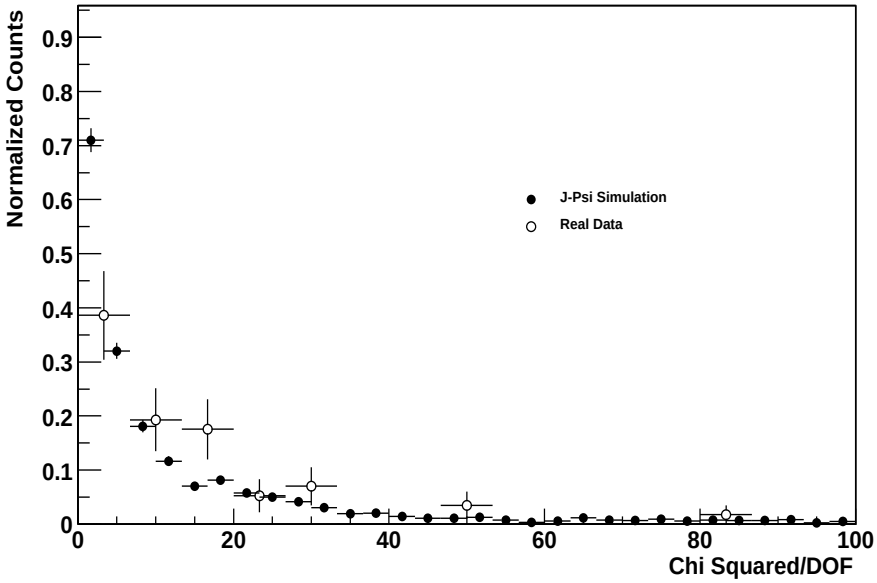

Figure 5.10: Muon track χ^2/DOF for the simulation and real data.

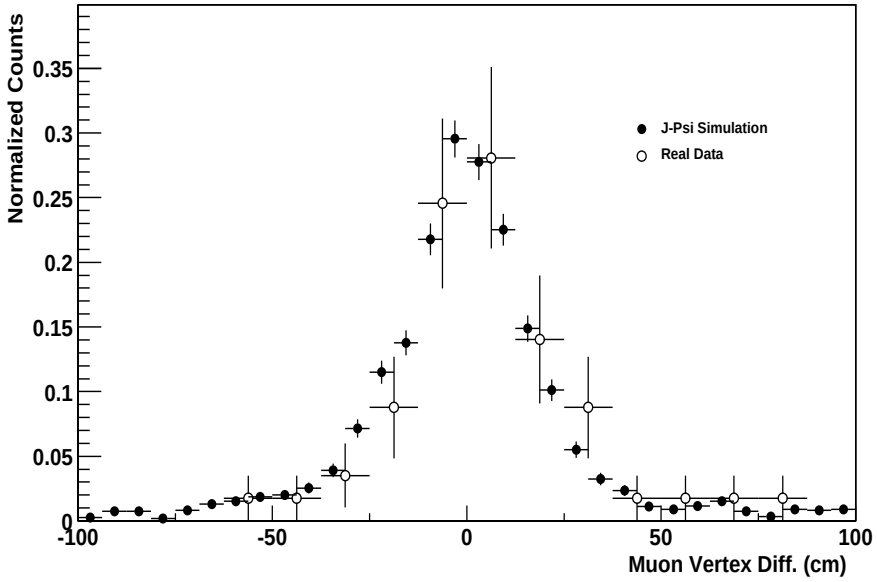

Figure 5.11: Difference between the two muon track vertices in a dimuon pair for the simulation and real data.

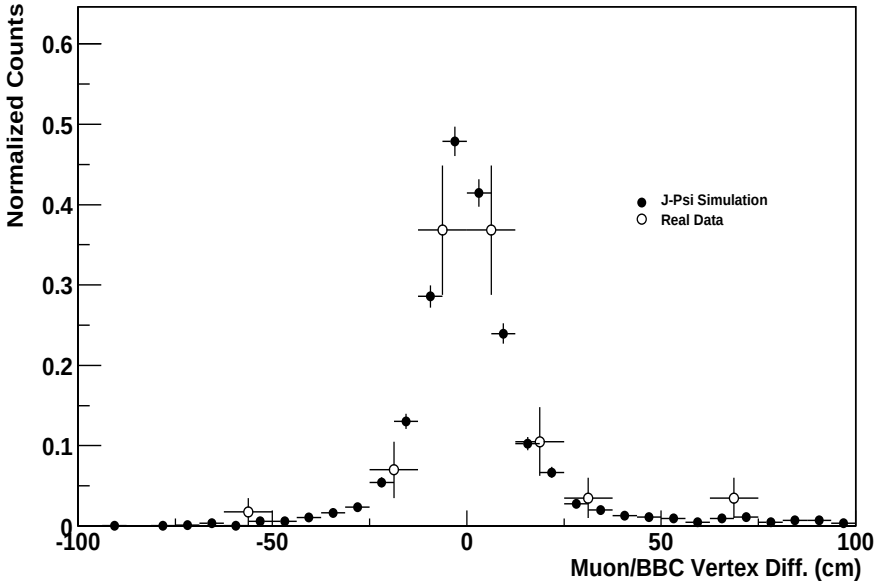

Figure 5.12: Difference between one of the muon track vertices in a dimuon pair and the BBC vertex for the simulation and real data.

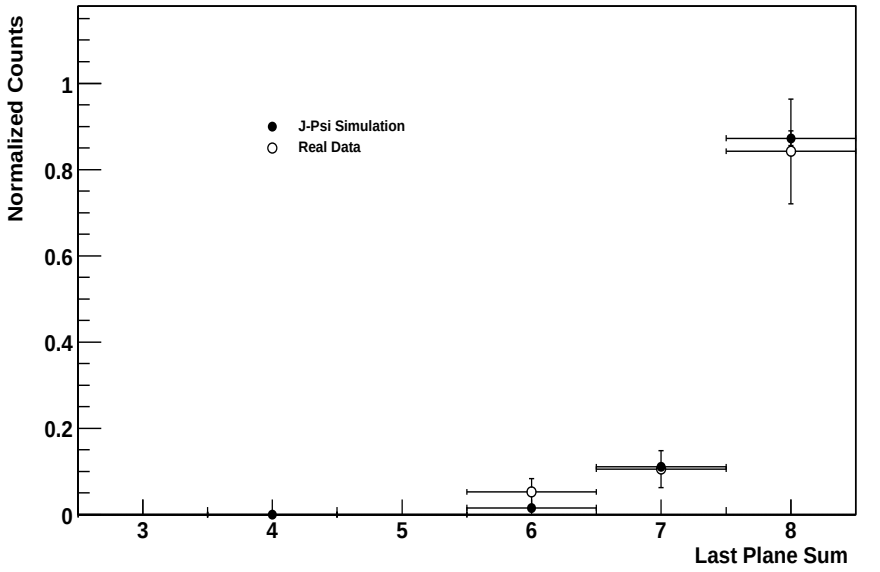

Figure 5.13: Sum of last MuId plane reached for the two muons in a dimuon pair for simulation and real data.

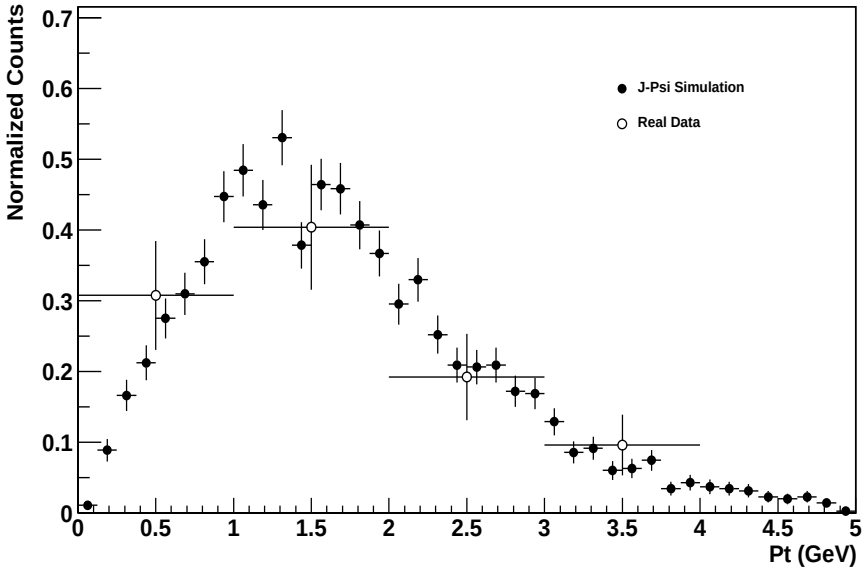

Figure 5.14: Dimuon p_t for simulation and real data.

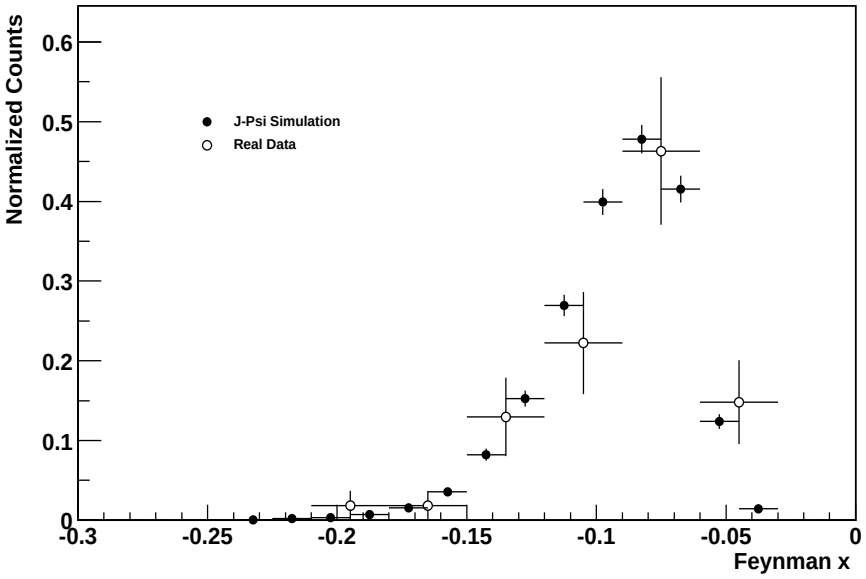

Figure 5.15: Dimuon x_F for simulation and real data.

calculations which rely on an accurate simulation.

5.5 J/ψ Cross Section

The cross section for J/ψ production is given by

$$\sigma_{J/\psi} = \frac{\mathrm{N}_{J/\psi}}{\mathcal{L}} \tag{5.1}$$

where $\mathrm{N}_{J/\psi}$ is the number of J/ψ produced for the integrated luminosity $\mathcal{L}$. The number of J/ψ produced is related to the number of J/ψ observed in the muon arm by

$$\mathrm{N}_{J/\psi} = \frac{\mathrm{N}^{\mathrm{det}}_{J/\psi}}{(\mathrm{A}\epsilon)_{\mu^+\mu^-}\mathrm{B}_{\mu^+\mu^-}} \tag{5.2}$$

where $\mathrm{N}^{\mathrm{det}}_{J/\psi}$ is the number of J/ψ observed in the detector, $(\mathrm{A}\epsilon)_{\mu^+\mu^-}$ is the product of the acceptance and the efficiency of the detector for $J/\psi \to \mu^+\mu^-$ events, and $\mathrm{B}_{\mu^+\mu^-}$ is the branching ratio for $J/\psi \to \mu^+\mu^-$. The integrated luminosity is given by

$$\mathcal{L} = \frac{\mathrm{N}_{\mathrm{mb}}}{\epsilon_{\mathrm{mb}}\sigma^{\mathrm{tot}}_{pp}} \ . \tag{5.3}$$

N_{mb} is the number of minimum bias triggers with |z vertex|$<$ 38 cm, ϵ_{mb} is the fraction of events with |z vertex|$<$ 38 cm which fire the minimum bias trigger and have a reconstructed |z vertex|$<$ 38 cm, and σ^{tot}_{pp} is the total pp cross section at $\sqrt{s} = 200$ GeV.

Figure 5.16 shows the mass spectrum for unlike sign ($\langle +- \rangle$) and like sign ($\langle ++ \rangle + \langle -- \rangle$) dimuon pairs from the dataset described in section 5.3. Two

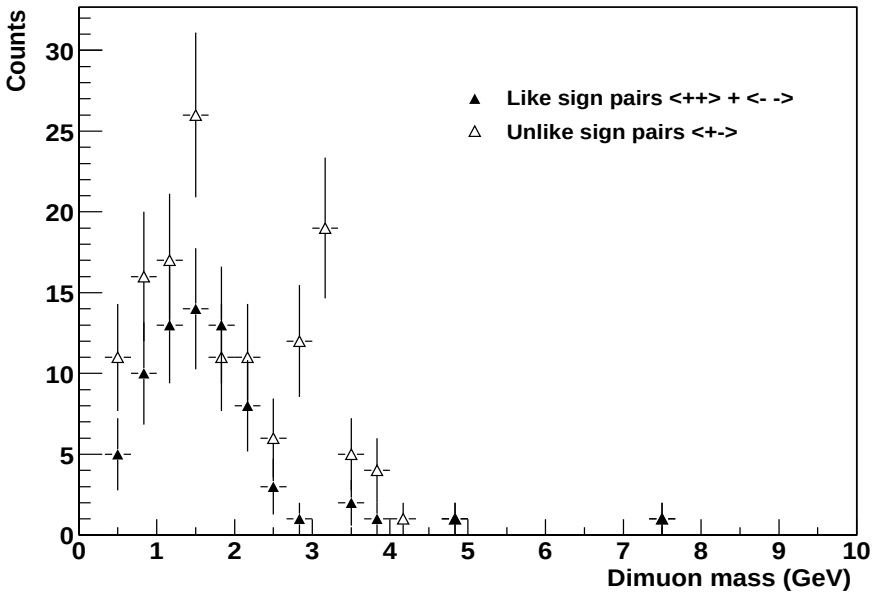

Figure 5.16: Dimuon mass spectrum for the pp dimuon data. Open triangles represent the unlike sign pairs, filled triangles represent the like sign pairs ($\langle ++ \rangle + \langle -- \rangle$).

properties of the mass spectrum are apparent. There appears to be an excess of unlike sign pairs compared to like sign pairs, and the J/ψ peak is quite obvious in the unlike sign spectrum at $\sim$3.1 GeV. The J/ψ peak can be isolated by performing a background subtraction. The background which will be subtracted from the unlike sign spectrum is constructed from the positive and negative muon pairs. The background is represented as

$$\mathrm{N}^{+-}_{\mathrm{back}} = 2\mathrm{RA}\sqrt{\mathrm{N}^{++}\mathrm{N}^{--}} \ . \tag{5.4}$$

R is a parameter which takes into account charge correlation effects, which are significant at low multiplicities. A is a parameter which accounts for any charge

asymmetry in the detector. This technique has been used in dimuon analysis on NA38/NA50, for example [Abr 00a]. For this analysis, A is assumed to be 1, and R will be determined from the data.

A more advanced approach would be to determine the R factor from simulations of pion and kaon decays, including the probablility of decay in the muon spectrometer factoring in absorber materials and the decay lengths (see [Abr 00a] for a compete description). A very simplistic simulation has been done with PYTHIA where pions and kaons generated from all QCD processes (MSEL=2) are decayed to muons and then combined to form dimuon pairs. The decays were done by giving the decay muon the same flight path as the parent meson, which is a reasonably good approximation to the actual decay kinematics. All the pions and kaons were assumed to decay to muons that passed through the muon spectrometer. Figure 5.17 shows the dimuon mass from the PYTHIA simulation for the unlike sign muon spectrum and the spectrum constructed using $2\sqrt{N^{++}N^{--}}$. An excess of unlike sign pairs over the $2\sqrt{N^{++}N^{--}}$ spectrum is evident.

One could conceivably incorporate the appropriate decay probablities for the muon spectrometer into the simulation and extract the R factor in this way. However, given the level of statistics available for this analysis, and the scarcity of background under the J/ψ peak, a simplified algorithm which determines R from the data should suffice. To determine the R factor, the positive and negative muon pairs are used to create a mass spectrum using $2\sqrt{N^{++}N^{--}}$. The bin entries

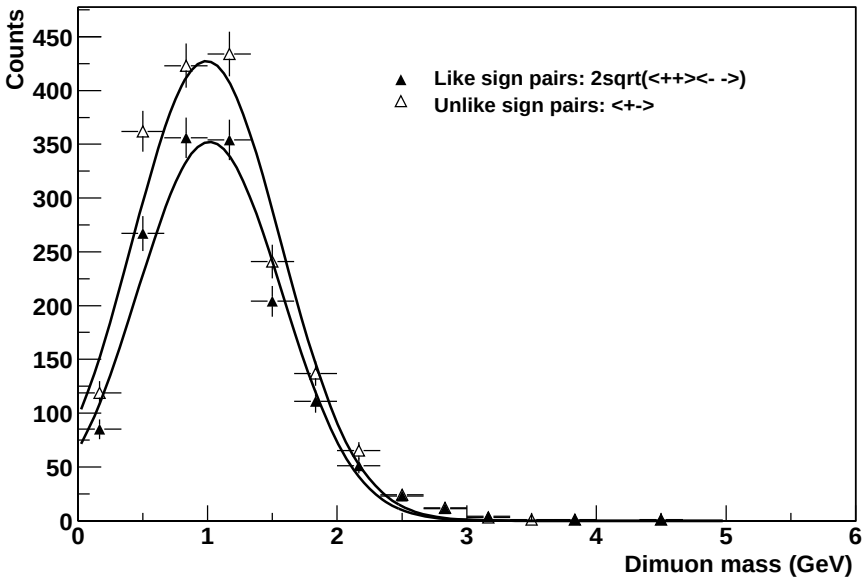

Figure 5.17: Dimuon spectrum from a PYTHIA simulation of pion and kaon decays. Open triangles represent the unlike sign mass spectrum, filled triangles represent the mass spectrum constructed using $2\sqrt{N^{++}N^{--}}$.

in the unlike sign spectrum and the $2\sqrt{N^{++}N^{--}}$ spectrum are then summed in the region below the J/ψ mass peak (0 GeV to 2.33 GeV). The R factor is then taken to be the ratio of the unlike sign spectrum bin sum to the $2\sqrt{N^{++}N^{--}}$ spectrum bin sum. Using this technique, the R factor is determined to be 1.52.

Once R is known, the background spectrum is determined using Equation 5.4. Figure 5.18 shows the unlike sign dimuon mass spectrum along with the background constructed from the like sign pairs (the $2RA\sqrt{N^{++}N^{--}}$ spectrum). To isolate the J/ψ signal, the background is subtracted from the unlike sign mass spectrum. The result of the subtraction is shown in Figure 5.19. The J/ψ peak is obvious, and the region around the J/ψ mass is fitted with a gaussian function.

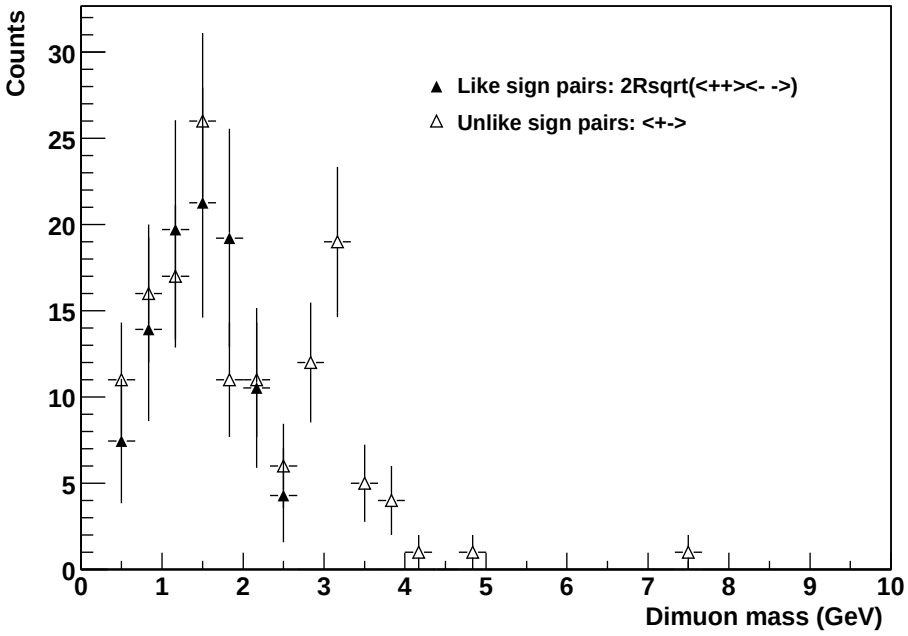

Figure 5.18: Dimuon spectrum from the real pp dimuon data. Open triangles represent the unlike sign mass spectrum, filled triangles represent the background constructed using Equation 1, with R = 1.52 and A = 1.

The mean of the fitted gaussian function is 3.08 $\pm$ 0.05 GeV, with σ = 279 $\pm$ 82 MeV. The mass resolution obtained in the simulation is 213.8 MeV (see Figure 5.3), which compares to the 279 MeV resolution observed for the J/ψ peak in the real data. The alignment of the Muon Tracker has improved since this data set was reconstructed. This means that the mass resolution of the real data may possibly improve to a value more consistent with the simulation in subsequent analysis of the data.

The number of J/ψ observed in the detector can then be calculated from the returned fit parameters:

$$\mathrm{N}^{\mathrm{det}}_{J/\psi} = \frac{\mathrm{N}\sigma\sqrt{2\pi}}{\mathrm{binwidth}} \ , \tag{5.5}$$

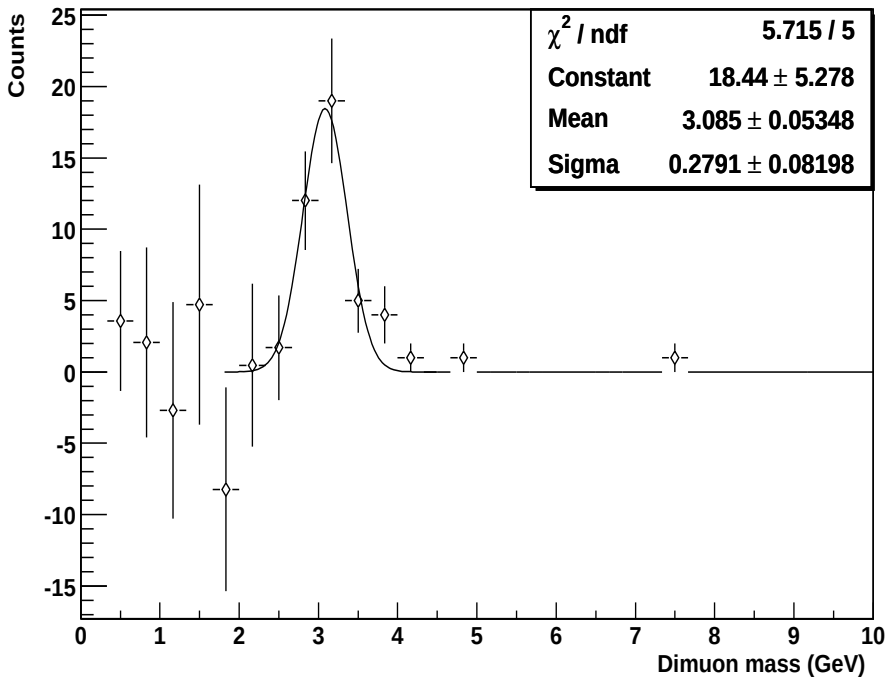

Figure 5.19: Background subtracted dimuon spectrum from the real pp dimuon data, with the J/ψ peak fitted by a gaussian function.

where N is the amplitude and σ is the width of the fitted gaussian function.

The number of J/ψ passing the cuts described in section 5.3 is found from Equation 5.5 to be 38.6 $\pm$ 16.0. If one simply counts the number of entries in the bins surrounding the J/ψ peak (from 2.33 to 4.0 GeV) one gets somewhat better statistical error. The number of J/ψ found by counting bins in this fashion is 41.7 $\pm$ 6.5.

The acceptance and efficiency for $J/\psi \rightarrow \mu^+\mu^-$ in the south muon arm is determined from the simulation. It is found that for J/ψ produced by PYTHIA over all space, 6.7% have dimuon decay products with total momentum at least

2 GeV (the minimum required to reach the muon identifier) and momentum θ angles such that both muons fall within the outer boundaries of the detector acceptance ($143^{o} < \theta < 171\ ^{o}$). The momentum cut and angular cut are used to select J/ψ events in the south arm from the event generator, and do not represent the total detector acceptance because there are other factors such as the chamber frames and some obstructing materials which reduce the acceptance further. Those factors are accounted for in the PISA portion of the simulation. Since we are interested in the product of the acceptance and the efficiency, we need only know the relation between the total number of events thrown in all space and the total number of events reconstructed by the detector. For J/ψ whose decay muon θ angles fall within the angular boundaries of the moun arm and have sufficient momentum to reach the muon identifier, it is found that 2.78% of those events will be reconstructed as a dimuon, after the additional obstructing material, inactive detector regions, and realistic electronic noise levels are accounted for. Then $(\mathrm{A}\epsilon)_{\mu^+\mu^-}$, the product of the acceptance and efficency for the south arm, is 0.00186.

The branching ratio for $J/\psi \rightarrow \mu^+\mu^-$ is well known [Hag 02], and $\mathrm{B}_{\mu^+\mu^-}$ is taken to be 0.0601.

The factors needed to compute the integrated luminosity have been studied in [Sat 02] and [Nag 02]. $\mathrm{N_{mb}}$ was found to be 1.72 x 10^9, the triggering efficiency is $\epsilon_{\mathrm{mb}} = 0.51$, and $\sigma_{pp}^{\mathrm{tot}} = 42.1$ mb is the pp total inelastic cross section taken from

[Hag 02]. Using all of these numbers as inputs to Equations 5.1, 5.2, and 5.3, gives $\sigma_{J/\psi} = 4.6 \pm 0.7$ (stat) μb. There are several sources of systematic errors. A 10% error is assigned to the number of J/ψ observed in the data to account for uncertainties in the background subtraction technique. For the acceptance and efficiency value, a systematic error of 18% is assigned to account for variations in MuId panel efficiencies, MuTr high voltage state variations, and a known bug in the simulation code affecting the acceptance of octant 7. The branching ratio is assigned an error of 3.2% as is done in [Hag 02]. N_{mb} is given an error of 5%, and ϵ_{mb} is given an error of 15% to account for uncertainties in the recorded data [Sat 02]. σ_{pp}^{tot} is given an error of 5%, consistent with the plot in [Hag 02]. An additional source of systematic error may be differences in the 4π rapidity distributions for $J/\psi \to \mu^+\mu^-$ produced with the PYTHIA event generator when compared to other generators, such as Ramona Vogt. This calculation assumes the PYTHIA rapidity distribution, shown in Figure 5.20, and I have not attempted to quantify a systematic error between different event generators. Considering all of the systematic errors, the value for the measured J/ψ cross section from the proton data is

$$\sigma_{J/\psi} = 4.6 \pm 0.7(\text{stat}) \pm 1.2(\text{sys})\mu\text{b} \ . \tag{5.6}$$

The measurement has been performed in a slightly different way in [Fra 02]. There, the muon data is divided into two bins of rapidity, and a mid rapidity point from a $J/\psi \to e^+e^-$ analysis is combined with the muon data. Figure 5.21 shows

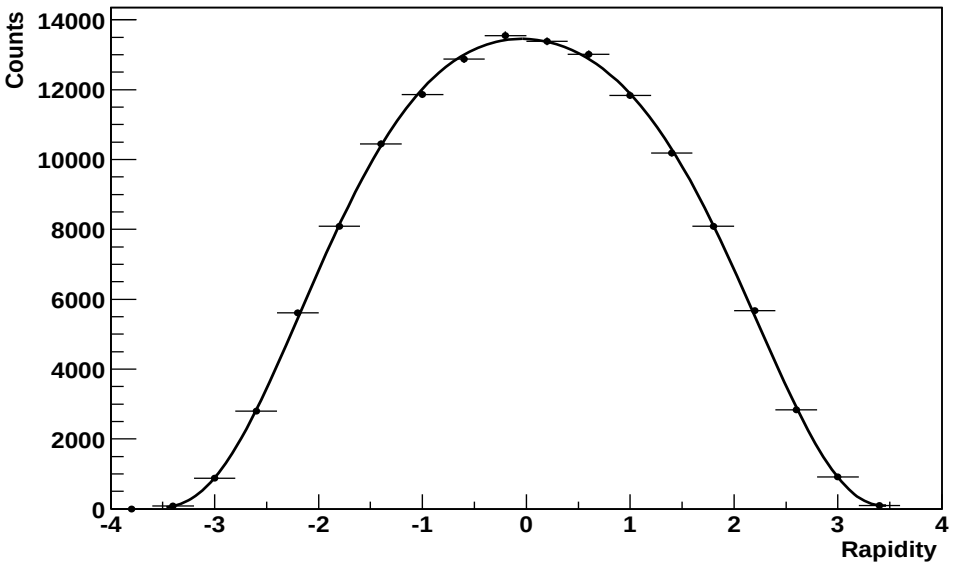

Figure 5.20: 4π rapidity distribution for $J/\psi \to \mu^+\mu^-$ produced by the PYTHIA event generator.

the production cross section times the branching ratio as a function of rapidity obtained using this technique. The electron data is the point at zero rapidity, and the muon data are the two points at negative rapidities. The PYTHIA rapidity distribution has been normalized to the data for comparision. A gaussian curve has been fitted to the data and integrated to produce the total production cross section of $\sigma_{J/\psi} = 3.8 \pm 0.6$ (stat.) $\pm$ 1.3 (syst.) μb. This is the current PHENIX preliminary data point for the J/ψ production cross section. This method is consistent within errors with the calculation performed above using only the muon data and relying on the rapidity distribution of PYTHIA to compute the integrated cross section. There are several functional forms which could potentially

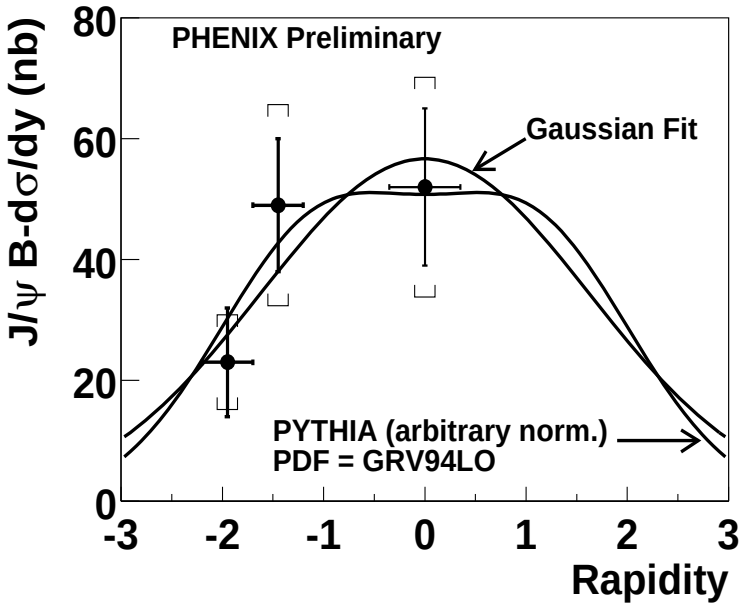

Figure 5.21: Production cross section as a function of rapidity from the combined PHENIX dimuon and dielectron data (taken from [Fra 02]).

be fitted to the data points in Figure 5.21, and considering the large error bars one should not draw any conclusions about the agreement or disagreement of the two methods at this point.

The measurement compares favorably to theoretical predictions. Fig. 5.22 shows the predictions for the hadroproduction J/ψ cross section from the color evaporation model at next to leading order, as discussed in [Amu 97]. The PHENIX preliminary data point is shown, along with the data point from this analysis. Theoretical predictions are shown for two parton distribution functions, GRV HO and MRS A. The model contains one free parameter, the fraction of onium states which materialize as J/ψ 's. This parameter is determined from

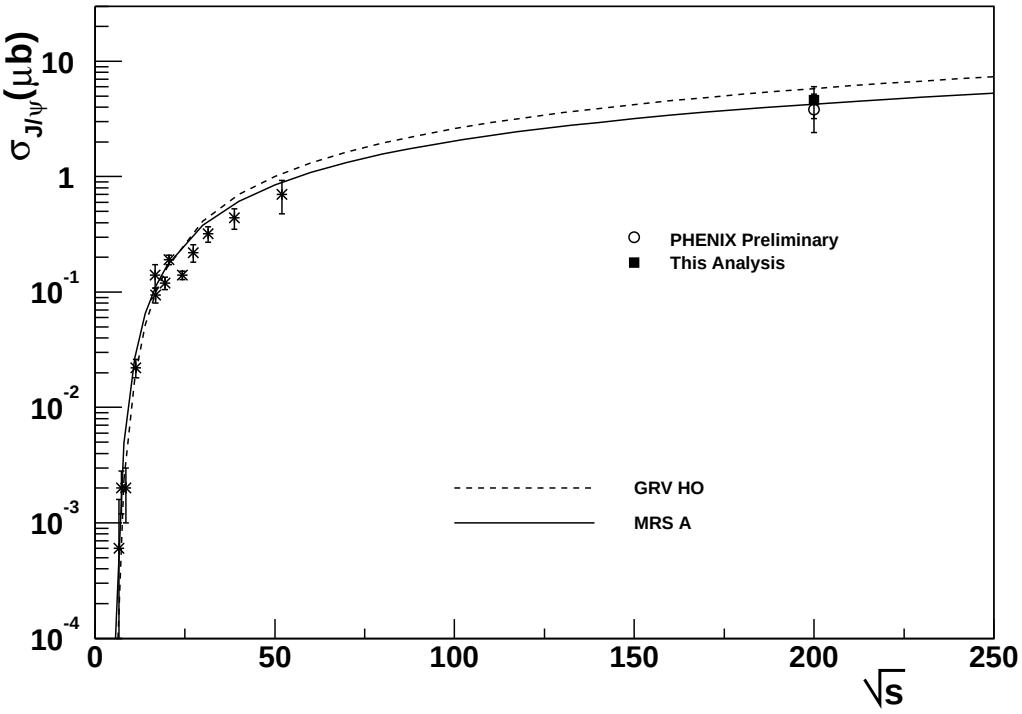

Figure 5.22: Color evaporation model predictions and measurements for hadroproduction of J/ψ . The PHENIX preliminary data point is shown, along with the result from this analysis, and results of previous measurements at lower energies. Theoretical predictions and low energy data points are taken from [Amu 97].

photoproduction data and used in the hadroproduction predictions. In addition, a K factor is used to account for higher order QCD corrections. This K factor is determined by fitting the hadroproduction cross section of $D\bar{D}$ pairs. The K factor used is 1.27 for the GRV HO distribution, and 1.71 for the MRS A distribution.

Data points from previous measurements at lower energies are also shown. It is interesting that the color evaporation model, a much simpler model than the NRQCD theory, appears to predict J/ψ production quite well. However, the

model is generally considered to be overly simplistic, because it ignores the color and spin of the interacting particles.

The NRQCD formalism is currently the leading theory for charmonium production. Unfortunately, there has not been a prediction for the total J/ψ cross section at our energy published in the literature. However, two PHENIX collaborators (H.D. Sato and N. Saito) have attempted to calculate the NRQCD prediction for the total J/ψ cross section at our energy of $\sqrt{s} = 200$ GeV [Sat 02a]. Their calculation uses the color octet matrix elements determined from the Tevatron data. Figure 5.23 shows their result for the NRQCD prediction for the total J/ψ cross section as a function of $\sqrt{s}$ for several different parton distribution functions. The QCD scale $Q = m_c$ is used. The PHENIX preliminary data point is shown and it is consistent with the NRQCD predictions.

5.6 J/ψ Polarization

The polarization is determined experimentally by observing the angular distribution of the dimuon decay products. In the J/ψ rest frame, the J/ψ with $J = 1$ decays to a muon pair which must also have $J = 1$. Take the quantization axis for the J/ψ to be the direction of the J/ψ linear momentum in the lab frame. Let the decay muons be produced with momenta at an angle θ with respect to this quantization axis. This is equivalent to the original J/ψ state $\phi(j, m)$ being transformed by a rotation about the y-axis through an angle θ. The transformed

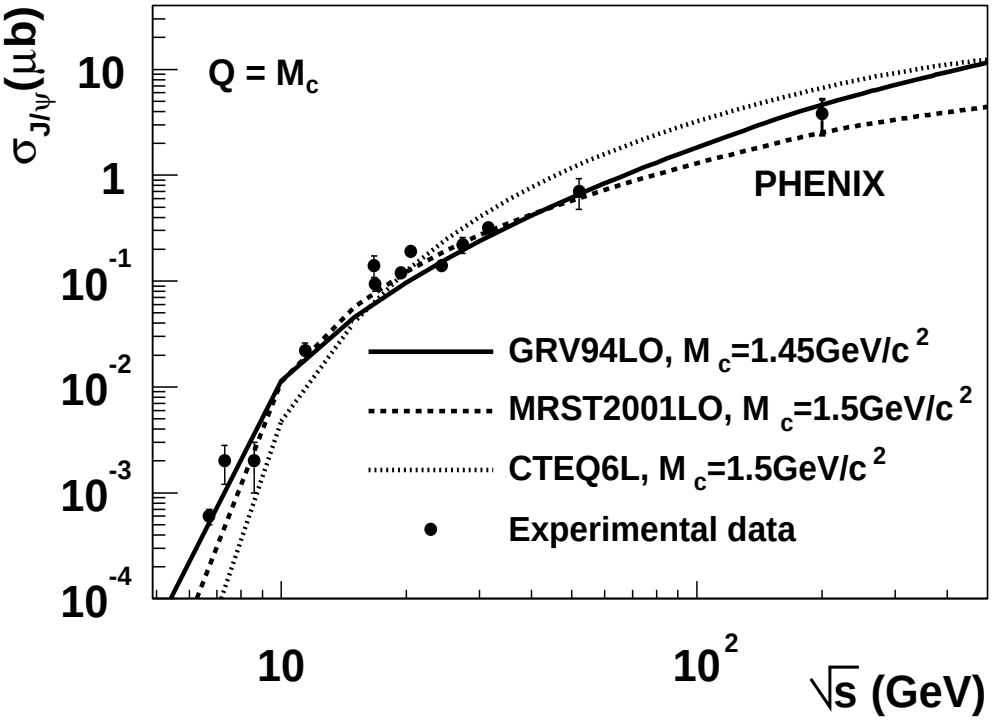

Figure 5.23: NRQCD total J/ψ cross section dependence on $\sqrt{s}$ and the PHENIX measurement (taken from [Sat 02a]).

wavefunction $\phi(j, m')$ can be expressed as a linear superposition of the old wavefunction with values of m = -1, 0, and 1. Using the rotation operator $e^{-iJ_y\theta}$, the transformation is written as

$$e^{-iJ_y\theta}\phi(j,m) = \sum_{m'} d^j_{m',m}(\theta)\phi(j,m') \ . \tag{5.7}$$

The coefficients $d^j_{m',m}$ are called the rotation matrices, and they are calculated from

$$\phi^*(j,m')e^{-iJ_y\theta}\phi(j,m) = d^j_{m',m} \ . \tag{5.8}$$

When the J/ψ has $m = \pm 1$ it is said to be transverse, when $m = 0$ it is called longitudinal. The $d^j_{m',m}$ represent the amplitude for emitting a μ^+ at an angle θ with respect to the J/ψ momentum in the lab frame. If σ_T is the cross section for producing the J/ψ in an $m = \pm 1$ state, and σ_L the cross section for the $m = 0$ state, the angular distribution of the total cross section is

$$\frac{\mathrm{d}\sigma}{\mathrm{dcos}\theta} \propto \sigma_T[(d^1_{1,1})^2 + (d^1_{1,-1})^2] + 2\sigma_L(d^1_{1,0})^2 \ . \tag{5.9}$$

The explicit forms for the rotation matrices can be calculated or looked up in a table. They are

$$d^1_{1,0}(\theta) = -\frac{1}{\sqrt{2}}\mathrm{sin}\theta \ , \tag{5.10}$$

$$d^1_{1,1}(\theta) = \frac{1}{2}(1 + \mathrm{cos}\theta) \ , \tag{5.11}$$

$$d^1_{1,-1}(\theta) = \frac{1}{2}(1 - \mathrm{cos}\theta) \ . \tag{5.12}$$

Using these forms in Equation 5.9 gives

$$\frac{\mathrm{d}\sigma}{\mathrm{dcos}\theta} \propto 1 + \frac{\sigma_T - 2\sigma_L}{\sigma_T + 2\sigma_L}\mathrm{cos}^2\theta \ . \tag{5.13}$$

We can then define the polarization parameter $\lambda \equiv \frac{\sigma_T - 2\sigma_L}{\sigma_T + 2\sigma_L}$, so that

$$\frac{\mathrm{d}\sigma}{\mathrm{dcos}\theta} \propto 1 + \lambda\mathrm{cos}^2\theta \ . \tag{5.14}$$

λ is 0 for unpolarized charmonium, -1 for longitudinal polarization, and +1 for transverse polarization.

A simulation is used to study the angular distribution of the positive decay muon for various values of the polarization. Ideally, one would separate the data

into x_F and p_t bins to study the dependence of the polarization on those parameters. The acceptance of the detector is dependent on the kinematic range and each bin has a unique acceptance correction. Figure 5.24 shows the how the shape of the cosθ acceptance of the south muon arm for unpolarized J/ψ varies for different bins of x_F and p_t . The events in Figure 5.24 were generated with PYTHIA implementing a simple geometrical cut on the theta angle of the decay muons corresponding to the acceptance of the south arm, and requiring the muons to have a total momentum of at least 2 GeV. Only the shapes of the acceptances are shown, the curves are not normalized. The small number of J/ψ in this analysis will not permit such a mapping of the data in x_F and p_t bins. Instead, we will only look at J/ψ in the ranges 0 GeV $< p_t <$ 5 GeV and -1 $< x_F <$ 0, and produce one acceptance correction for that kinematic region. Figure 5.25 shows the simulated cosθ distribution for three values of J/ψ polarization (-1, 0, and +1) for J/ψ in the kinematic range 0 GeV $< p_t <$ 5 GeV and -1 $< x_F <$ 0. These curves were generated using the full detector simulation, which includes the inactive high voltage and readout electronics. The shape of the curve for no polarization is due entirely to the acceptance of the detector. The curves for transverse and longitudinal polarization are generated by weighting the unpolarized curve by $1 \pm \cos^2\theta$. Because the functions are symmetrical about zero, the absolute value of cosθ is plotted. This also allows one to decrease the statistical error of the bin entries for the small number of J/ψ available for analysis here. The desired procedure would

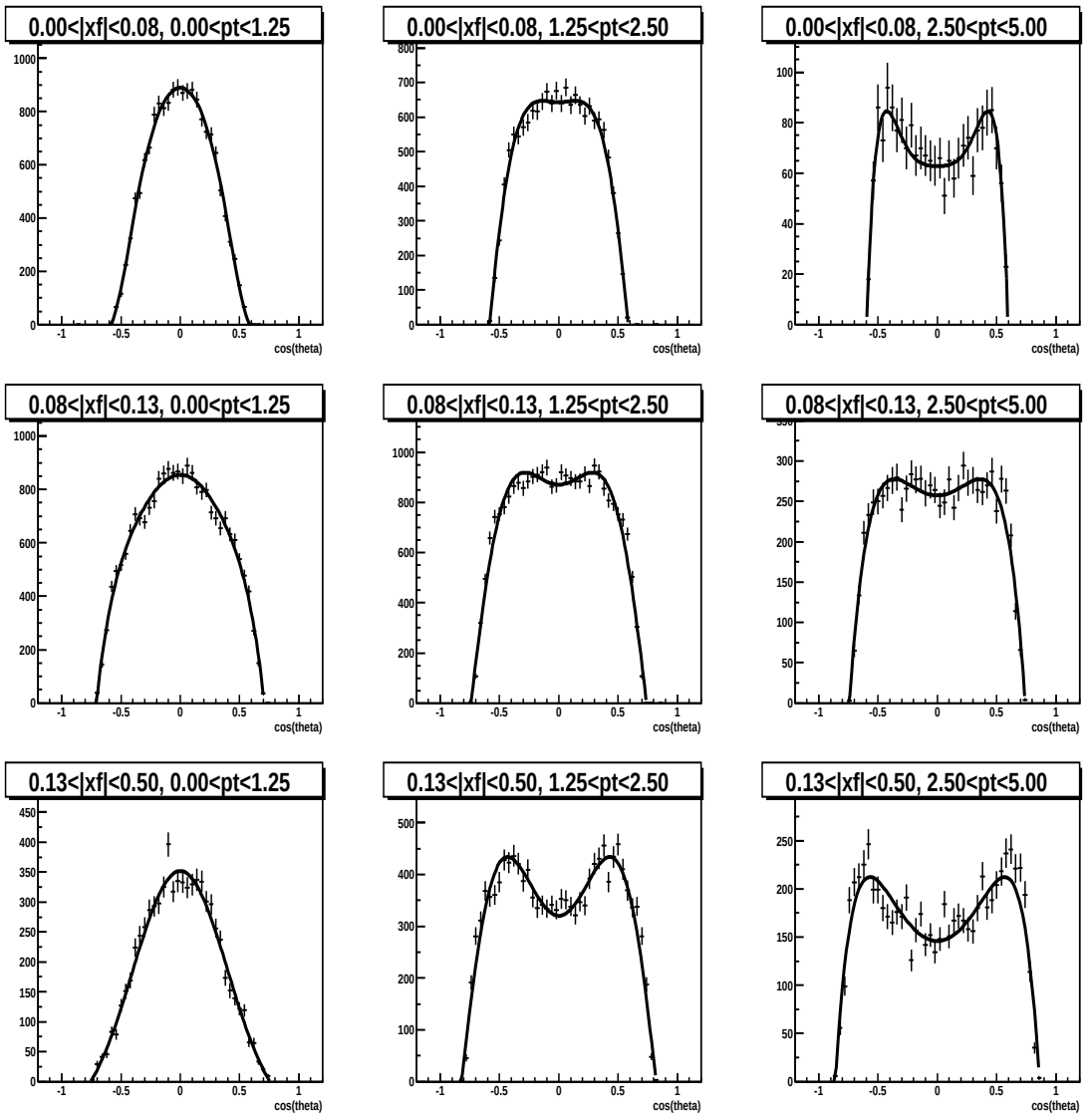

Figure 5.24: Shape of the cosθ acceptance in the south muon arm for simulated unpolarized J/ψ in different $x_{_F}$ and p_t bins.

be to bin the dimuon pairs in bins of cosθ, isolate the J/ψ peak in each of those bins by doing a background subtracton, then extract the number of J/ψ in each bin and plot the cosθ distribution. However, because of the limited number of

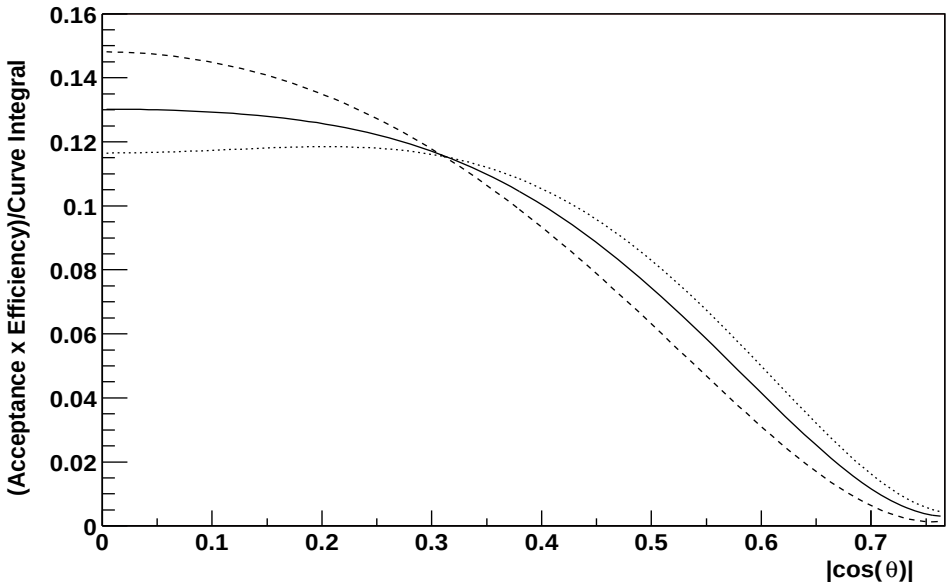

Figure 5.25: Simulated cosθ distributions in the south muon arm for J/ψ in the kinematic range 0 GeV $< p_t <$ 5 GeV and -1 $< x_F <$ 0, with no polarization(solid), transverse polarization(dot), and longitudinal polarization(dash). Each curve is normalized by its integral.

J/ψ available a different technique will be used. The distributions in Figure 5.25 exhibit a point at $|\cos\theta| = 0.31$ where the functions cross. Two regions of $|\cos\theta|$ are defined. One region $0 < |\cos\theta| \leq 0.31$, and a second region $0.31 < |\cos\theta| \leq 0.8$. The number of J/ψ in region 1 can be labeled as I_1, and the number of J/ψ in region 2 can be labeled as I_2. A relation can be derived between the ratio $\frac{I_1}{I_2}$ and the polarization.

The acceptance curve for unpolarized J/ψ in Figure 5.25 is fitted with a function of the form

$$f(x) = a(1 + bx^2 + cx^4 + dx^6) \tag{5.15}$$

where $x \equiv \cos\theta$ and a, b, c, d are free parameters. For polarized J/ψ , the acceptance is found by weighting Equation 5.15 by $1 + \lambda x^2$. Thus, the acceptance function for arbitrary polarization is

$$f_\lambda(x) = a(1 + bx^2 + cx^4 + dx^6)(1 + \lambda x^2) \tag{5.16}$$

The ratio $\frac{I_1}{I_2}$ is then given by

$$\frac{I_1}{I_2} = \frac{\int_0^{0.31} f_\lambda(x)\mathrm{d}x}{\int_{0.31}^{0.8} f_\lambda(x)\mathrm{d}x} \ . \tag{5.17}$$

The returned fit parameters for the unpolarized curve in Figure 5.25 are $a = 0.130$, b = -0.616, c = -6.33, and d = 7.74. Using these parameters and performing the integration, one arrives at the relation between the ratio $\frac{I_1}{I_2}$ and the polarization λ:

$$\lambda = \frac{0.0274(\frac{I_1}{I_2}) - 0.0391}{0.00122 - 0.00600(\frac{I_1}{I_2})} \ . \tag{5.18}$$

The relation is shown in Figure 5.26.

The *pp* dimuon data will be divided into these two regions of $|\cos\theta|$. For each of the two regions, the background will be constructed using the same method as in section 5.4, the J/ψ peak will be isolated, and the number of J/ψ will be determined. The ratio of J/ψ in the two regions will be computed, and the polarization will be determined by Equation 5.18. When this algorithm was applied to the J/ψ simulation data, which is known to have zero polarization, the result was $\lambda = 0.030 \pm 0.21$, consistent with zero. An R factor for each of the

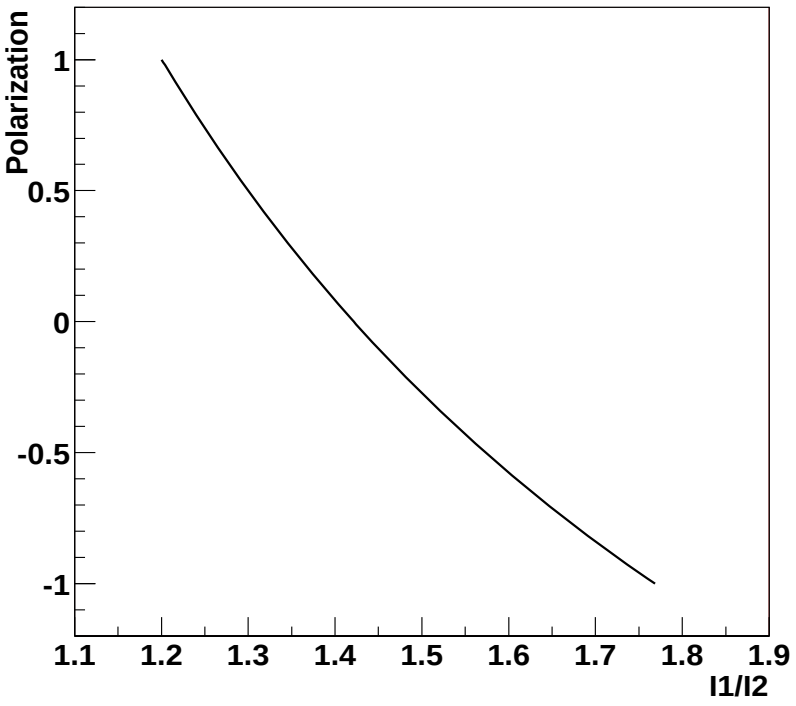

Figure 5.26: Relation between the number of J/ψ in region 1 divided by the number of J/ψ in region 2 for different J/ψ polarizations.

two regions of $|\cos\theta|$ is determined. Using the method described in Section 3 gives $R_{0<|\cos\theta|\leq 0.31} = 1.72$ and $R_{0.31<|\cos\theta|\leq 0.8} = 1.00$. The background is then constructed from the like sign pairs for both regions using Equation 5.4 The dimuon mass spectrum after the background is subtracted is shown in Figure 5.27 for the region $0 < |\cos\theta| \leq 0.31$, and Figure 5.28 for the region $0.31 < |\cos\theta| \leq 0.8$. The number of J/ψ in the two regions is computed by adding the bin entries in the range 2.33 GeV to 4.0 GeV. This method gives $N^{J/\psi}_{0<|\cos\theta|\leq 0.31} = 26 \pm 5.1$, and $N^{J/\psi}_{0.31<|\cos\theta|\leq 0.8} = 18 \pm 4.2$. The ratio of J/ψ in the two regions of $|\cos\theta|$ is then

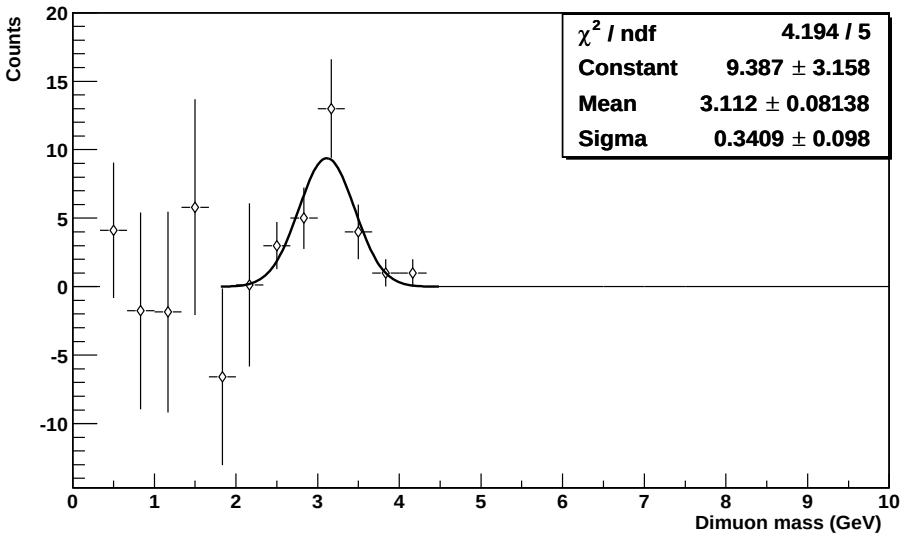

Figure 5.27: Dimuon mass spectrum after background subtraction for the region $0 < |\cos\theta| \leq 0.31$.

$\frac{I_1}{I_2} = 1.4 \pm 0.44$. Using Equation 5.18 one finds the polarization parameter

$$\lambda = 0.11 \pm 1.6 \text{ (stat)} , \tag{5.19}$$

where the error given is the statistical error.

The error of this measurement will not permit any conclusions to be drawn regarding a comparison to the theoretical predictions. However, the centroid of the measurement appears to be consistent with the expectation that J/ψ in this low range of p_t should have a small polarization. It is informative to ask how many J/ψ would be needed to produce a definitive measurement. Using the technique outlined here, approximately 1000 events would produce an absolute statistical error on the polarization parameter of $\sigma_\lambda \approx 0.35$, 5000 events would give $\sigma_\lambda \approx 0.16$, 10,000 events would give $\sigma_\lambda \approx 0.11$, and 100,000 events would give $\sigma_\lambda \approx$

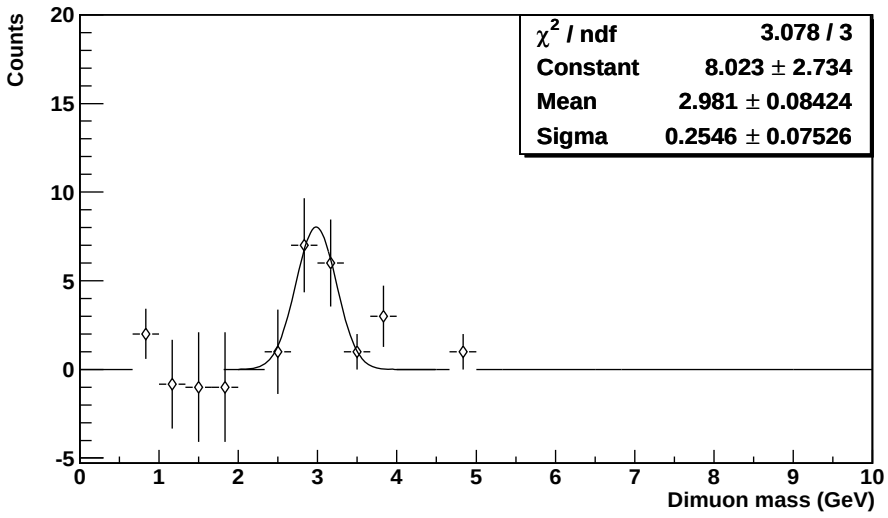

Figure 5.28: Dimuon mass spectrum after background subtraction for the region $0.31 < |\cos\theta| \leq 0.8$.

0.03. These are the number of events required for one bin of x_F and p_T.

6 CONCLUSIONS AND OUTLOOK

The muon spectrometer arms contribute greatly to the overall physics capabilities of the PHENIX detector. The coverage in rapidity is -2.2 $< y <$ -1.2 for the south arm and 1.2 $< y <$ 2.4 for the north arm. The muon physics program is broad and includes both QGP physics and spin physics. In the area of QGP physics, important probes involving muons are J/ψ suppression/enhancement, the melting order of heavy quarkonium states, and strangeness enhancement. In the area of spin physics, the gluon spin is probed with open heavy flavor production, and the antiquark helicity distributions are probed with W boson production and the Drell-Yan process. In addition, important tests of current models for charmonium production can be performed with measurements of the charmonium production cross section and charmonium polarization.

The muon spectrometer arms were designed to collect data in both proton and heavy ion collisions. The detector must perform muon tracking and identification for a wide range of chamber occupancies and track momentum. For the second RHIC running period in 2001-02, the south muon arm was completed and collected its first data. The performance of the detector was close to the design goals. There was some acceptance loss due to areas of inactive electronics and chamber high voltage. For future data-taking runs, these issues will be addressed and the performance of the detector will continue to improve significantly.

The analysis of the first data collected with the south muon arm exhibits a clear J/ψ mass peak. The production cross section for J/ψ in proton collisions at $\sqrt{s} = 200$ GeV has been measured. The observed value of $\sigma^{pp}_{J/\psi} = 4.6 \pm 0.7 \pm 1.2$ μb agrees well with the color evaporation model and is consistent with color octet model predictions. A technique for performing a J/ψ polarization measurement was studied, and a very low statistics measurement was attempted. However, the available statistics will not permit any definite conclusions to be drawn at this point.

The outlook for future RHIC running periods is good. Higher beam luminosities, a more efficient detector, and the addition of the north muon arm will produce high statistics data sets, bringing the full potential of the muon arms into reach. An important study of J/ψ production in d-Au and Au-Au collisions will be performed in the coming years. Proton collisions at $\sqrt{s} = 500$ GeV will extend the kinematic range to higher p_t values for W boson production and open heavy flavor studies, as well as allowing a polarization measurement for high p_t charmonium states.

REFERENCES

[Abr 97] M.C. Abreu *et al.*, Phys. Lett. **B410**, 337 (1997)

[Abr 00] M.C. Abreu *et al.*, Phys. Lett. **B477**, 28 (2000)

[Abr 00a] M.C. Abreu *et al.*, Eur. Phys. J. **C14** 443 (2000)

[Aff 00] T. Affolder *et al.*, Phys. Rev. Lett. **85**, 2886 (2000)

[Aki 03] H. Akikawa *et al.*, accepted for publication in Nucl. Instrum. Meth. **A**, Special Issue (2003).

[Amu 97] J.F, Amundson O.J.P. Eboli, E.M. Gregores, and F. Halzen, Phys. Lett. **B390**, 323 (1997)

[Ash 88] J. Ashman *et al.*, Phys. Lett. **B206**, 364 (1988)

[Bai 83] R. Baier and R. Ruckl, Z. Phys. **C19**, 251 (1983)

[Ben 96] M. Beneke and I.Z. Rothstein, Phys.Rev. **D54**, 2005 (1996)

[Bod 97] G.T. Bodwin, E. Braaten, and G.P. Lepage, Phys. Rev. **D51**, 1125 (1997)

[Bra 95] E. Braaten and S. Fleming, Phys. Rev. Lett. **74**, 3327 (1995)

[Bra 00] E. Braaten, B. Kniehl, and J. Lee, Phys. Rev. **D62**, 94005 (2000)

[Bro 98] M. Brooks and J. Moss, "Heavy Flavor Production via Single Muon Detection in the PHENIX Detector at $\sqrt{s}$=200 GeV," PHENIX Technical Note 361 (1998)

[Cho 95] P. Cho and M. Wise, Phys. Lett. **B346**, 129 (1995)

[Cho 02] I.J. Choi *et al.*, "A Quick Alignment and its Resolution Studies for the Muon Arm Spectrometer," PHENIX Technical Note 398, (2002)

[Cia 02] V. Cianciolo *et al.*, "MuID Square-Hole Shielding Study", PHENIX Technical Note 394, (2002)

[Dre 99] B. Dressler *et al.*, Eur. Phys. J. **C18**, 719 (1999)

[Dri 81] D. Drijard *et al.*, Z. Phys. **C9**, 293 (1981)

[Fra 77] S.C. Frautschi, S. Pakvasa, and S.F. Tuan, Nucl. Phys. **B121**, 141 (1977)

[Fra 02] A.D. Frawley, for the PHENIX collaboration, To appear in the proceedings of Quark Matter 2002 (QM 2002), Nantes, France, 18-24 Jul 2002

[Gao 90] M. Gao, Phys. Rev. **D41**, 626 (1990)

[Gas 87] R. Gastmans, W. Troost, and T.T. Wu, Nucl. Phys. **B291**, 731 (1987)

[Hag 02] K. Hagiwara *et al.*, Phys. Rev. **D66**, 010001 (2002)

[Inn 91] V. Innocente, M. Maire, and E. Nagy, In Amsterdam 1991, Proceedings, MC91:Detector and event simulation in high energy physics (see HIGH ENERGY PHYSICS INDEX 30 (1992) No. 3237), 58 (1991)

[Inn 93] V. Innocente, Nucl. Instrum. Meth. **A324**, 297 (1993)

[Jaf 96] R. Jaffe, Phys. Lett. **B365**, 359 (1996)

[Kam 98] B. Kamal, Phys. Rev. **D57**, 6663 (1998)

[Kar 94] M. Karliner and R.W. Robinett, Phys. Lett. **B324**, 209 (1994)

[Krä 01] M. Krämer, Prog. Part. Nucl. Phys., **47**, 141 (2001)

[Mat 88] E. Mathieson, Nucl. Instrum. Meth. **A270**, 602 (1988)

[Mat 86] T. Matsui and H. Satz, Phys. Lett. **B178**, 416 (1986)

[McL 85] L.D. McLerran, Acta. Phys. Polon., **B16**, 669 (1985)

[Mül 95] B. Müller, Rept. Prog. Phys. **58**, 611 (1995)

[Nag 02] J. Nagle, for the PHENIX collaboration, "$J/\psi \rightarrow$ ee Preliminary Results from Run 2 (pp and AuAu)," PHENIX Analysis Note 117 (2002)

[Nas 01] P. Nason *et al.*, Published in CERN-YR-2000/01, hep-ph/0003142 (2001)

[PHE 94] The PHENIX Spin Collaboration, "Spin Structure Function Physics with an Upgraded PHENIX Muon Spectrometer," http://www.phenix.bnl.gov/phenix/WWW/muon/spin/spin2.ps, (1994)

[PHE 98] The PHENIX Muon Arms Team, "The PHENIX Muon Arms: Current Design and Status" (1998)

[Qui 98] J. Qui, J.P. Vary, and X. Zhang, Phys. Rev. Lett., **88**, 232301 (1998)

[Raf 82] J. Rafelski and B. Müller, Phys. Rev. Lett. **48**, 1066 (1982)

[Sai 95] N. Saito and J.M. Moss, "Spin Physics with Inclusive Muon Production," http://www.phenix.bnl.gov/phenix/WWW/muon/notes/d10.ps, (1995)

[Sat 02] H. Sato and V. Cianciolo, "Preliminary Measurement of the J/ψ Production Cross Section by the South Muon Arm in Run-2," PHENIX Analysis Note 118 (2002)

[Sat 02a] H. Sato and N. Saito, "Comparison of the Preliminary Results of J/ψ Measurements in Run-2 p+p Collisions with the Perturbative QCD Based Models," PHENIX Analysis Note 162 (2002)

[Sho 85] A. Shor, Phys. Rev. Lett. **54**, 1122 (1985)

[Sof 98] J. Soffer and J.M. Virey, Nucl. Phys. **B509**, 297 (1998)

[The 01] R. Thews, M. Schroedter, and J. Rafelski, Phys. Rev. **C63**, 054905 (2001)

[Tow 01] R.S. Towell *et al.*, Phys.Rev. **D64**, 052002 (2001)

[Van 95] M. Vanttinen *et al.*, Phys. Rev. **D51**, 3332 (1995)

[Zha 00] B. Zhang *et al.*, Phys. Rev. **C62**, 054905 (2000)